Prepared Under Contract AT(39-1)-1477

With

U. S. Atomic Energy Commission

RESEARCH MEMORANDUM

THE BLAST WAVE IN AIR RESULTING FROM A HIGH TEMPERATURE, HIGH PRESSURE SPHERE OF AIR (U)

H. L. Brode

RM-1[illegible]-AEC

December 3, 1[illegible]

(Released 10-30-[illegible])

Assigned to _____

This is a working paper. It may be expanded, modified, or withdrawn at any time.

The RAND Corporation

1700 MAIN ST. • SANTA MONICA • CALIFORNIA

SUMMARY

This report contains the results of a calculation of the blast wave resulting from the explosion of a sphere of air initially at rest and at standard sea-level density but at 20,000 atmospheres pressure. Results are presented in graphical form, showing the variations of overpressure, density, particle velocity, temperature and dynamic pressure as functions of space and time. Shock values of these parameters, total impulses, positive durations and shock arrival times are also illustrated. Comparison is made with other calculations and with observations.

CONTENTS

I. INTRODUCTION

A calculation of the blast wave in air resulting from a hot (386,300 ^{o}K), high pressure (20,000 atmos) sphere of air initially at rest is reported here. This particular calculation was made on the RAND high speed computer (Johnniac) in 1955-1956. Some similar calculations, carried out at the same time, have been reported previously [1,2,3] but the press of more recent calculations has delayed the publication of the results presented here.

THE METHOD

The work was accomplished by a step-wise solution of a system of difference equations, approximating that set of differential equations which in turn represent the usual hydrodynamic (or conservation) equations in spherical symmetry.[1]

Solving any such system of difference equations with the accuracy and detail represented here involves a great many special considerations and much machine and programming time. Since Ref. (1) includes a discussion of most of these factors, they will not be mentioned further here. The fit to the equation of state of air, as used here, however, is the slightly improved form reported in Ref. (3).

THE PROBLEM

The initial conditions for this problem specified an isothermal sphere of air at normal (standard sea-level) density and 20,000 atmos pressure--initially at rest. This required an air temperature of about 386,300 ^{o}K. At time zero this sphere was released in a standard sea-level atmosphere.

THE UNITS

The computations used the following set of units for the hydrodynamic parameters:

Radius: $\lambda = R/\alpha$

Time: $\tau = tc_o/\alpha$

where the length α is defined as $\alpha^3 = W/P_o$, with W = total blast energy.

Pressure: $\pi = P/P_o$

Density: $\eta = \rho/\rho_o$

Particle velocity: $\beta = u/c_o$

Temperature: $\theta = T/T_o$

where P_o, ρ_o, c_o, T_o are the pressure, density, sound speed and temperature in the ambient or pre-shocked air.

II. THE RESULTS

PRESSURE VS RADIUS

In Fig. 1 the spacial distribution of pressures is illustrated for the earliest times in the explosion. There are several things to note about this beginning: The shock wave in air starts with an initial strength well below the initial pressure of the sphere, and very shortly decays even further in the spherical divergence. Between the outward moving shock and the inward moving rarefaction, at the contact surface, a second shock develops, and begins to grow inward from that surface while the latter moves out in the general expansion. When the rarefaction wave has exhausted itself, this inward-facing second shock begins to implode on the origin.

In Fig. 2, one can trace the progress of this imploding shock and note its reflection. Figure 2 also illustrates the shock pressure spike at the main shock front which is typical of all strong spherical shock waves. The further progress of the second shock is evident in Fig. 3, where because of a reflection at the contact surface, the second shock is split into a reflected and a transmitted shock, the reflected shock again imploding and the transmitted shock going on up the back of the main shock.

In Fig. 4 the transmitted shock (labeled S_2) can be seen to overtake the main shock, while the reflected shock (labeled S_3) implodes on the origin, reflects and moves out after the main shock.

In Fig. 5 the repetition of this reflection--transmission phenomena occurs and new shocks are generated. Each shock thus generated at these early times is able to overtake and join the main shock, since the regions inside the main shock are still hot and have high sound speeds. As

expansion continues and the shock grows as in Figs. 6 through 11 the nature of the pressure wave becomes much like that of a point source explosion. The effect of the secondary shocks becomes less and less important, eventually becoming insignificant.

In Fig. 8 one can see the first development of a negative phase (where the pressure drops below the pre-shock ambient pressure). The last two curves of Fig. 8 show some negative phase. In Figs. 10 and 11 the finite duration of the negative phase becomes evident and the nature of the pressure pulse shows signs of approaching a semi-acoustical form, represented by a wave of positive pressure followed by a comparable negative wave behind which the air has returned to its initial pressure.

PARTICLE VELOCITY VS RADIUS

The particle velocity profiles of Figs. 12 through 21 illustrate most of the same features mentioned in connection with the pressure profiles. The development of the second shock and its implosion on the origin, its reflection at the center and then at the contact surface and subsequent shock reflections and transmissions are all in evidence. In the later plots a rather wild excursion of velocity near the origin should be understood to have little influence on the bulk of the explosion since here the sound velocities are high and the mass involved is small. Again at the late times the wave forms are very similar to those of the point source explosion.[1]

DENSITY VS RADIUS

Figure 22 illustrates the density changes as a consequence of the explosion in its early phases. The first curve shows the effect of the rarefaction in the inner regions which reduce the density below normal,

the effect of the inward shock which terminates this rarefaction, and the high compression region of the main outward shock. As the expansion continues, the inner air becomes less and less dense, and is traversed by various shocks, while the main shock continues to drive the air out into a density shell. A characteristic difference remains between these density profiles and those of the point source explosion, in that the low density of the interior retains evidence of the beginnings in the isothermal sphere (see Fig. 23). At still later times even this effect becomes insignificant, and density profiles are indeed very similar to a point source density distribution.

TEMPERATURE VS RADIUS

One can again note much of the same shock development in the temperature vs radius plots of Figs. 29 through 34. Of considerable interest is the nature of the temperature profiles at intermediate times (Figs. 31 and 32) which indicate that the initial high temperature air expands quite rapidly behind the shock to many times its initial radius, remaining quite hot even after the expansion stops. This hot sphere of air which is left after the blast wave has moved away, contains considerable energy though it is at a correspondingly low density. Figures 33 and 34, illustrating temperatures at the late times have not been smoothed for publication, and show the original data points connected by straight line segments.

SHOCK PARAMETERS

The arrival time of the main shock as a function of the shock radius is displayed in Fig. 35.

Figure 36 illustrates the decay of shock pressure vs shock radius for the main shock. Note the initial drop as the air shock begins at a pressure well below the pressure of the initial sphere. Note also the jumps in the peak overpressure where the secondary shocks join the main shock. Once the rarefaction wave has exhausted the high pressure sphere, the main shock decay rate becomes that of a point-source strong shock* (inverse cube) and from then on follows more closely the "point-source" picture.

The peak dynamic pressure vs shock radius is illustrated in Fig. 37, while Fig. 38 shows the relation between peak velocity and shock radius, and Fig. 39 illustrates the shock density. The shock temperature is shown in Fig. 40.

IMPULSE AND DURATIONS

The impulses for overpressure and dynamic pressure in the positive phases are specified as functions of the shock radius in Fig. 41. The overpressure impulse (I_p^+) shows a roughly inverse first power dependence on the radius. The dynamic pressure impulse shows a marked change as the shock grows weaker; from a decay even more gradual than the inverse first power to about an inverse cube of the radius. Figure 42 shows the durations of the positive overpressure (D_p^+) and velocity (D_u^+).

BLAST WAVE PARAMETERS VS TIME

The remaining figures (Figs. 43-54) display portions of the time history of the various blast parameters after shock arrival ($t' = t - t_s$)

*Early solutions of a similarity nature with the simplifying assumptions of a point-source and a strong-shock were developed by G. I. Taylor[4] and by J. Von Neumann[5] and lead to a shock pressure which decreased like the inverse cube of the shock radius. Although these solutions are exceedingly useful and ingenious in their simplifications, they fail to give realistic results for other than simple sources, for a complex gas such as air and for shocks of only modest strength.

for a series of distances from the burst point. The peak overpressure at these points ranges from 8090 psi to 3.41 psi, providing a description of the initial behavior of overpressure, dynamic pressure, particle velocity, temperature and density at a wide variety of peak overpressure levels. Reasonable interpolations between graphs allows predictions of other pressure levels.

It should be noted that the overpressure in the early stages of the explosion (Figs. 43-48) exhibits a decay which is best fit by the sum of two negative exponentials:

$$\Delta P(t') = \Delta P_s(ae^{-\alpha t'} + be^{-\beta t'})(1-t'/D_P^+).$$

The last factor may be included to force the overpressure to go to zero at the end of the positive phase. The reality of this essential dichotomy of overpressure decay is made plausible when one considers the nature of the overpressure vs radius profiles while the shock is still strong (Figs. 1-6) from which one sees that the pressure must drop rapidly after the shock has passed, since the shock is moving rapidly and the pressure behind the shock front decreases rapidly with decreasing radius. Once the sharp pulse near the shock front has gone by, the pressure must decay at a slower rate which will be characteristic of the adiabatic expansion of the interior air -- a volume of air which is essentially free of any further pressure gradients.

Similar exponential fits may be readily made for the other parameters, but it is only the overpressure that displays the sharp duality of decay rates.

III. CONCLUSIONS

COMPARISONS OF PEAK OVERPRESSURE

The peak overpressure vs shock radius is shown for comparison (in Fig. 55) for various calculations and for the empirical curve for nuclear explosion (the latter from "The Effects of Nuclear Weapons"[6]). As seen, the agreement between the present calculation (solid line) and the nuclear explosion curve (circled dots) is quite good. This agreement, however, is less good at the lowest pressure, where the difference, corresponding to about 6 per cent in radius, would amount to nearly a 20 per cent difference in explosion energy. At these late stages in the calculation the initial explosion energy has become a small fraction of the ambient energy of the air involved. The explosion energy, then, at late stages is the small difference between the large energies of the engulfed air before and after shock arrival.

The fact that the present curve agrees as well as it does, while other calculations with less correct equations of state for air are different by a nearly constant factor, is indicative of the importance of the equation of state for air explosions. The ideal-gas, point-source results,[7] for instance, can be brought in line over most of the range of overpressures by reducing the energy source by a factor of about one-half, i.e., a real-air point-source explosion is about 50 per cent as efficient as a point-source explosion in an ideal gas of $\gamma = 1.4$.

Also shown in Fig. 55 is the result for the real-air point-source calculation,[1] but since that calculation had an equation of state which was based on the old and incorrect value of the binding energy of the

nitrogen molecule, it might be expected to differ slightly from the present (hot sphere) results. The fact that it differs by as much as it does is somewhat surprising.

The TNT calculation,[3] whose peak overpressure curve is also included on Fig. 55, also had the slightly incorrect fit for the equation of state of air. Perhaps more significantly, the TNT curve illustrates the futility of comparing solid explosive blasts with other types of explosive sources, either blasts from different chemical explosives or from nuclear, spark or impact sources, since at no interesting pressure level can the TNT results be said to have "forgotten" their source. A rough rule as to when an explosion's peak overpressure decay becomes similar to that of a point source, is when the shock wave has engulfed a mass of air ten times the mass of the initial explosive. For chemical explosives such a distance means quite small overpressures.

In connection with the comparison here with a nuclear explosion, it should be further stated that although fair agreement for shock overpressure vs shock radius is achieved, between calculation and empirical curve there is no reason to expect agreement for hydrodynamic quantities much behind the shock front, since in reality other mechanisms must become important there--e.g. radiation transport mechanisms which have been ignored in this simple, spherically symmetric hydrodynamic model, started from a sphere of hot air.

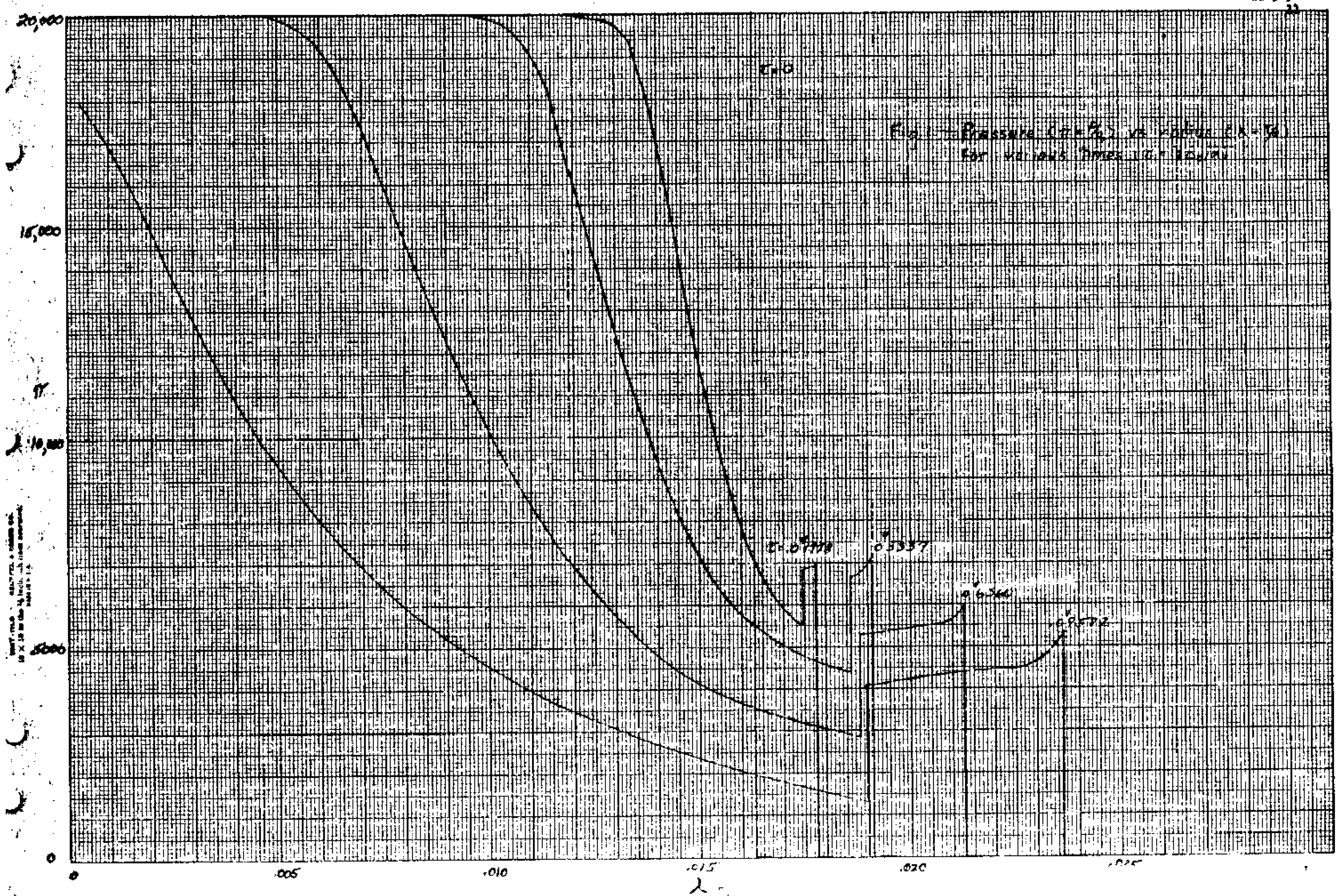
Fig. 1 - Pressure (π = P/P₀) vs Radius (λ = r/a)
for various times (τ = t/a²)
τ=0
τ=.01778
.03337
.06560
.09572
20,000
15,000
π
10,000
5000
0
0
.005
.010
.015
.020
.025
λ

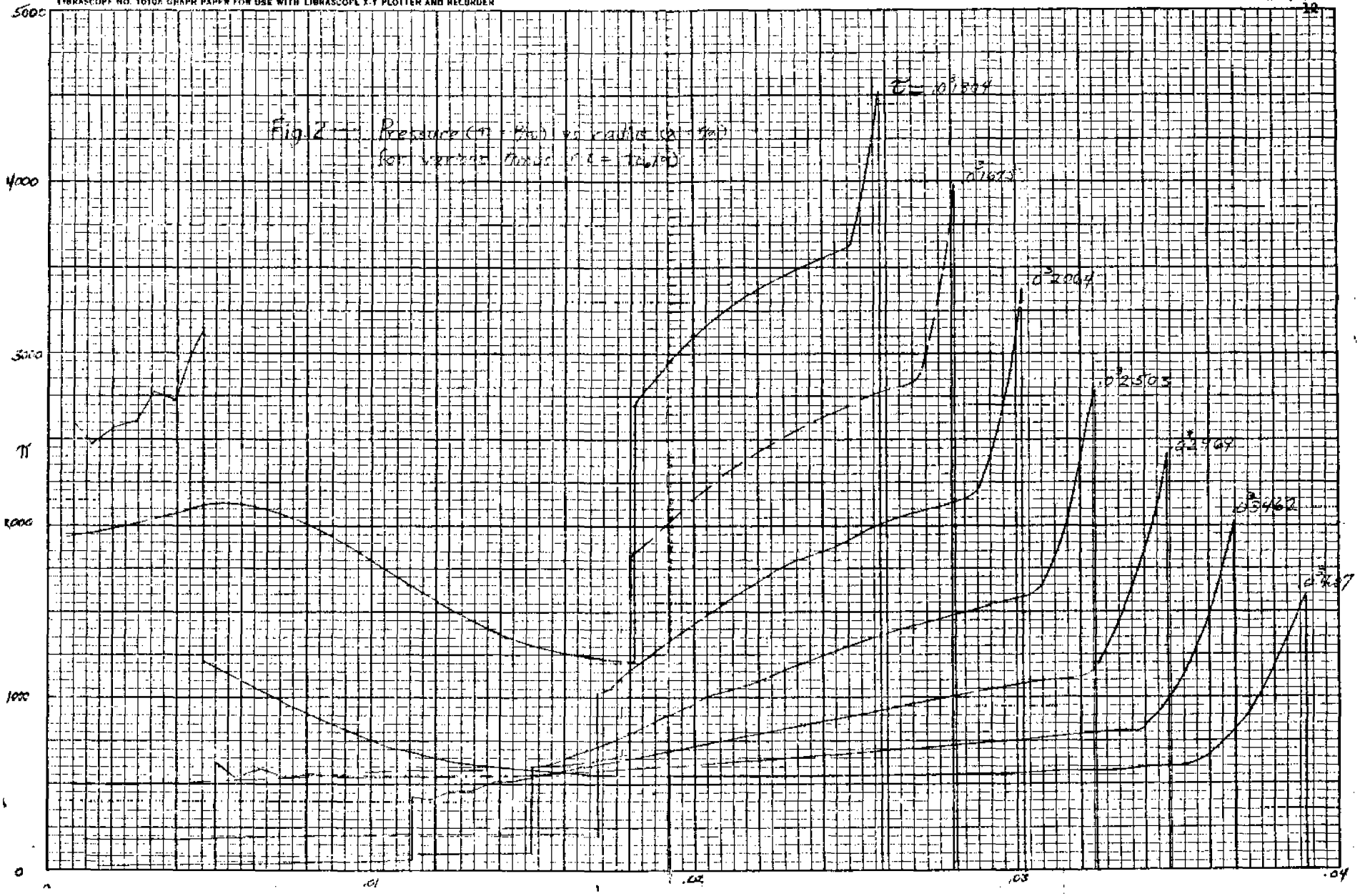

Fig. 2 — Pressure (π - psi) vs radius ($\bar{c}$ - in.) for variable $\bar{c}$ ($\bar{c}$ = 12,10)

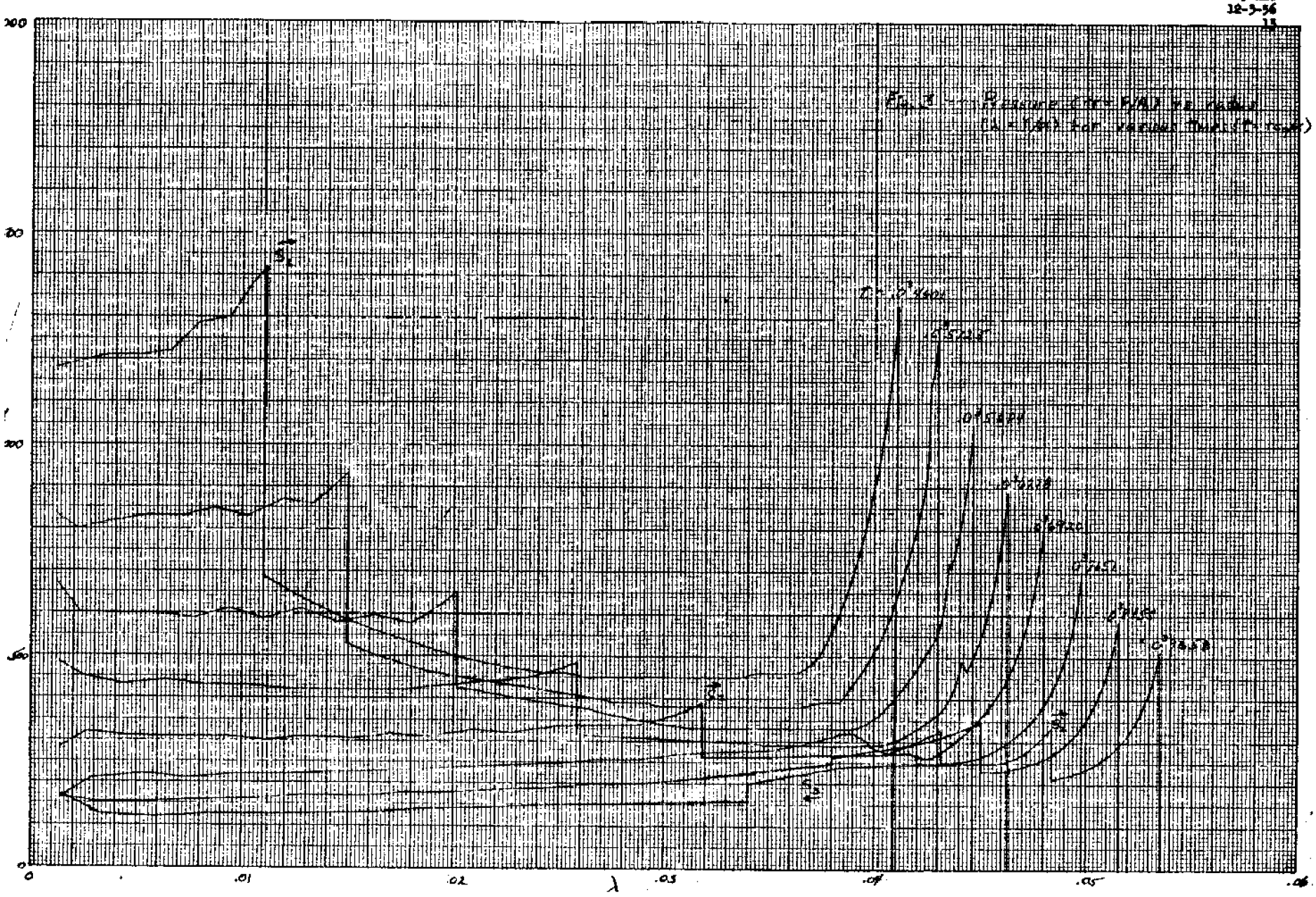
200
100
300
500
0
0
.01
.02
λ
.03
.04
.05
.06

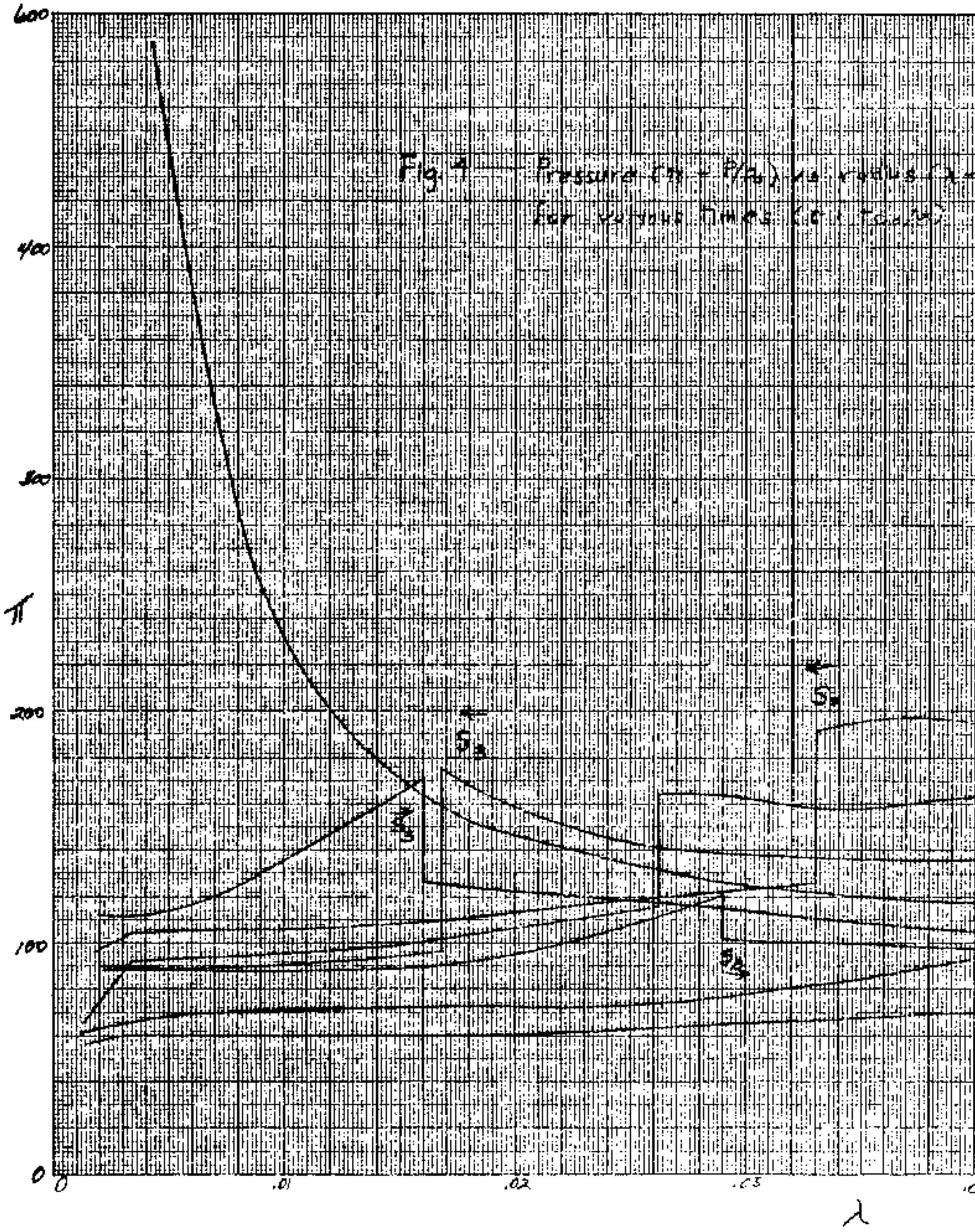
Fig 4 — Pressure (π + P/λ) vs radius
for various times
600
400
300
200
100
0
π
0
.01
.02
.03
λ

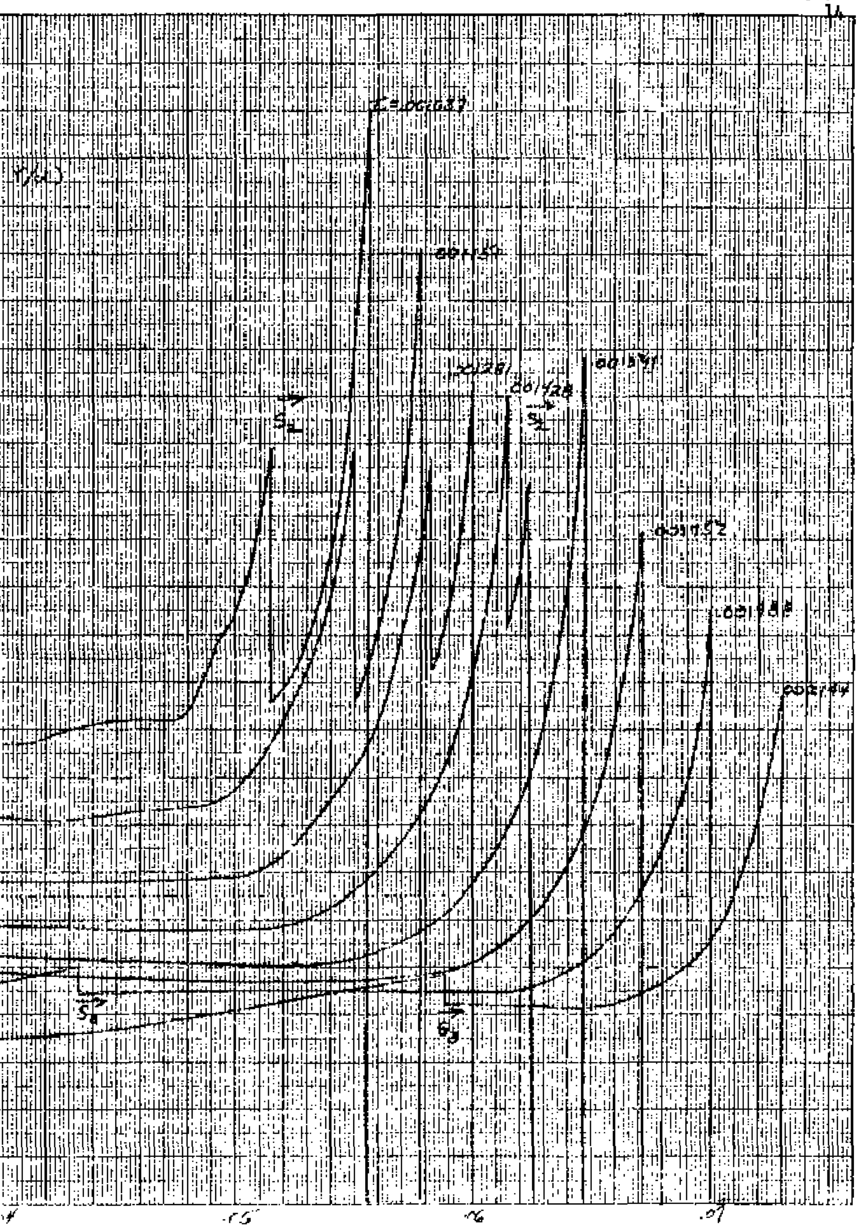
.05
.06
.07

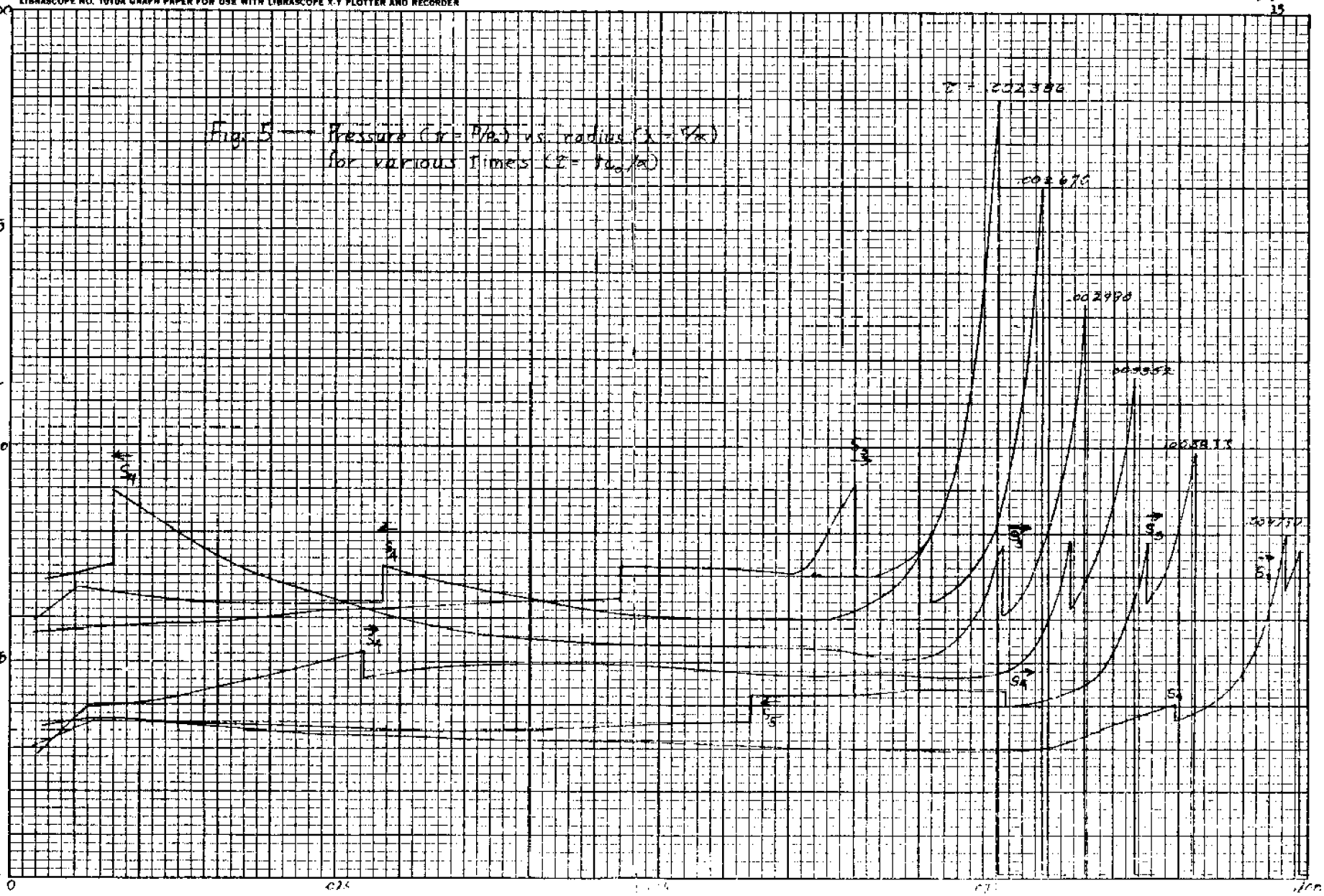

Fig. 5 — Pressure ($\bar{P} = P/p_0$) vs. radius ($\bar{r} = r/a$) for various Times ($\tau = t c_0 / a$)

LIBRASCOPE NO. 2500A CENTIMETERS

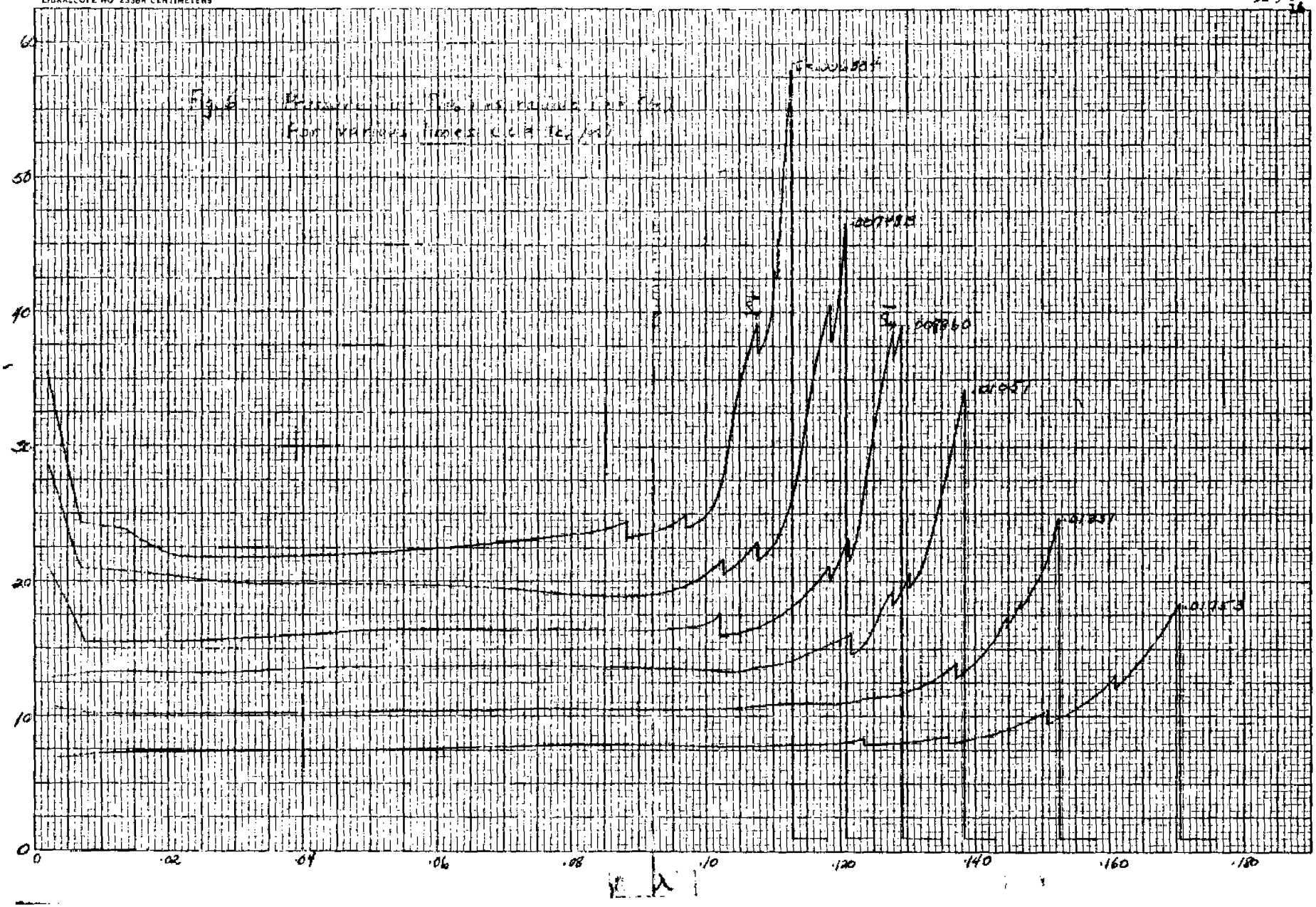

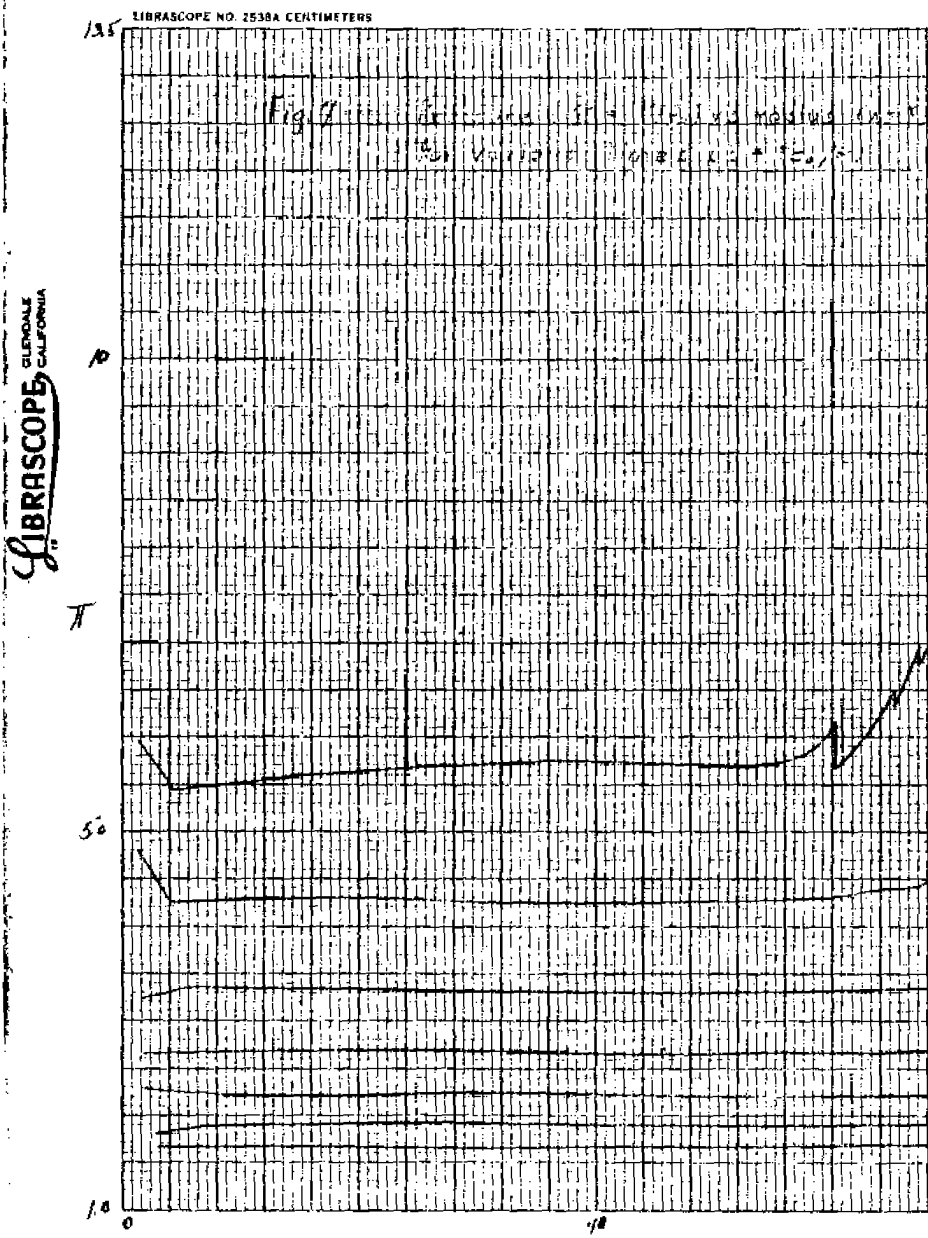
LIBRASCOPE NO. 2538A CENTIMETERS
LIBRASCOPE GLENDALE CALIFORNIA
Fig 7
0

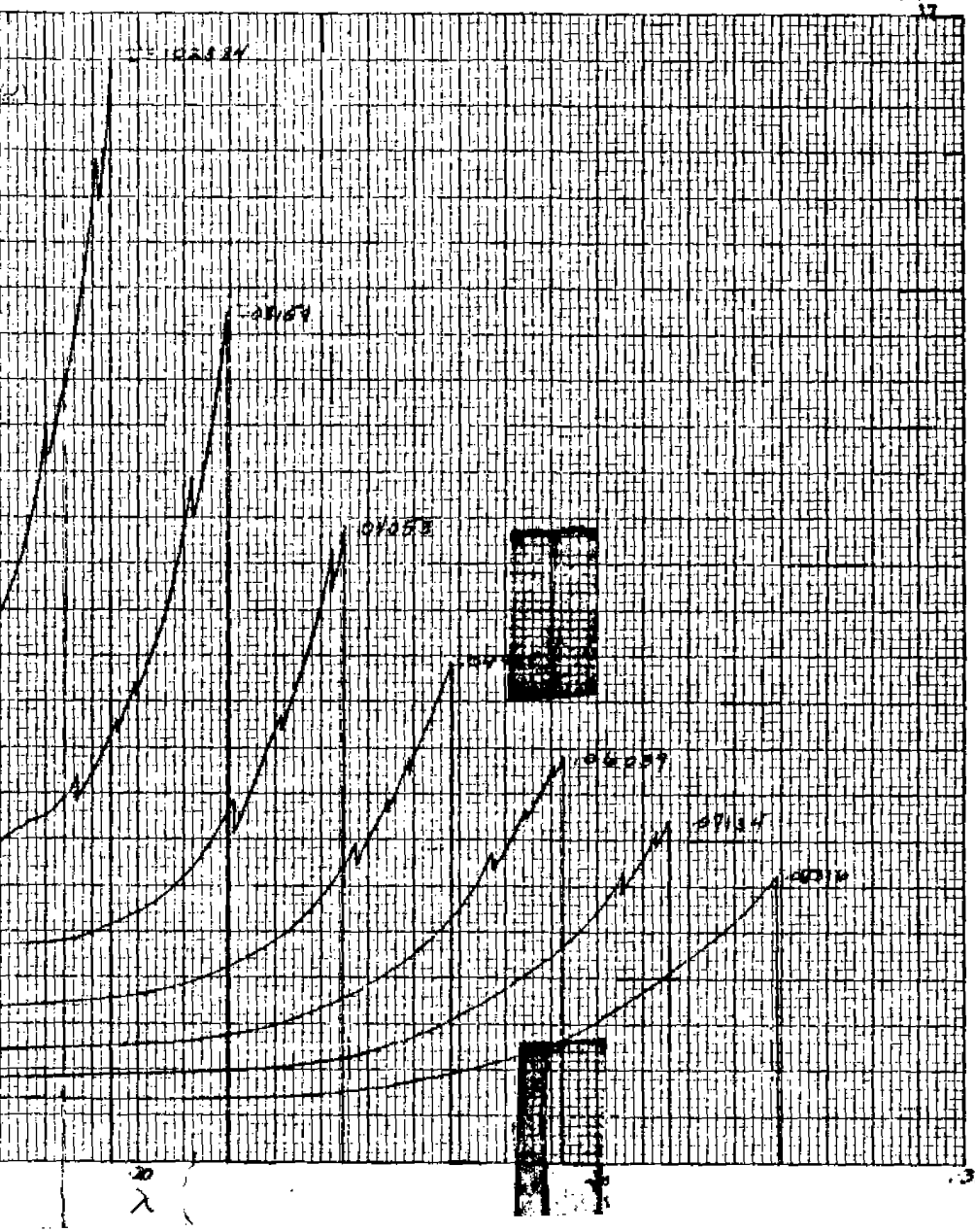
20
λ
30

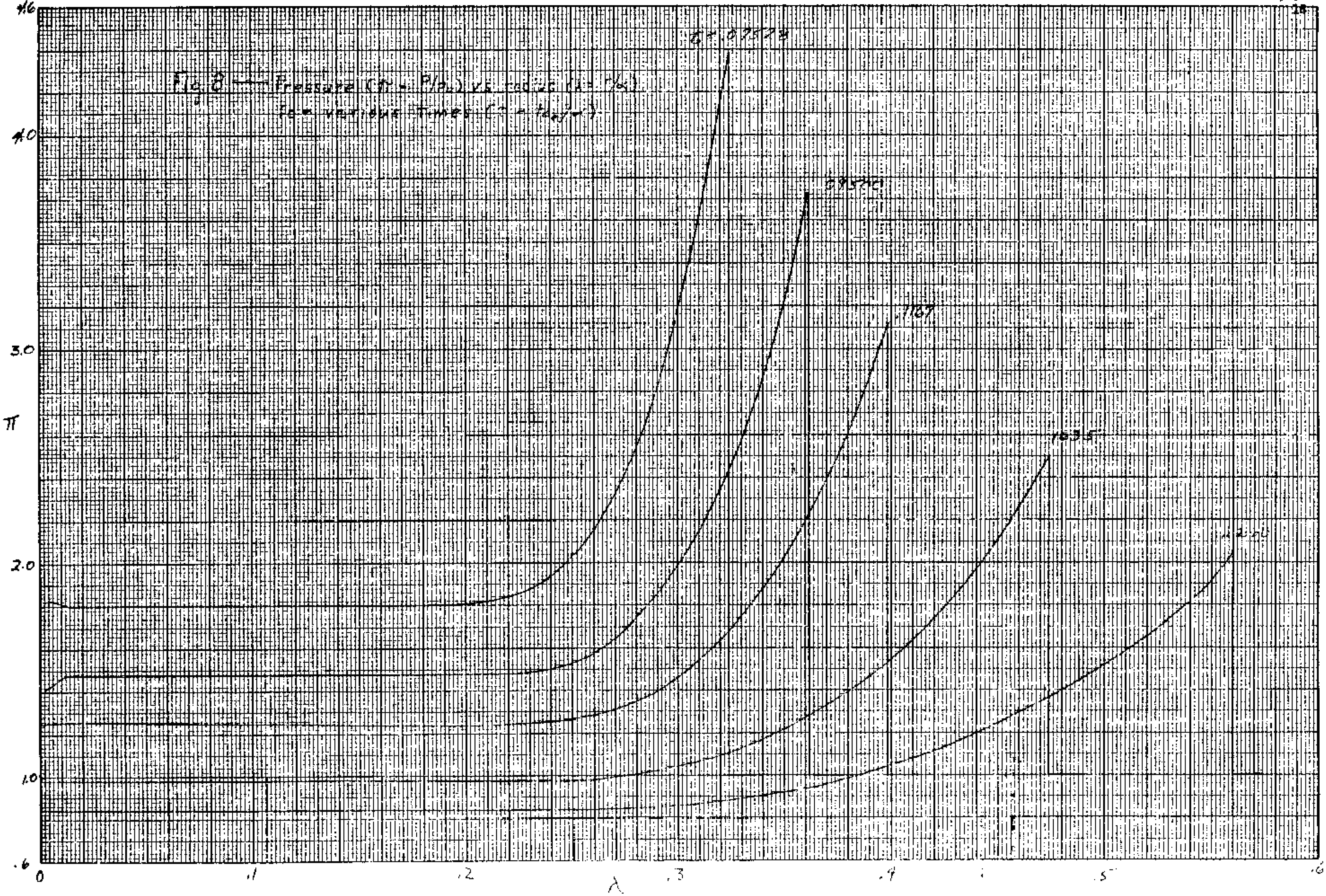

Fig. 8 — Pressure (π = P/p₀) vs radius (λ = r/a)
for various times (τ = t/...)

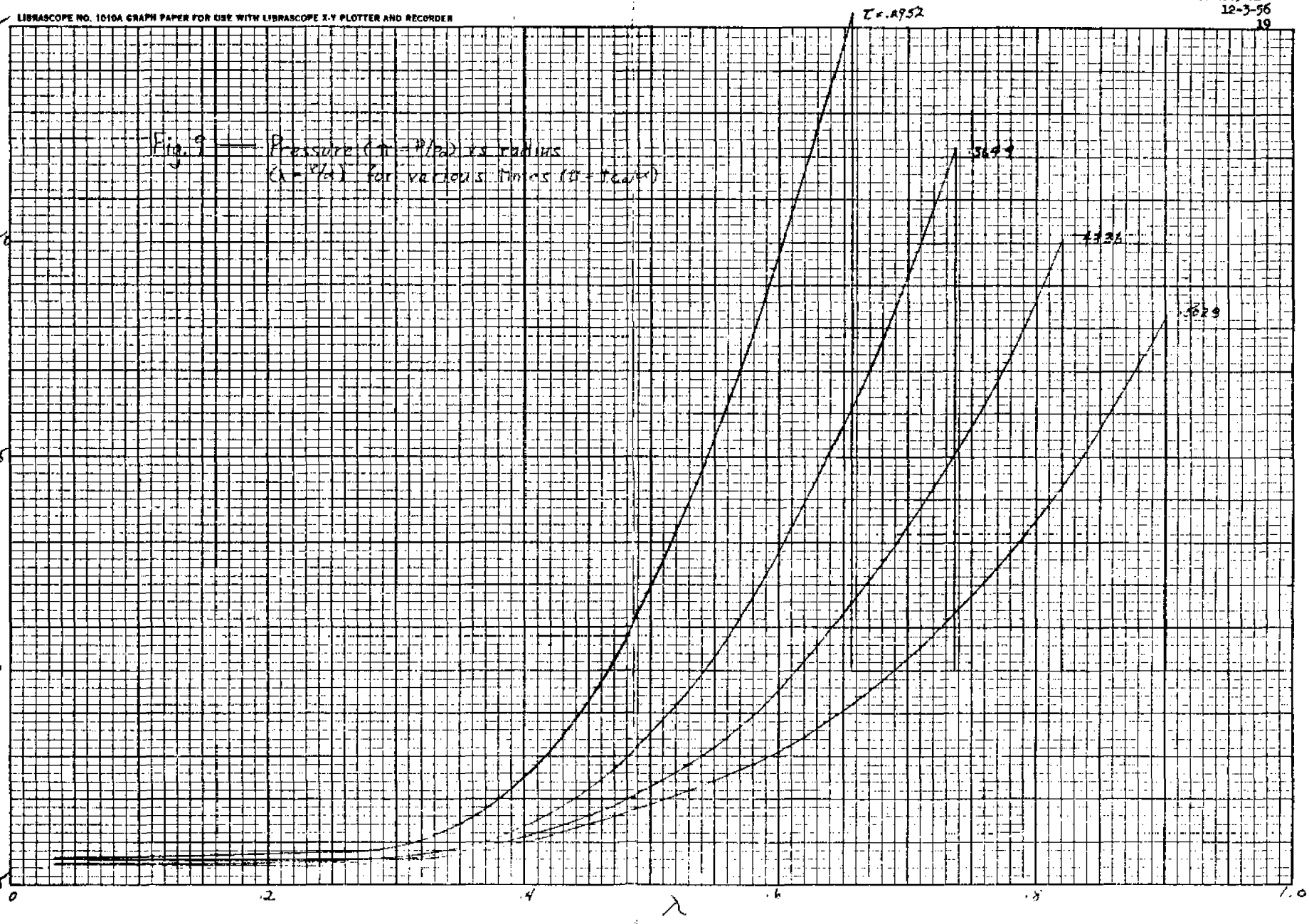

Fig. 9 — Pressure ($\pi = P/\rho a^2$) vs radius ($\lambda = r/a$) for various times ($\tau = t c_0/a$)

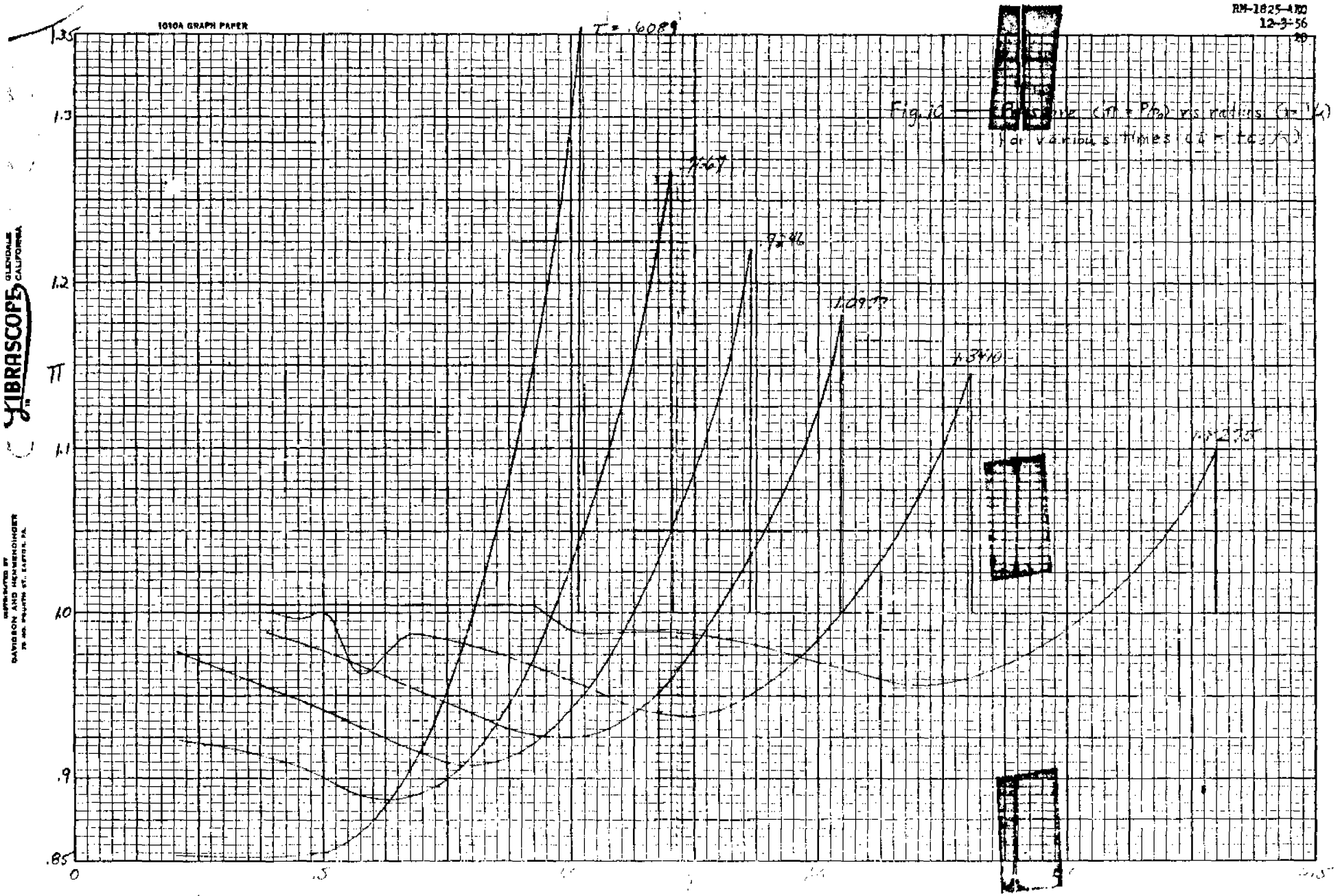

Fig. 10 — Pressure ($\pi = P/P_0$) vs radius ($r = r/r_0$) for various times ($\tau = t c_0 / r_0$)

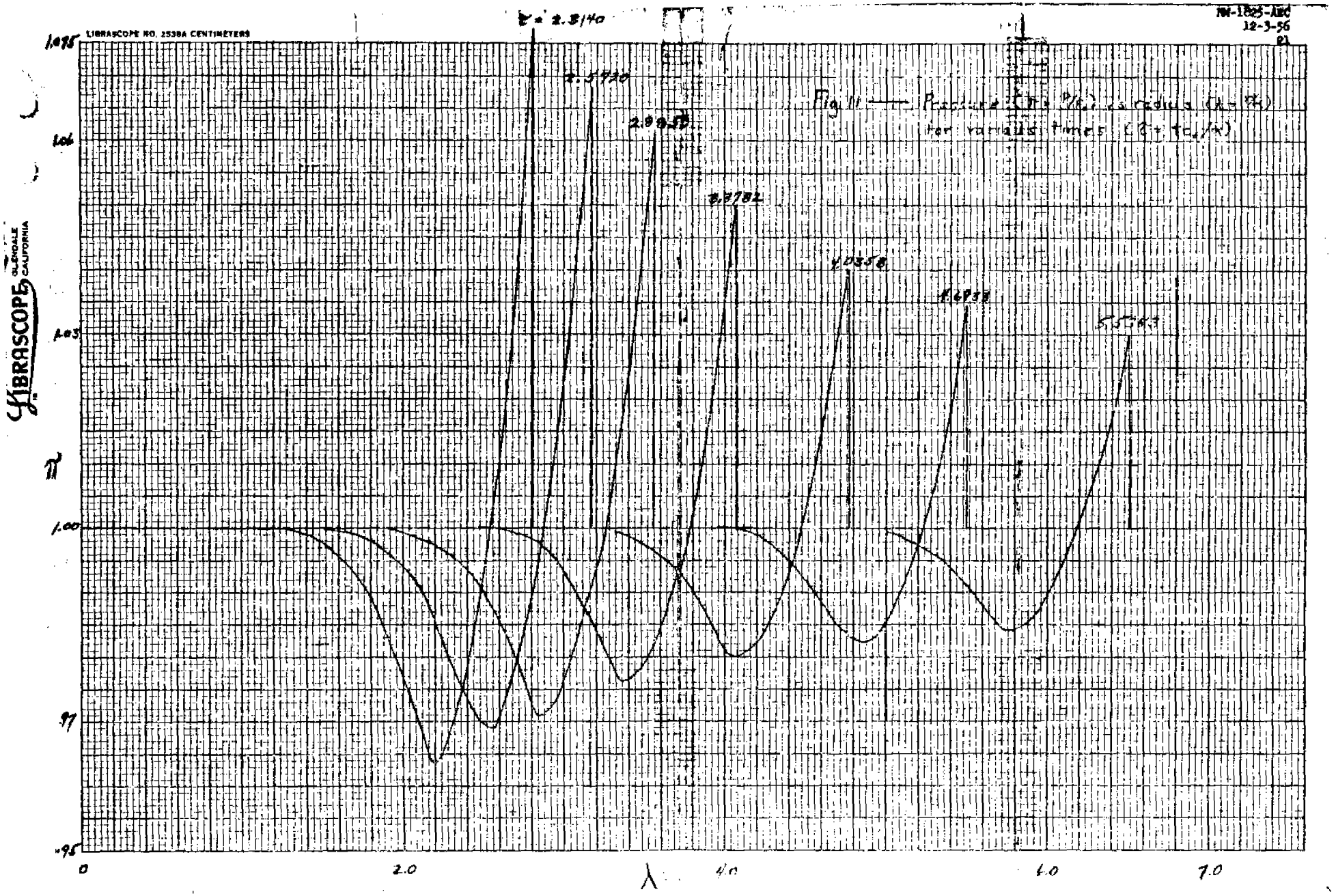

Fig. 11 — Pressure (P/P_0) as a radius ($R_0 = r/r_0$) for various times ($\tau = t c_0 / r_0$)

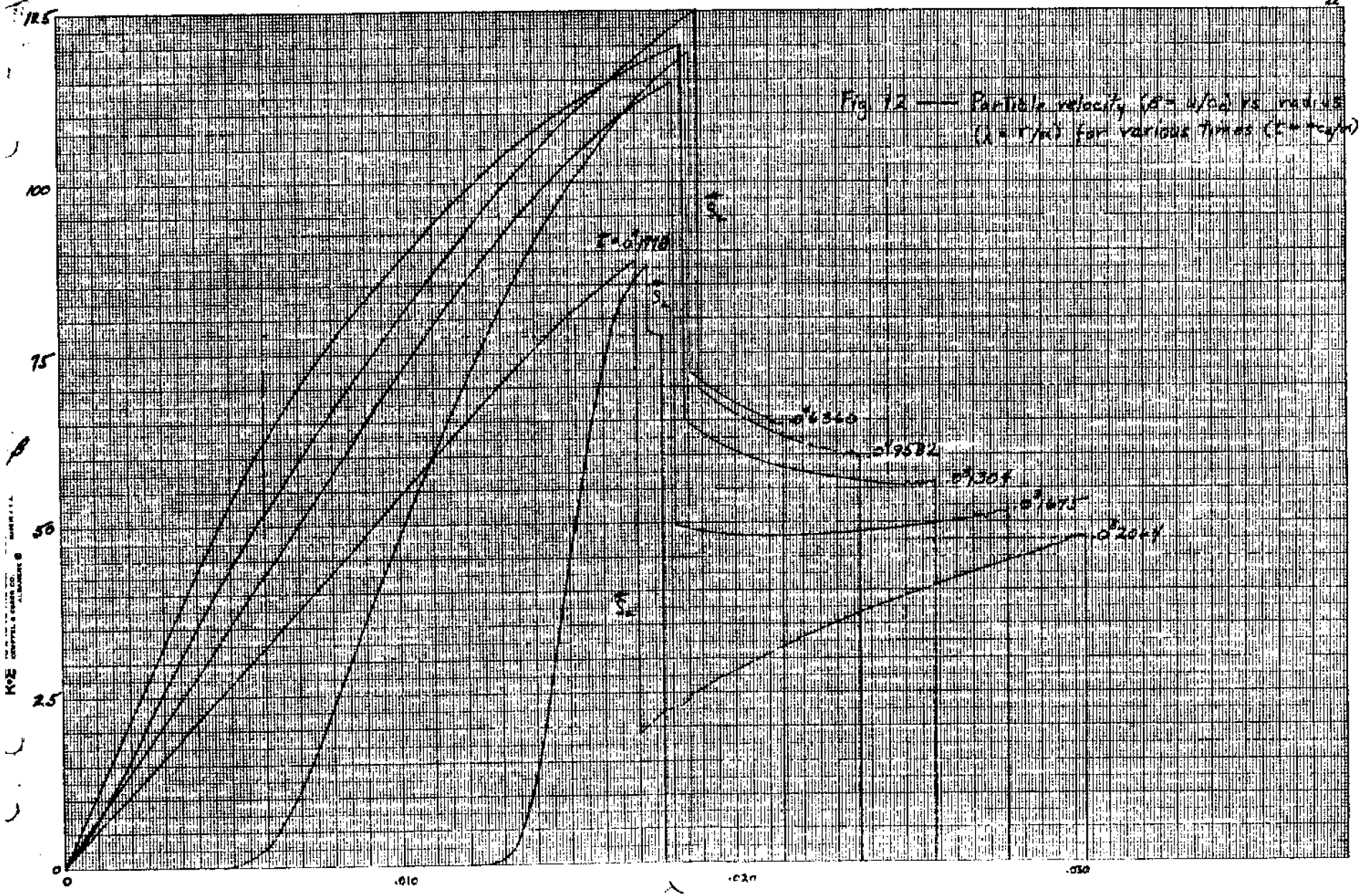

Fig. 12 — Particle velocity ($\beta = u/c_0$) vs. radius ($\lambda = r/R$) for various times ($\tau = tc_0/R$)

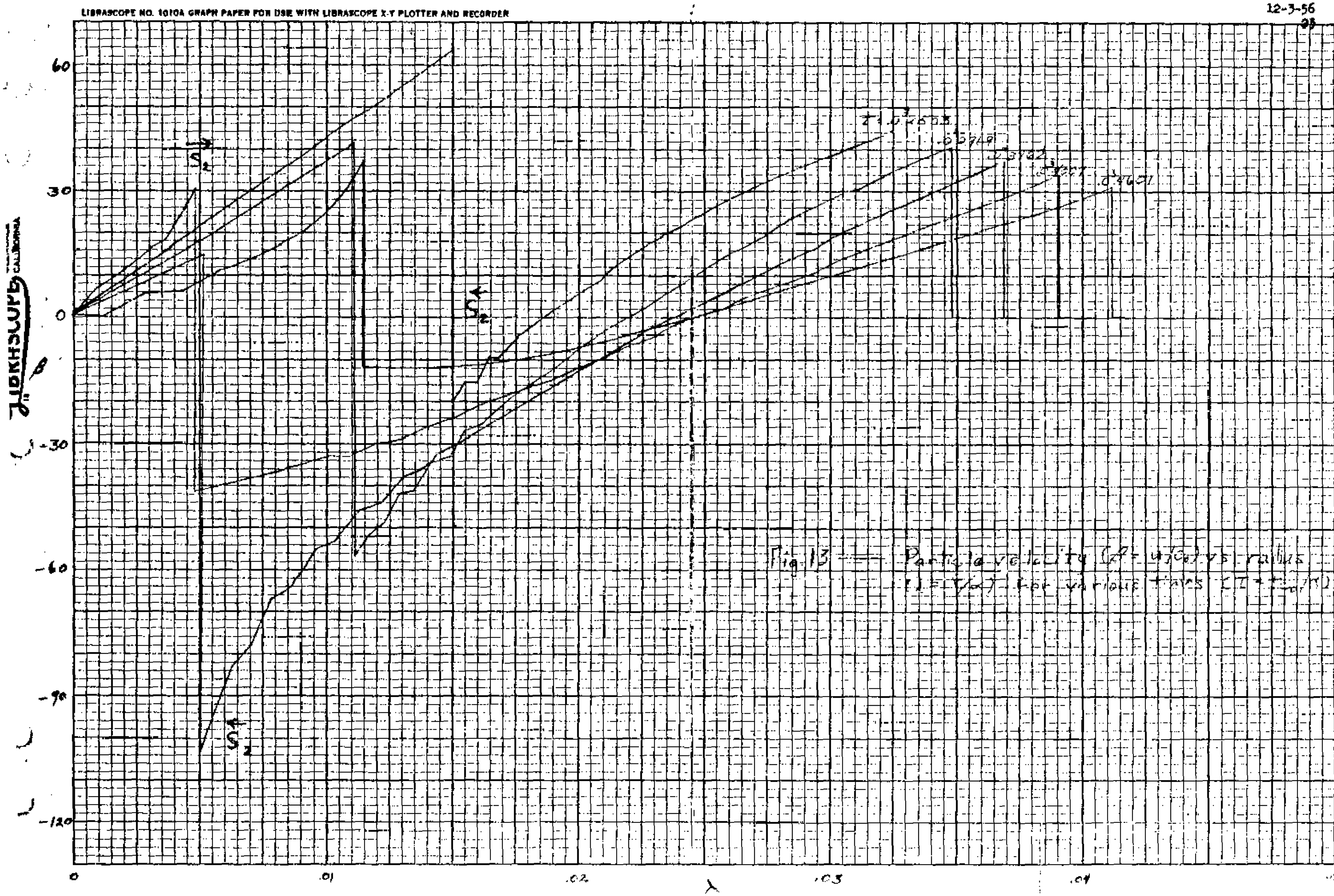

Fig. 13 — Particle velocity ($\beta = u/c_0$) vs radius $\lambda = r/(c_0 T)$ for various times ($\tau = t c_0/R$)

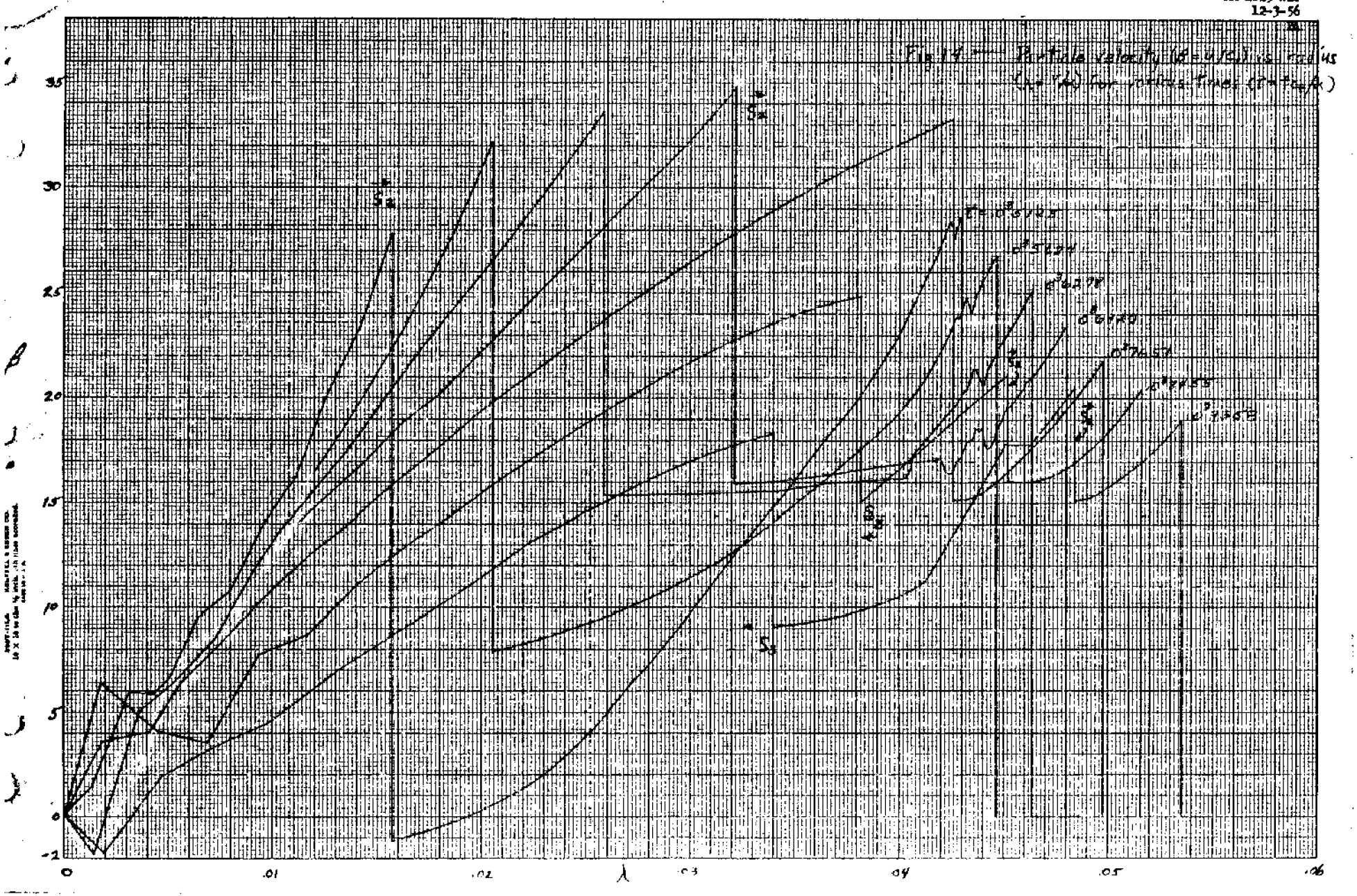

Fig. 14 — Particle velocity ($\beta = v/c$) vs. radius ($\lambda = r_0/\lambda$) for various times ($\tau = t c/\lambda$)

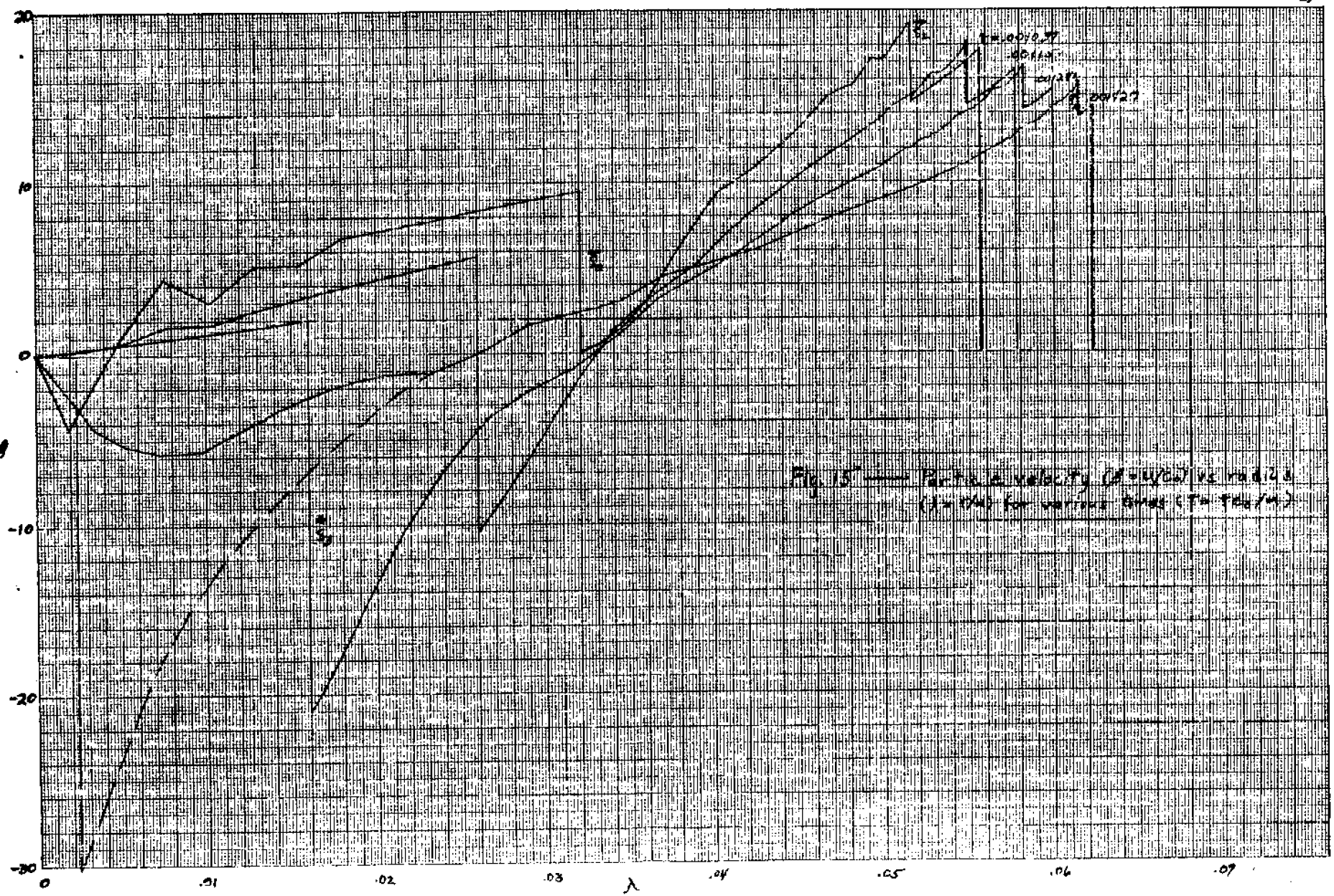

Fig. 15 — Particle velocity, $(\beta = w/u_0)$ vs radius $(\lambda = r/a)$ for various times $(\tau = tc_0/a)$

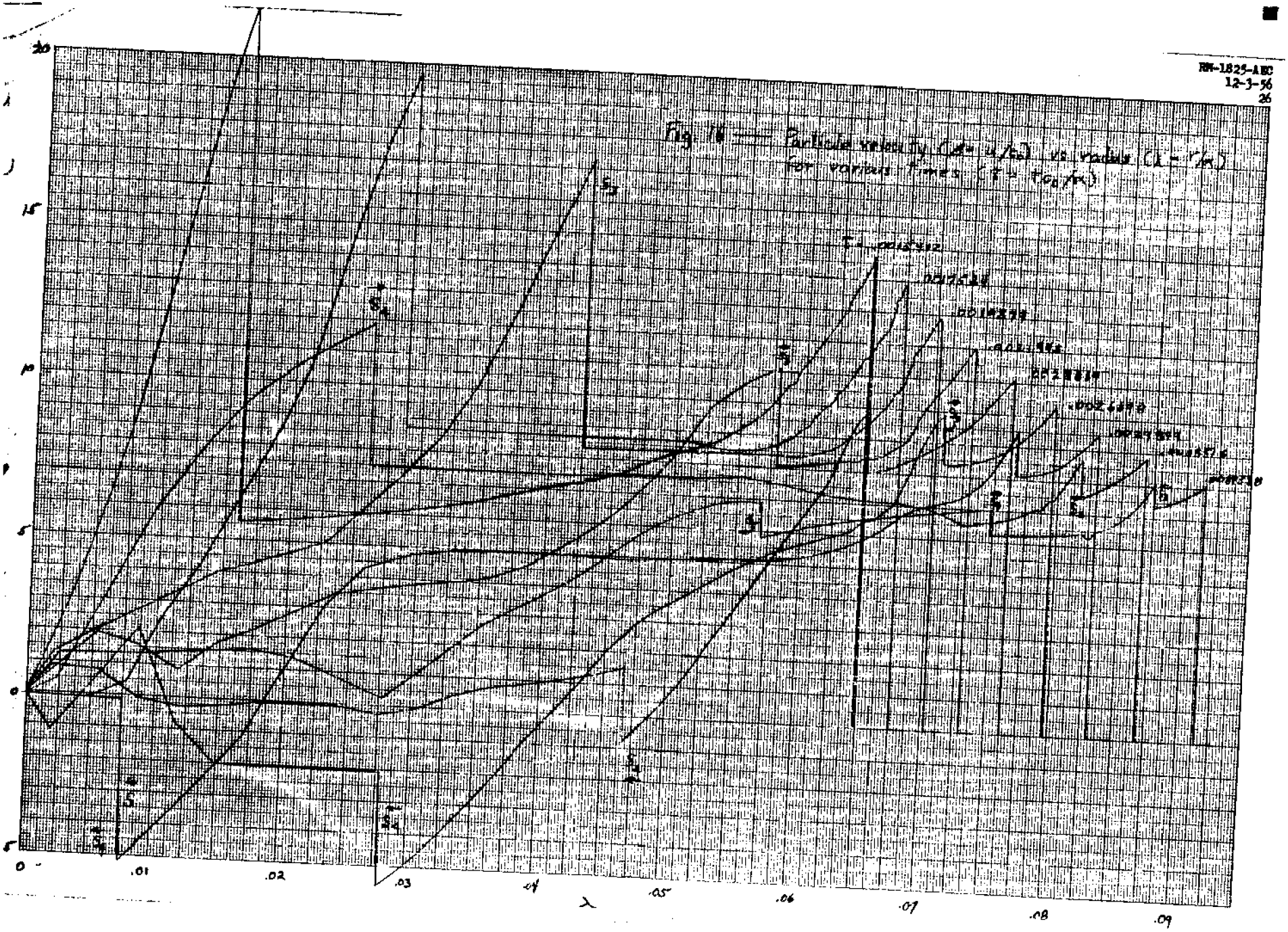

Fig. 16 — Particle velocity (u/c_0) vs radius ($\lambda = r/r_0$) for various times ($\tau = t c_0/r_0$)

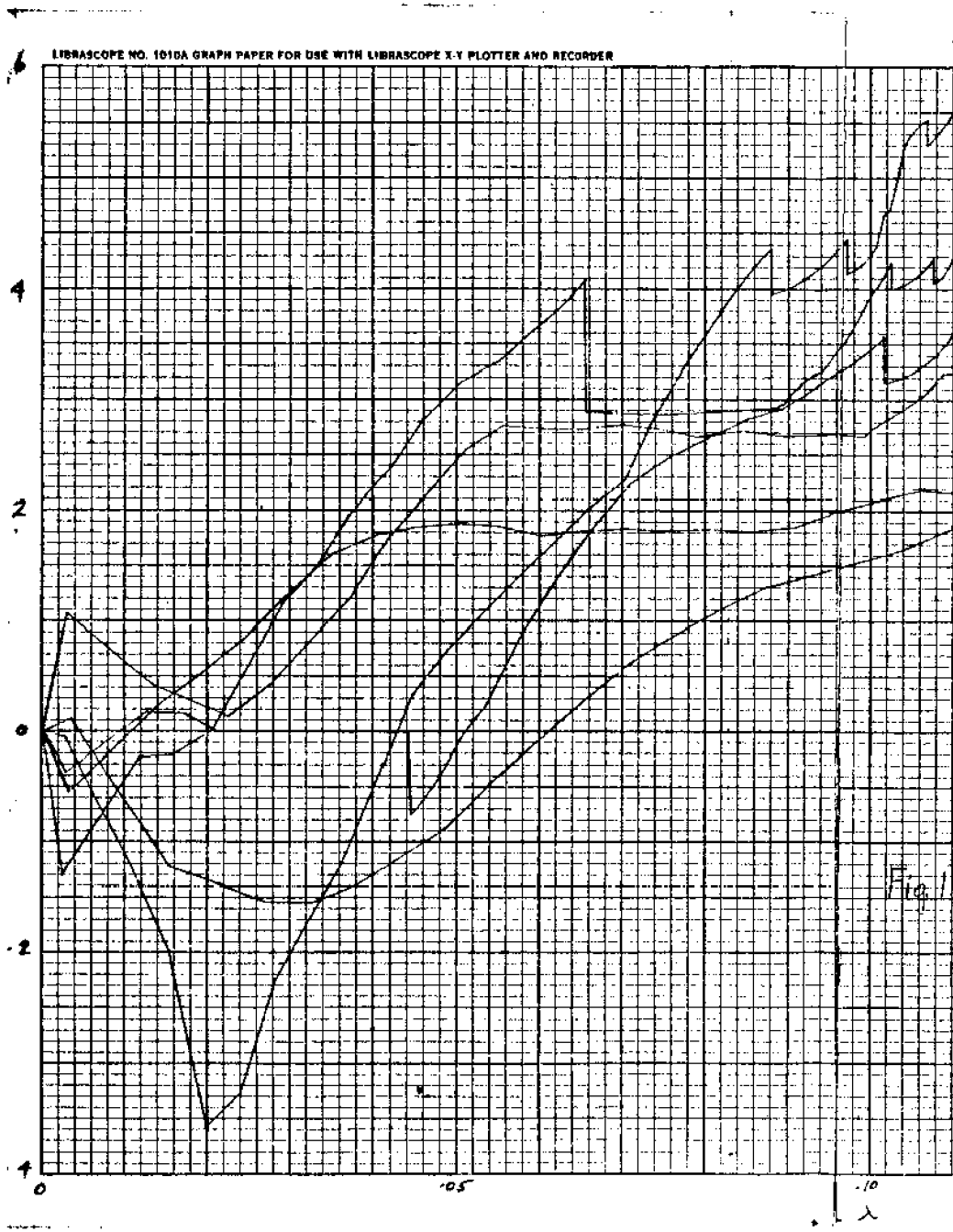
LIBRASCOPE NO. 1010A GRAPH PAPER FOR USE WITH LIBRASCOPE X-Y PLOTTER AND RECORDER
6
4
2
0
-2
-4
0
.05
.10
λ
Fig 1

$\tau = .006334$

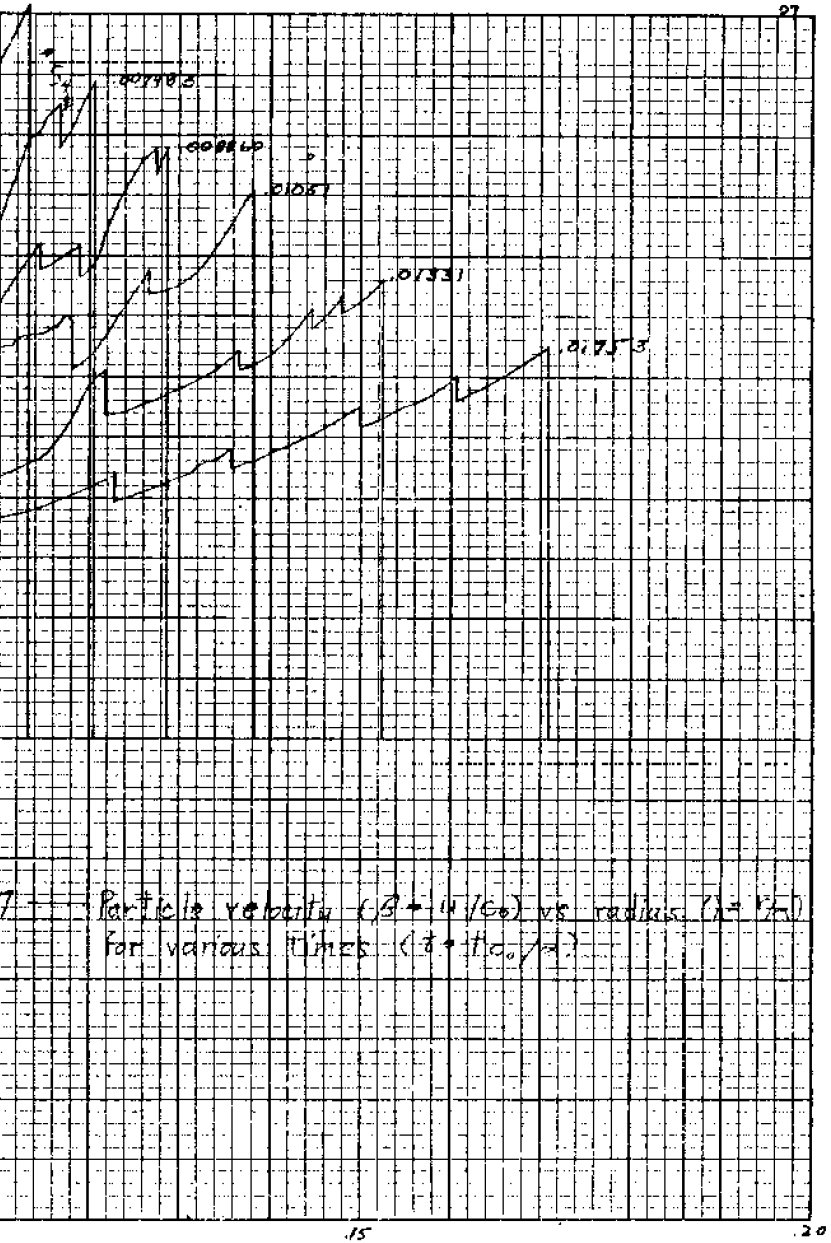

7 — Particle velocity ($\beta = u/c_0$) vs radius ($\gamma = r/r_0$) for various times ($\delta = t c_0/r_0$)

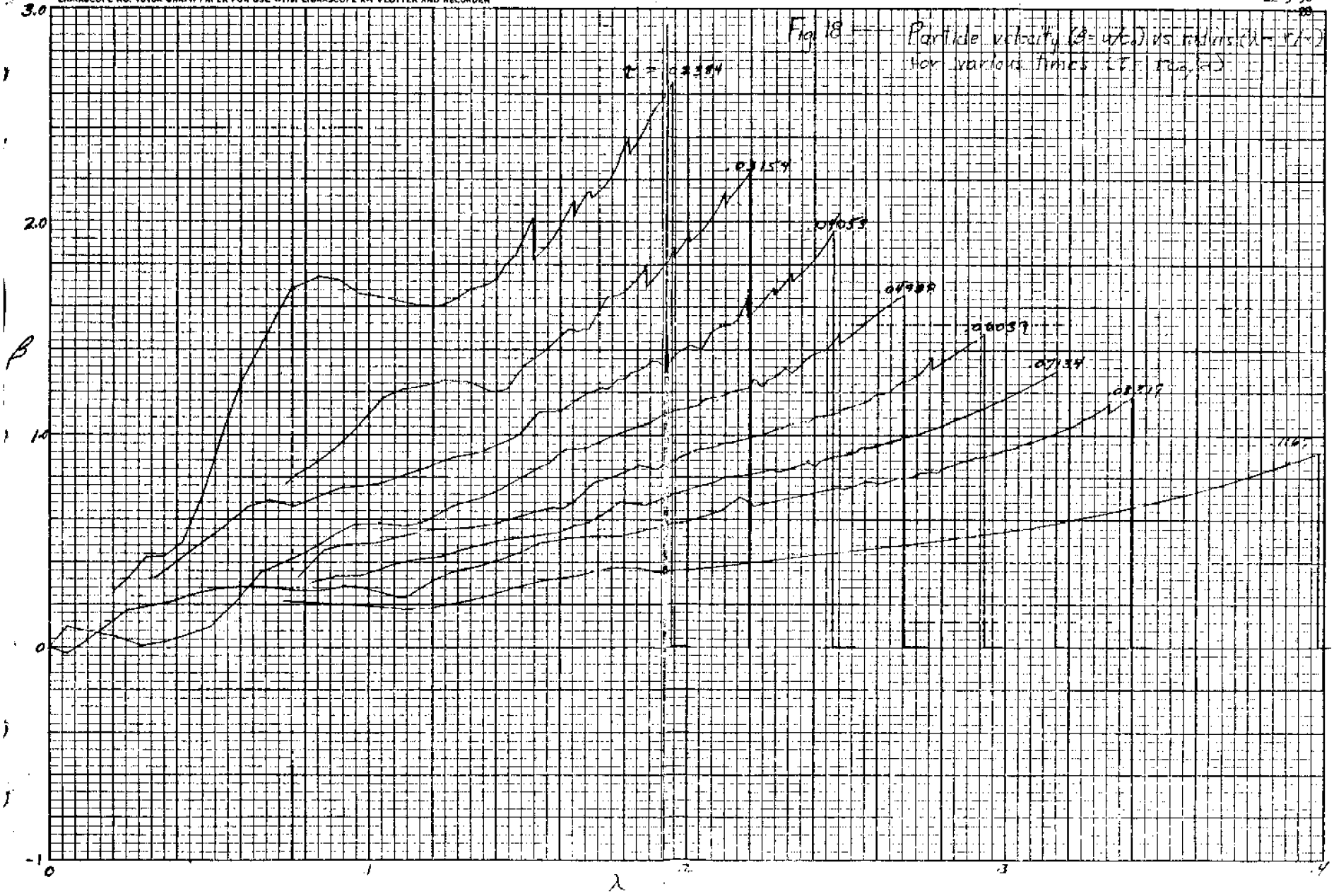

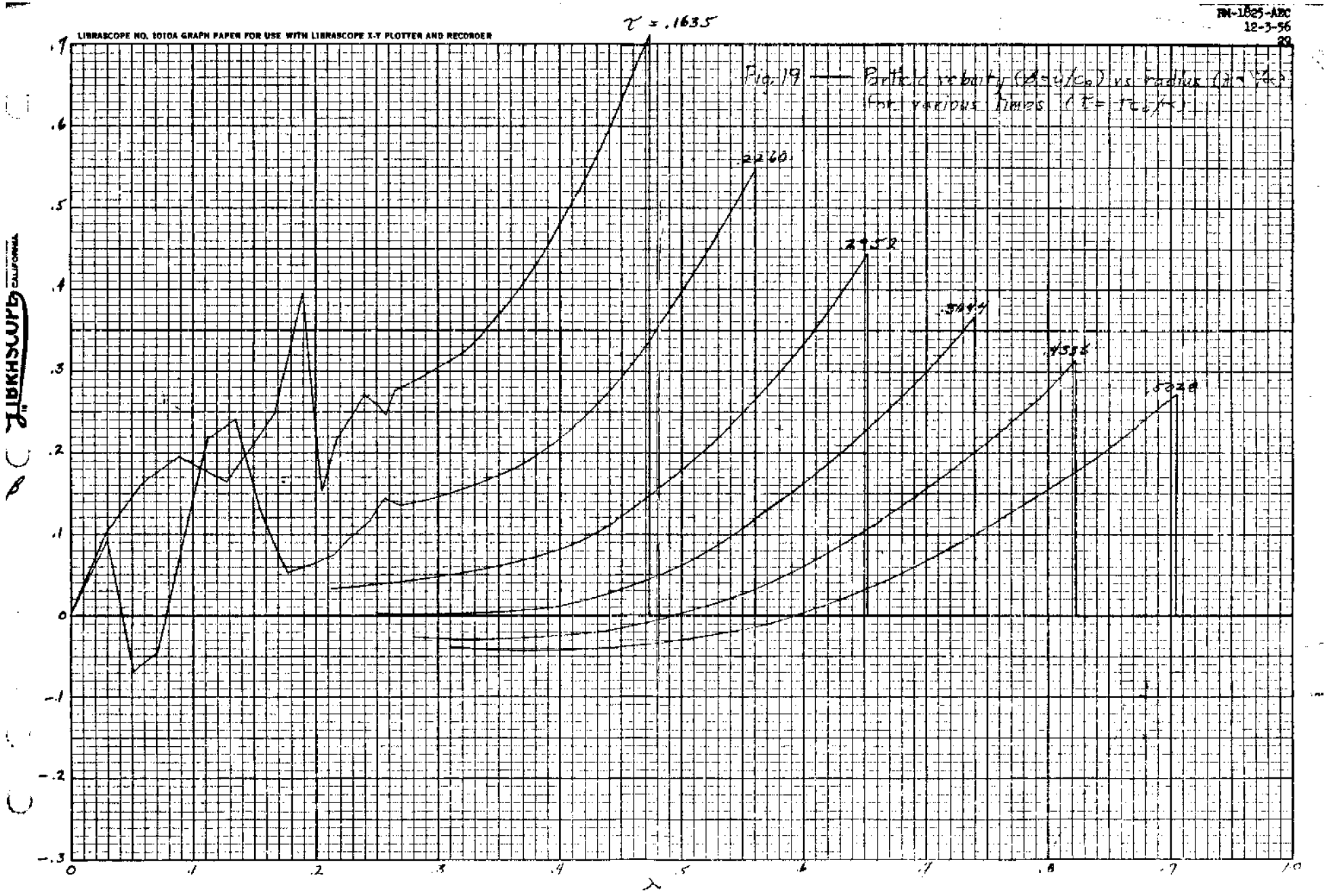

Fig. 19 — Particle velocity ($\beta = v/c_0$) vs radius ($\lambda = r/r_0$) for various times ($\tau = tc_0/r_0$).

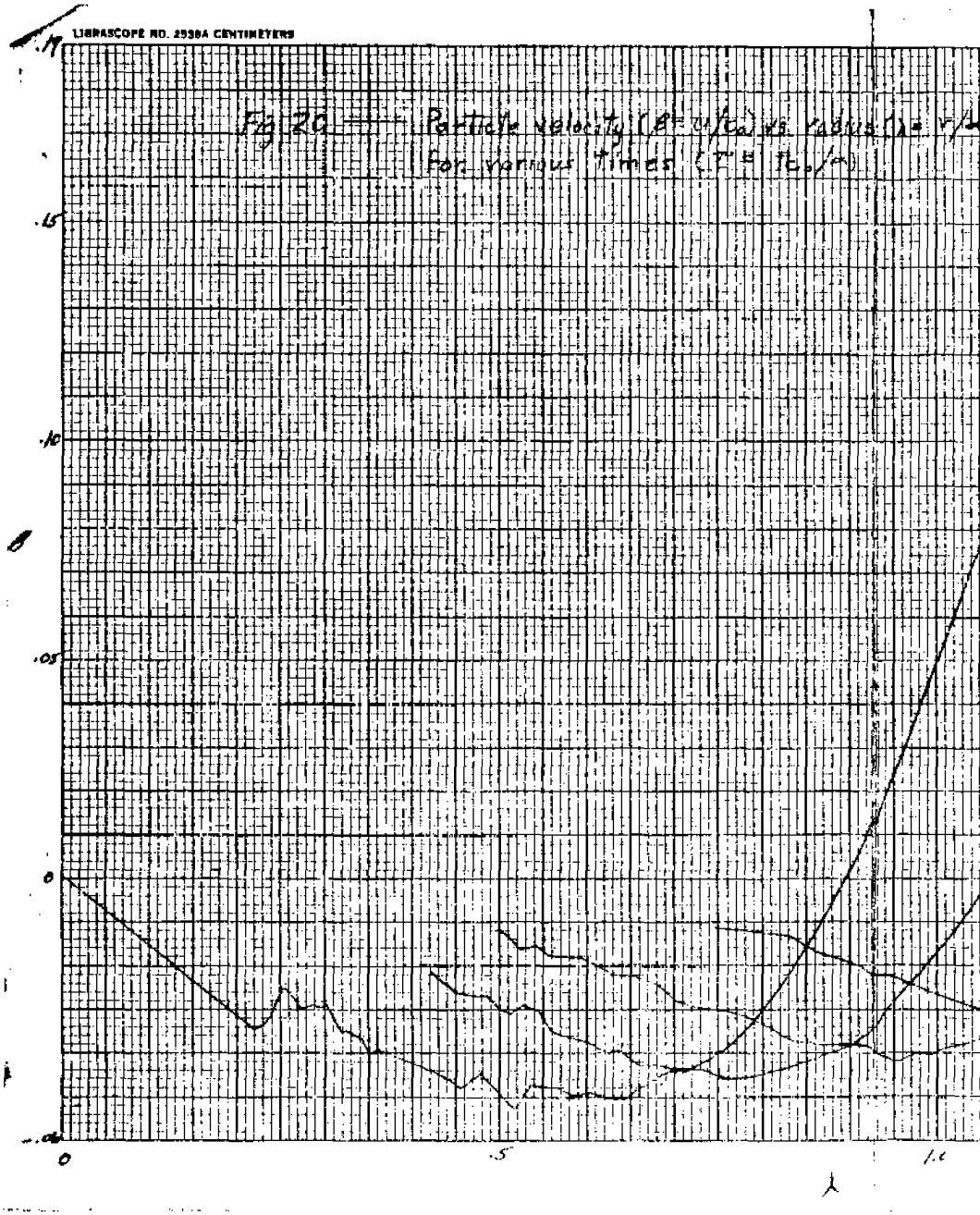
LIBRASCOPE NO. 2930A CENTIMETERS
Fig 20 — Particle velocity (β = u/c₀) vs. radius (λ = r/a)
for various times (τ = tc₀/a)
.15
.10
β
.05
0
0
.5
1.0
λ

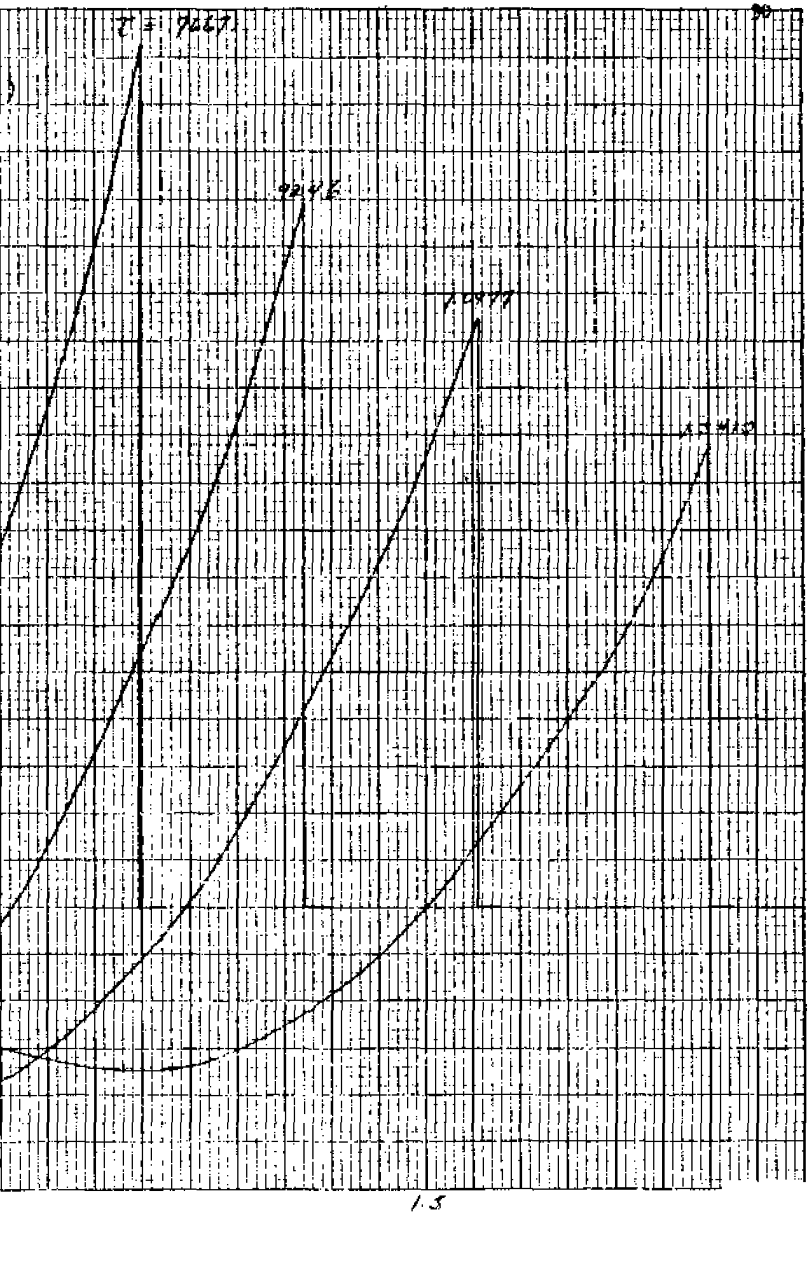
τ = .9227
.9242
1.5

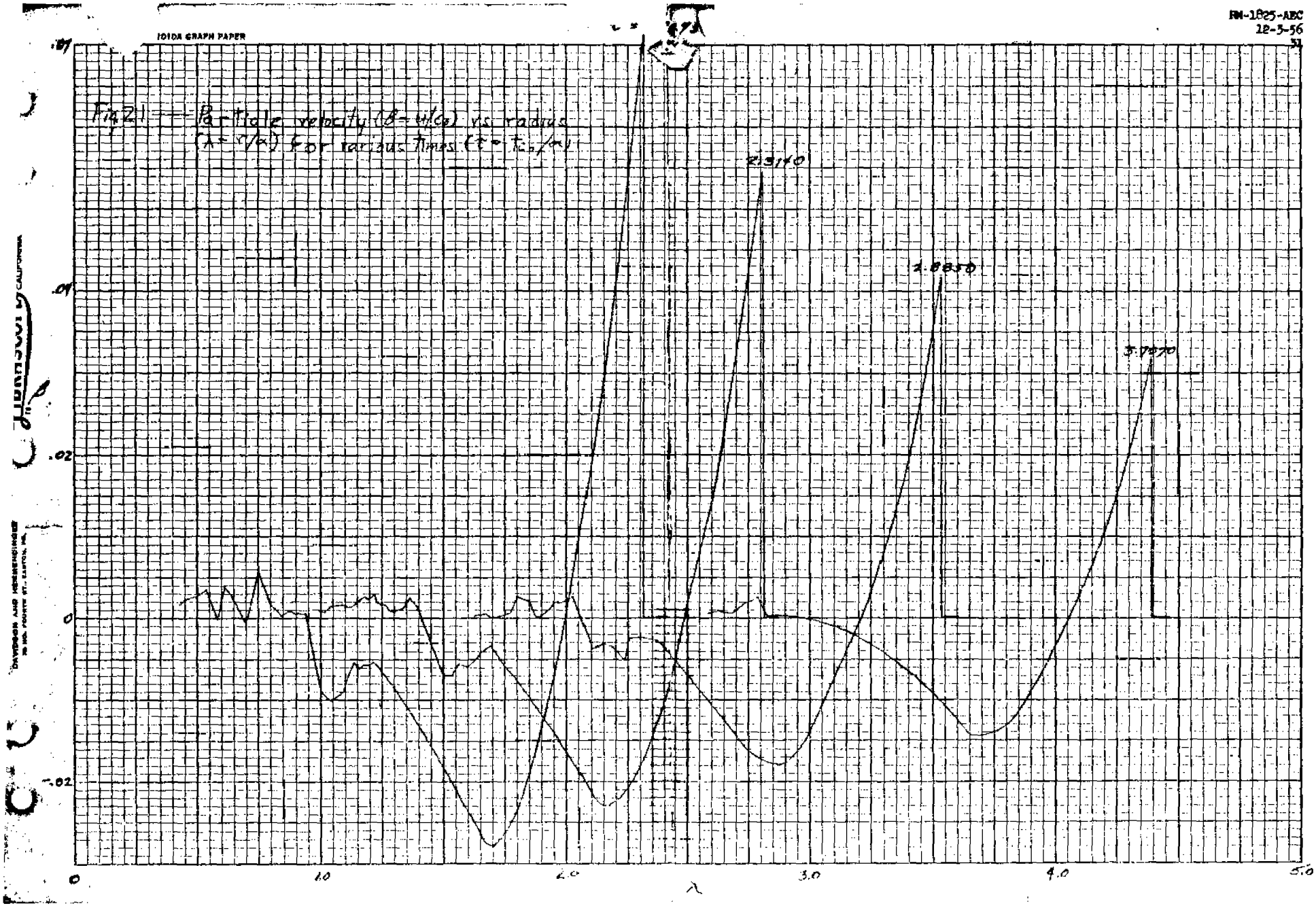
1010A GRAPH PAPER
Fig 21 — Particle velocity (β = v/c) vs radius (λ = r/a) for various times (τ = t c/a)
2.9140
1.8830
3.7870
.04
.02
0
-.02
1.0
2.0
3.0
4.0
5.0
λ

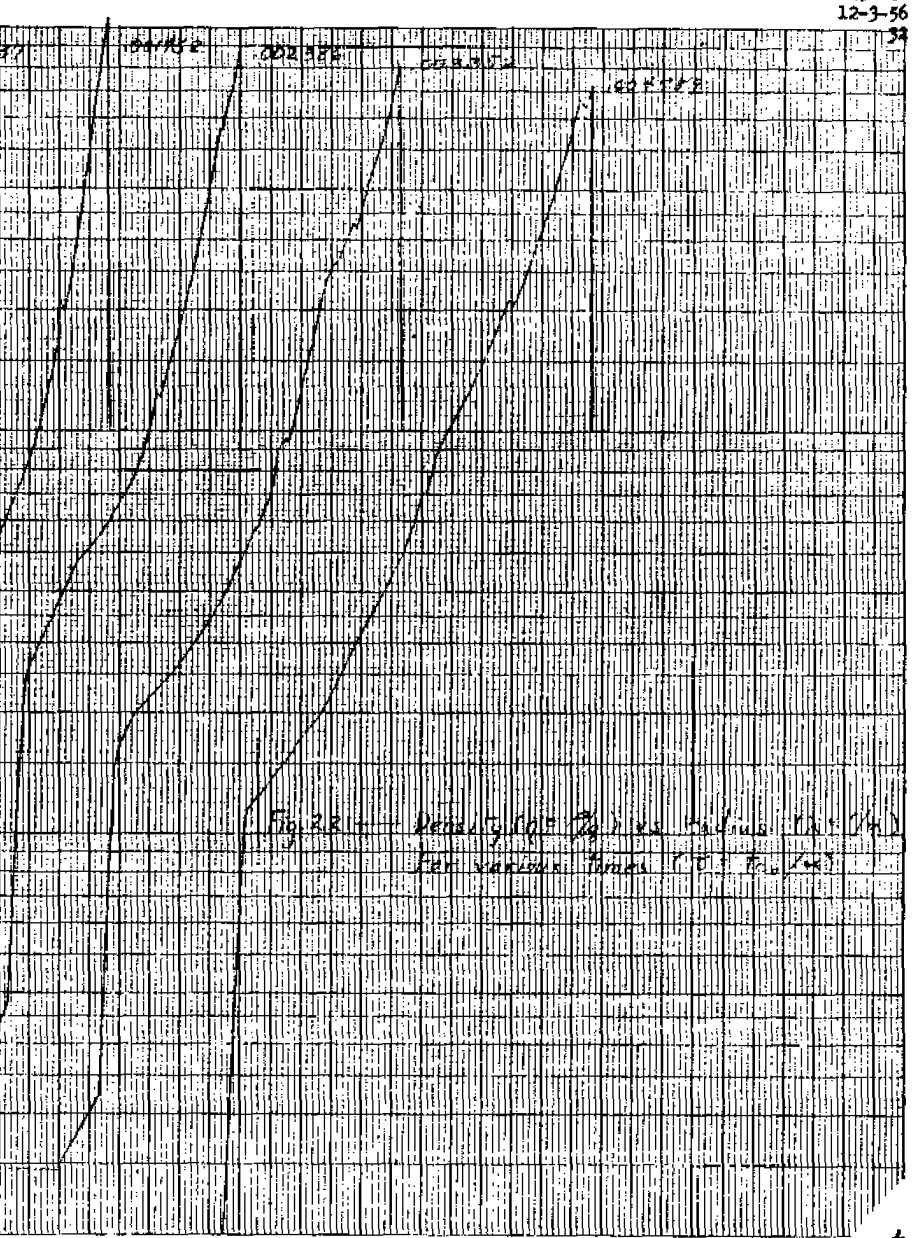

Fig. 22 — Density [ρ/ρ_0] vs. radius [r/r_0] for various times [t]

0
.02
.04
.06
.08
.10
.12
.14
.16
.18
.20
.22
.24
.26
.28
.30
.32
.34
.36
.38
.40
.42
.44
.46
.48
.50
.52
.54
.56
.58
.60
.62
.64
.66
.68
.70
.72
.74
.76
.78
.80
.82
.84
.86
.88
.90
.92
.94
.96
.98
1.00

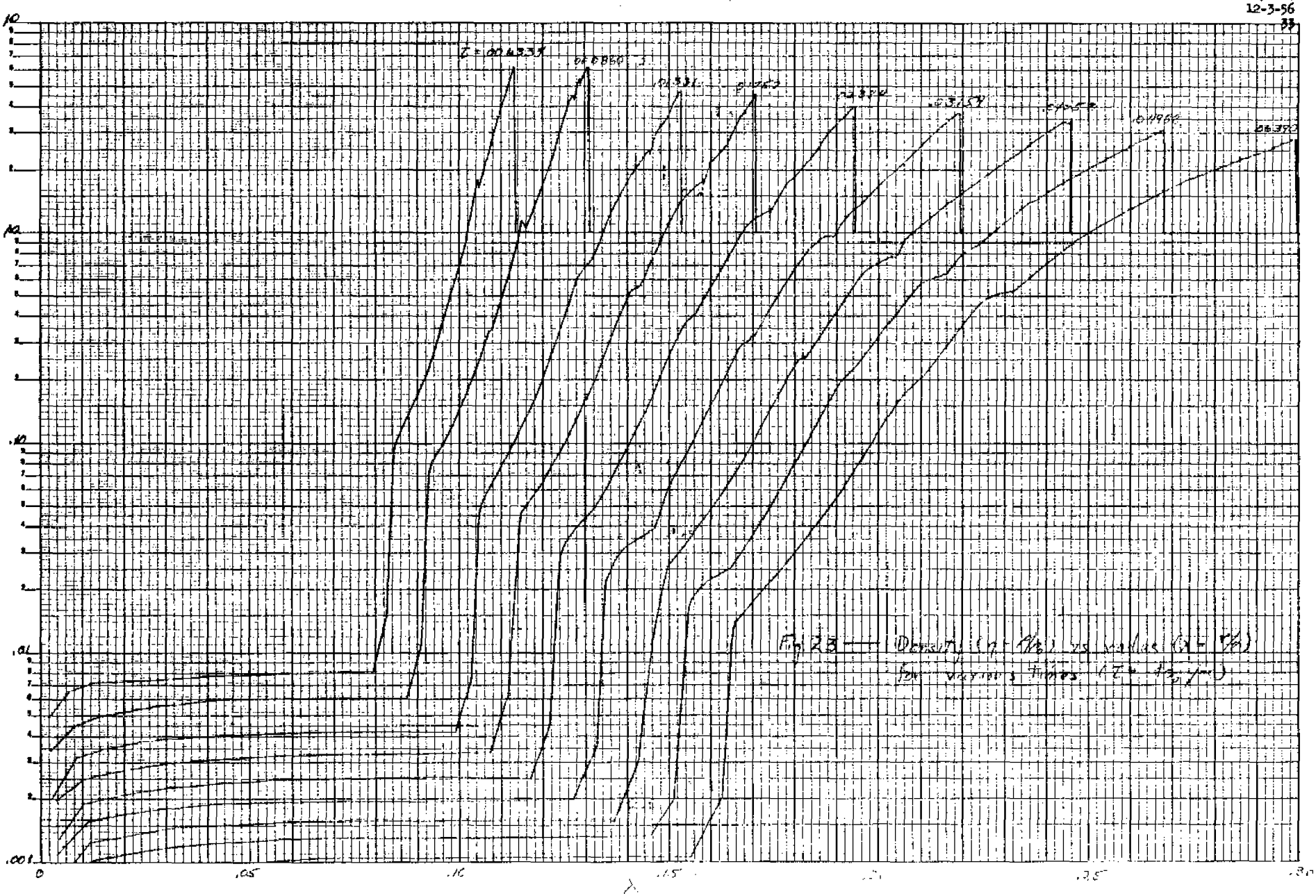

Fig 28 — Density ($\eta - \eta_0$) vs wavelength ($\lambda - \lambda_0$)
for various times ($t - t_0$, μsec)

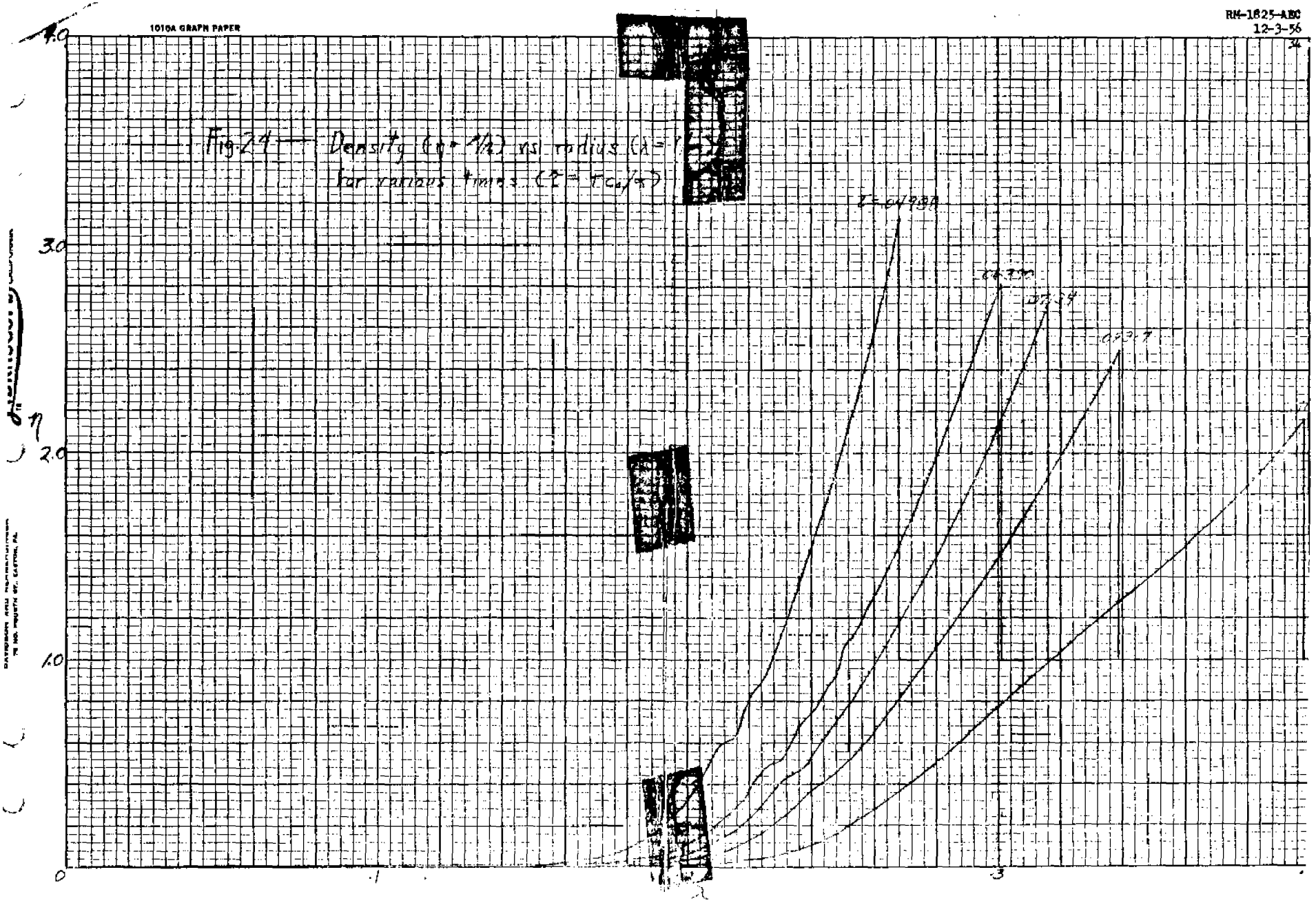

Fig. 24 — Density ($\rho^* = \rho/\rho_0$) vs radius ($\lambda = r/r_0$) for various times ($\tau = t c_0/r_0$)

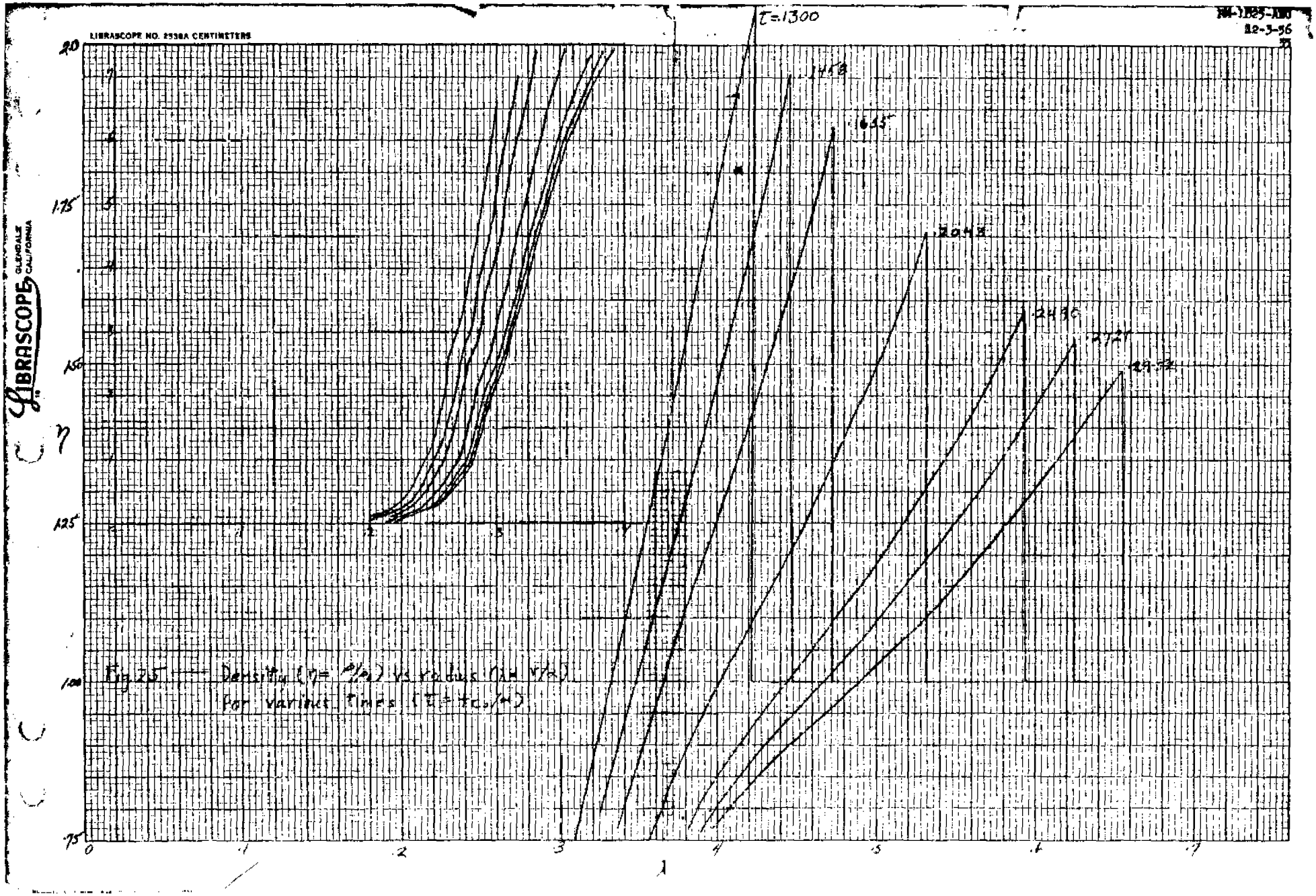

Fig 25 — Density ($\eta = \rho/\rho_0$) vs radius ($\lambda = r/r_0$)
For various times ($\tau = t c_0/r_0$)

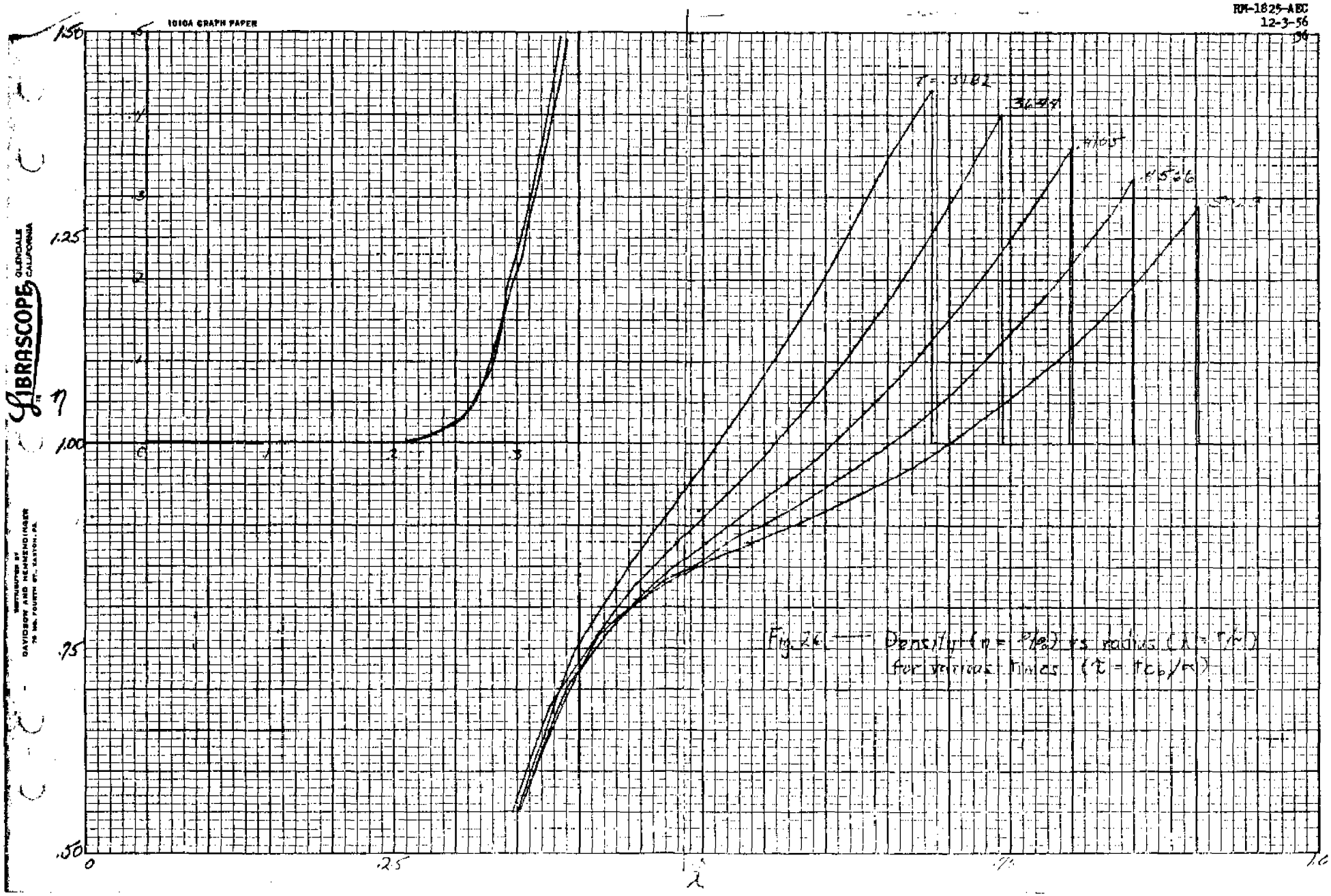

Fig. XX — Density ($\eta = \rho/\rho_0$) vs radius ($\lambda = r/r_c$) for various times ($\tau = t c_0/r_c$)

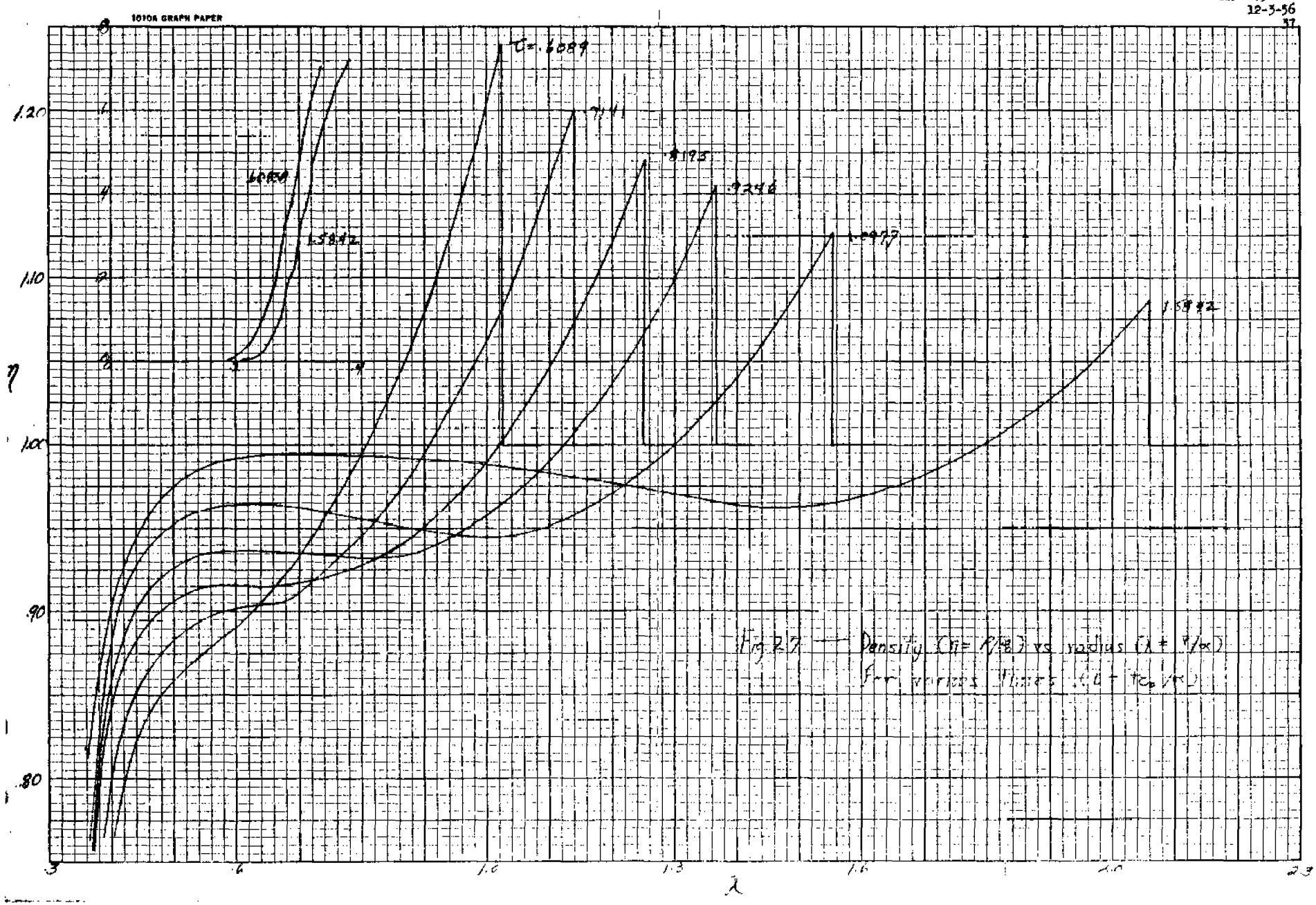

Fig 2.7 — Density ($\eta = \rho/\rho_0$) vs. radius ($\lambda = r/r_0$) for various flows ($C = \dot{m}/\rho_0 r_0$)

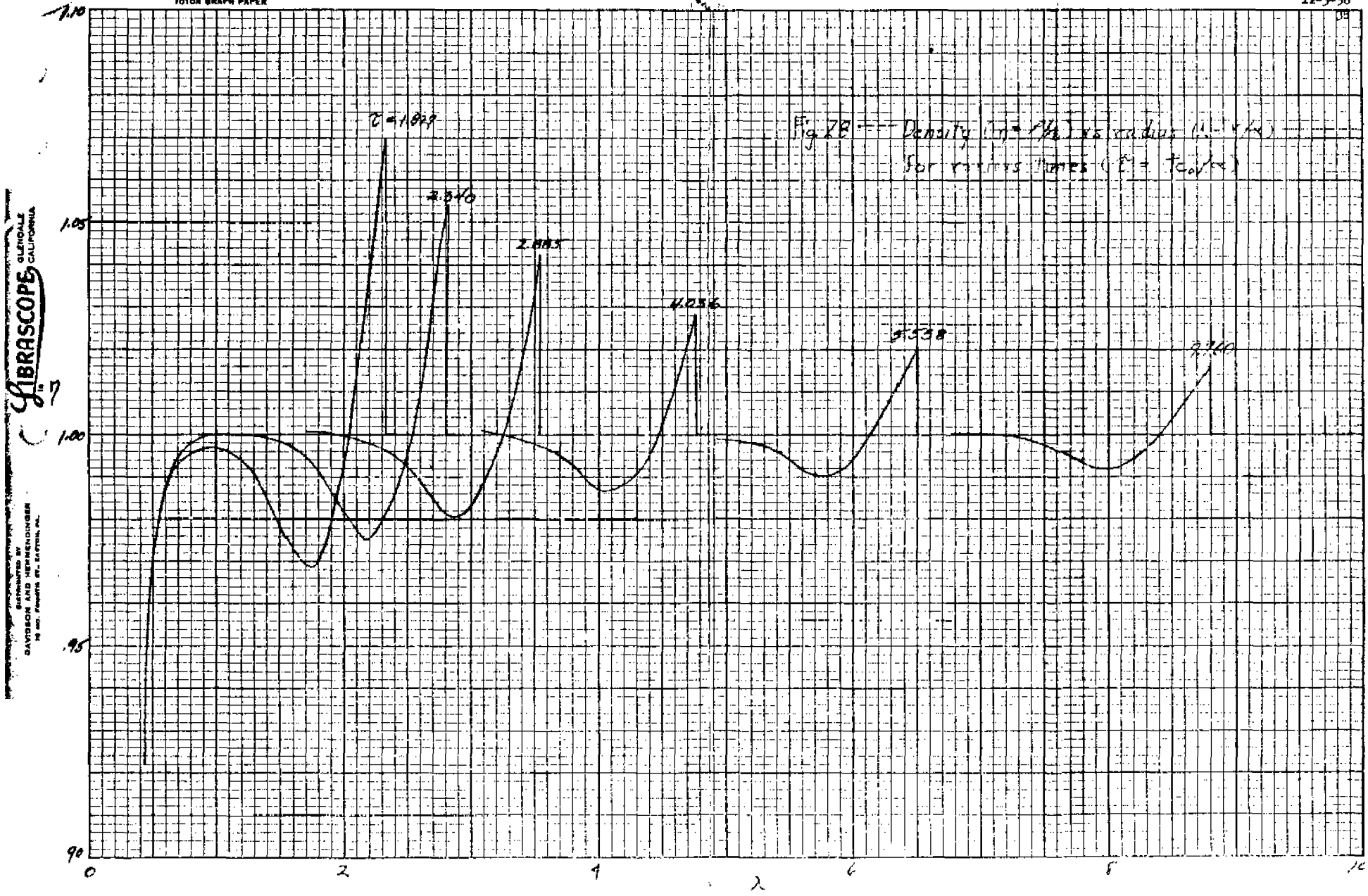

Fig 28 — Density ($\eta = \rho/\rho_0$) vs radius ($\lambda = r/r_0$) for various times ($\tau = t c_0/r_0$)

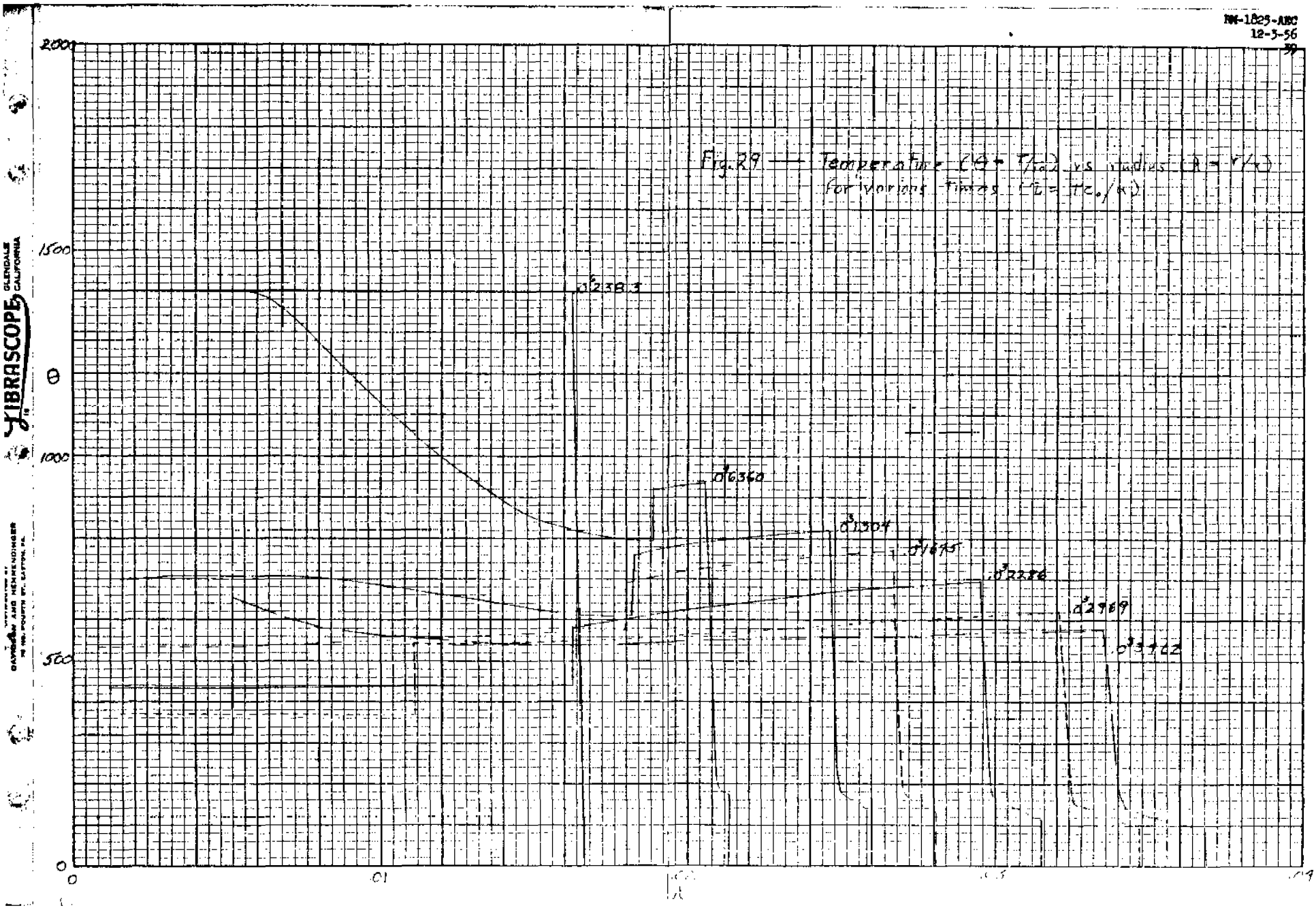

Fig. 29 — Temperature ($\theta = T/T_{ad}$) vs radius ($\alpha = r/r_0$) for various times ($\tau = t c_0/r_0$)

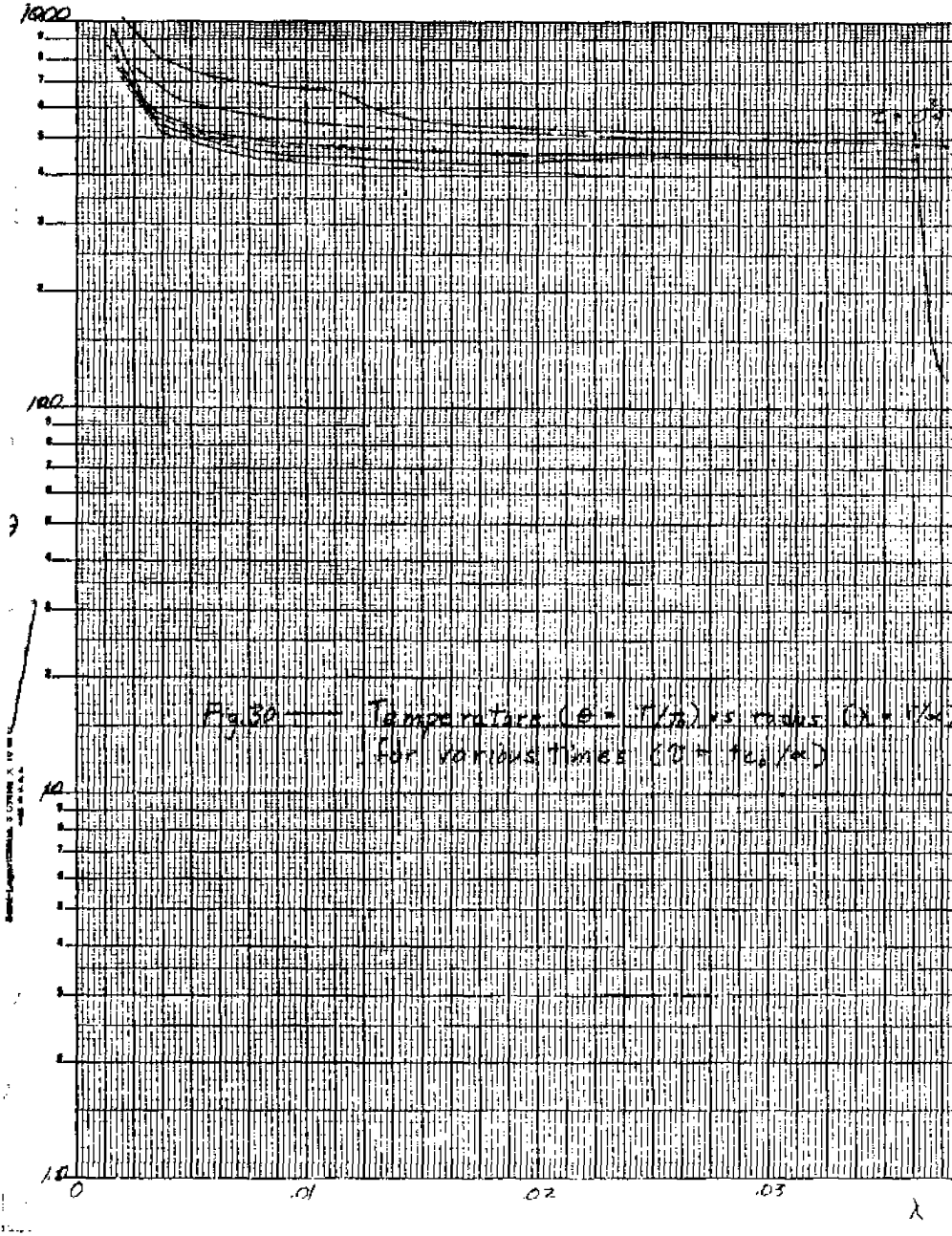

Fig. 30 — Temperature ($\theta = T/T_0$) vs radius ($\lambda = r/r_0$) for various Times ($\tau = t\alpha_0/r_0^2$)

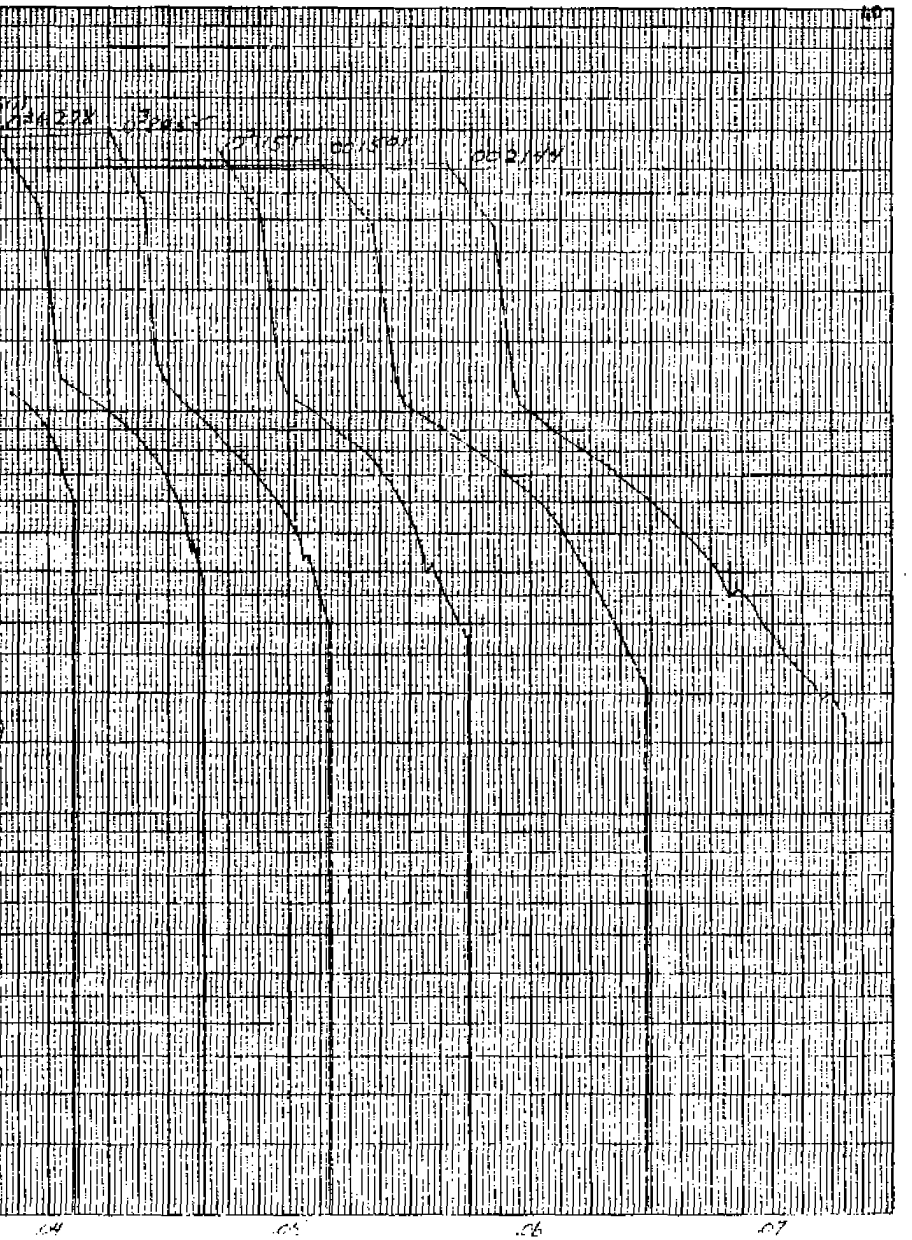

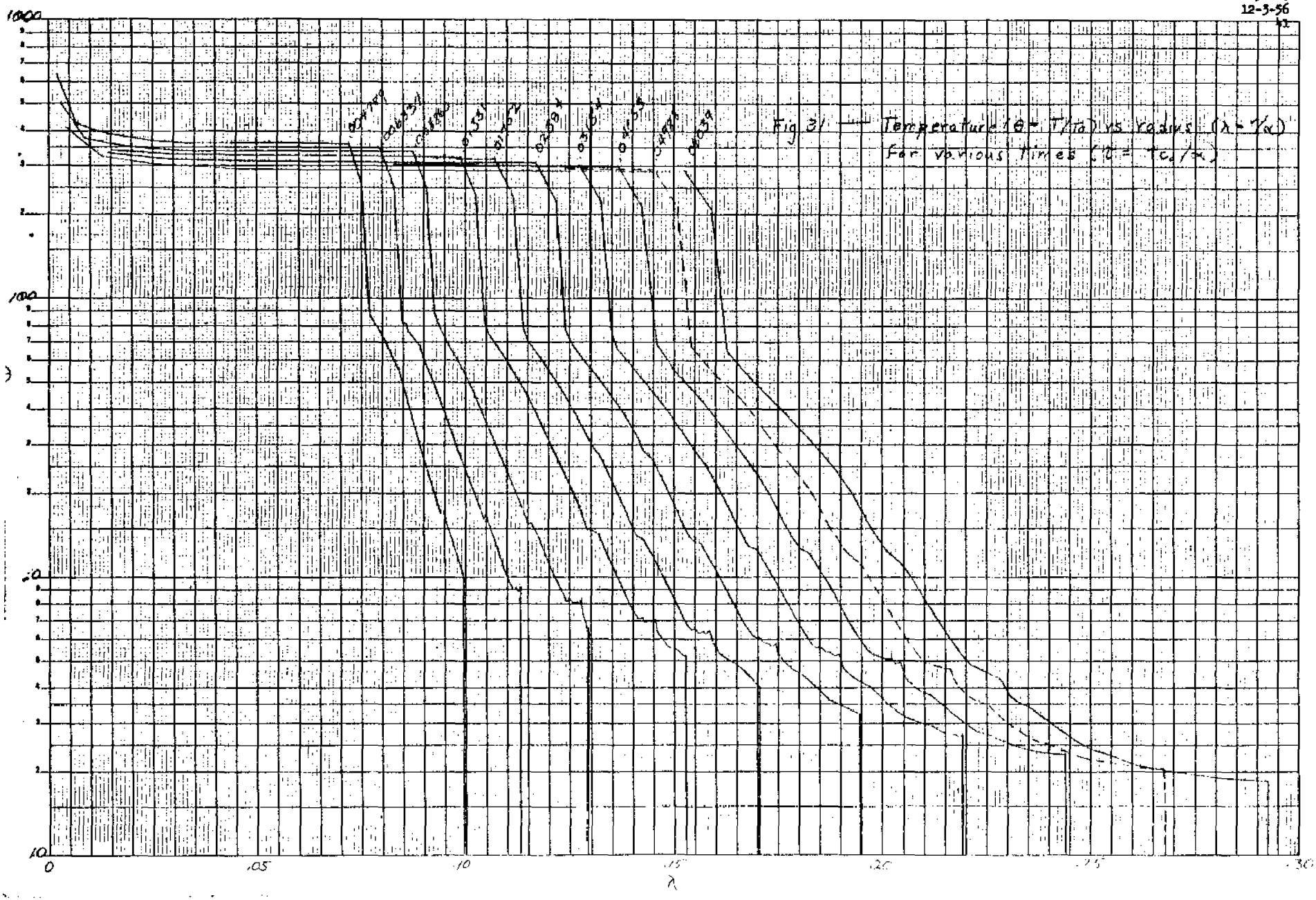

Fig 31 — Temperature ($\theta = T/T_0$) vs radius ($\lambda = r/a$) for various times ($\tau = t c_1/a$)

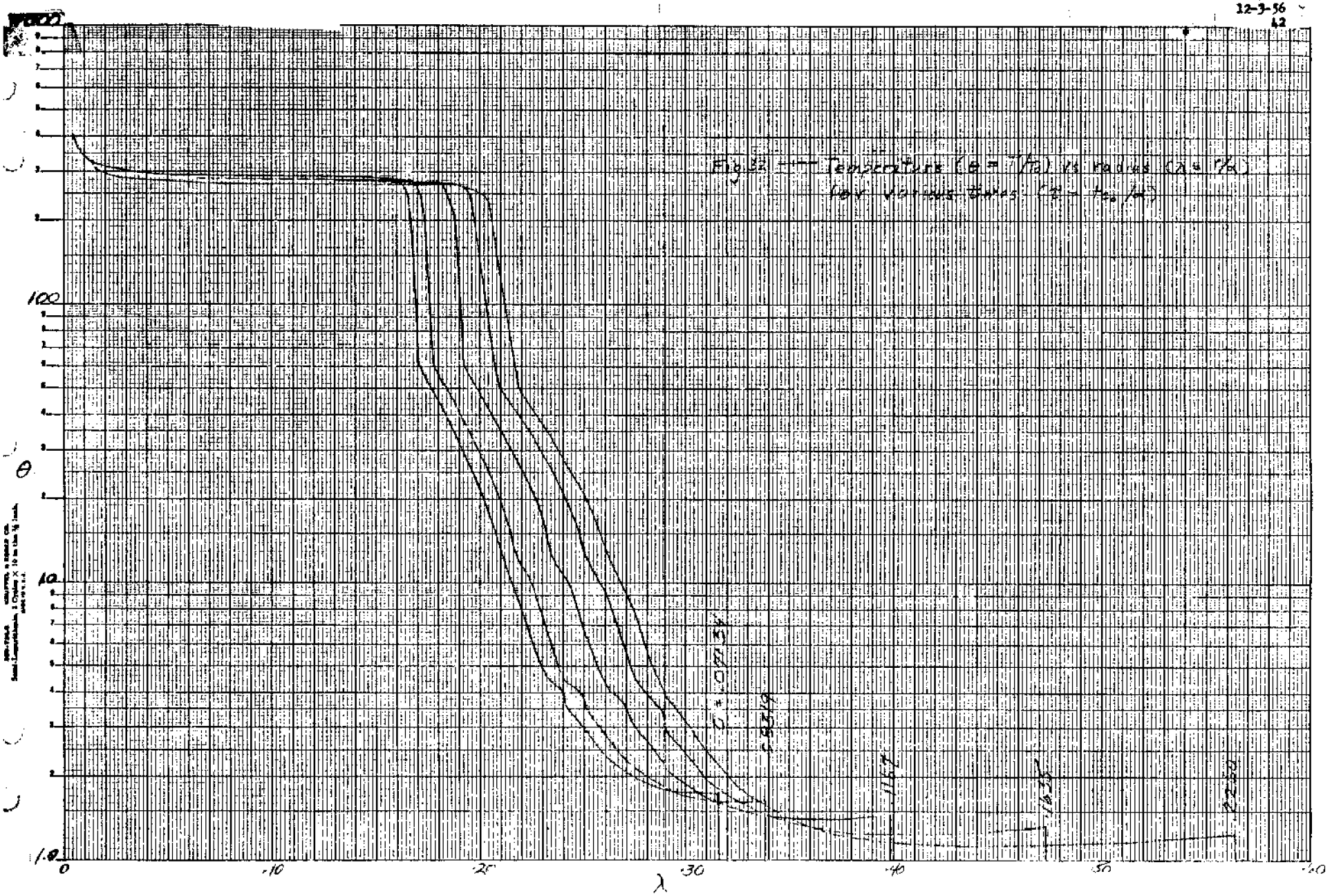

Fig. 22 — Temperature ($\theta = T/T_0$) vs radius ($\lambda = r/r_0$) for various times ($\tau = kt_0/r_0^2$)

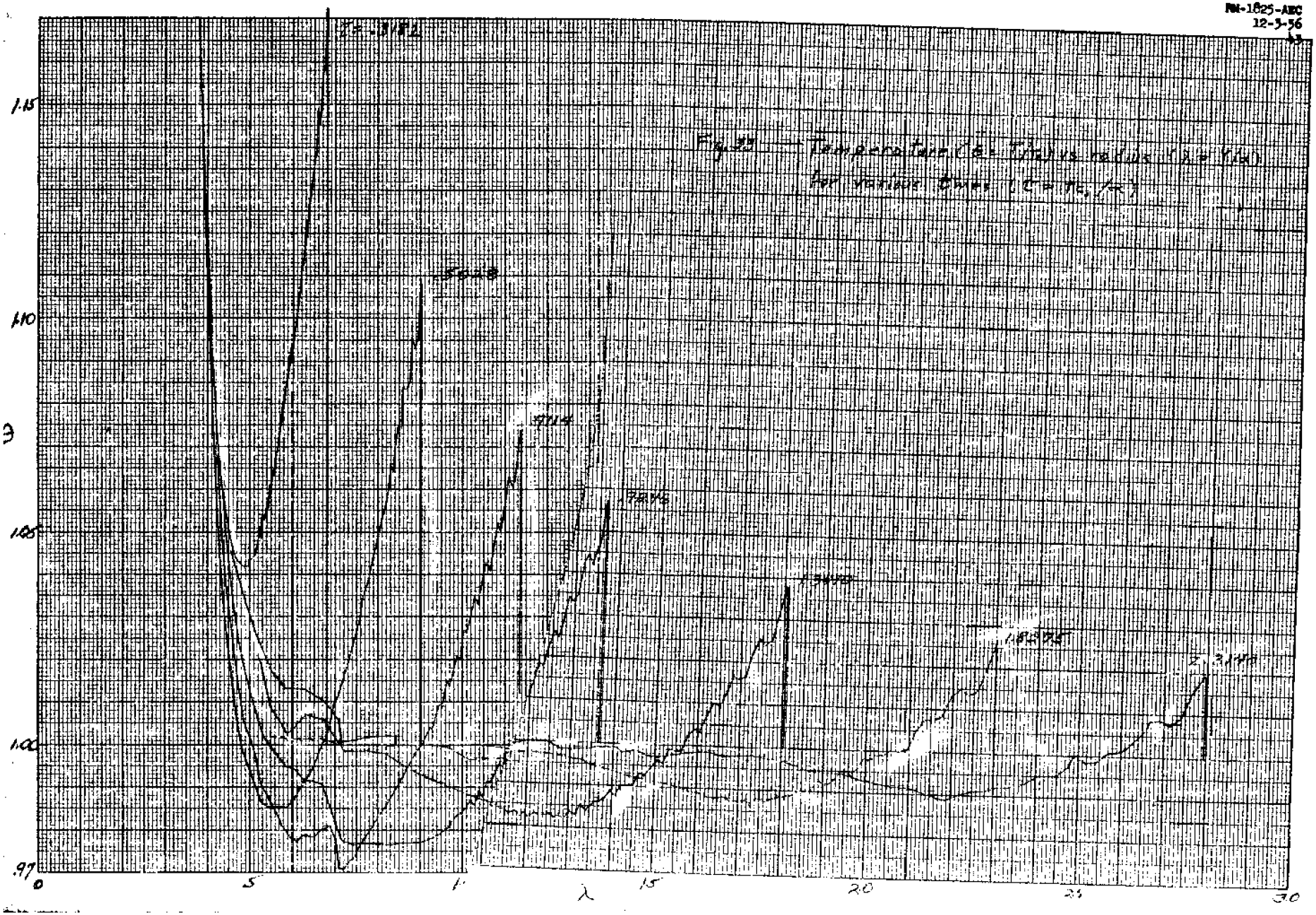

Fig. 29 — Temperature ratio ($\theta = T/T_0$) vs. radius ($\lambda = r/r_0$) for various times ($\zeta = \pi_0 t/R^2$)

RM-1825-ABC
12-3-56

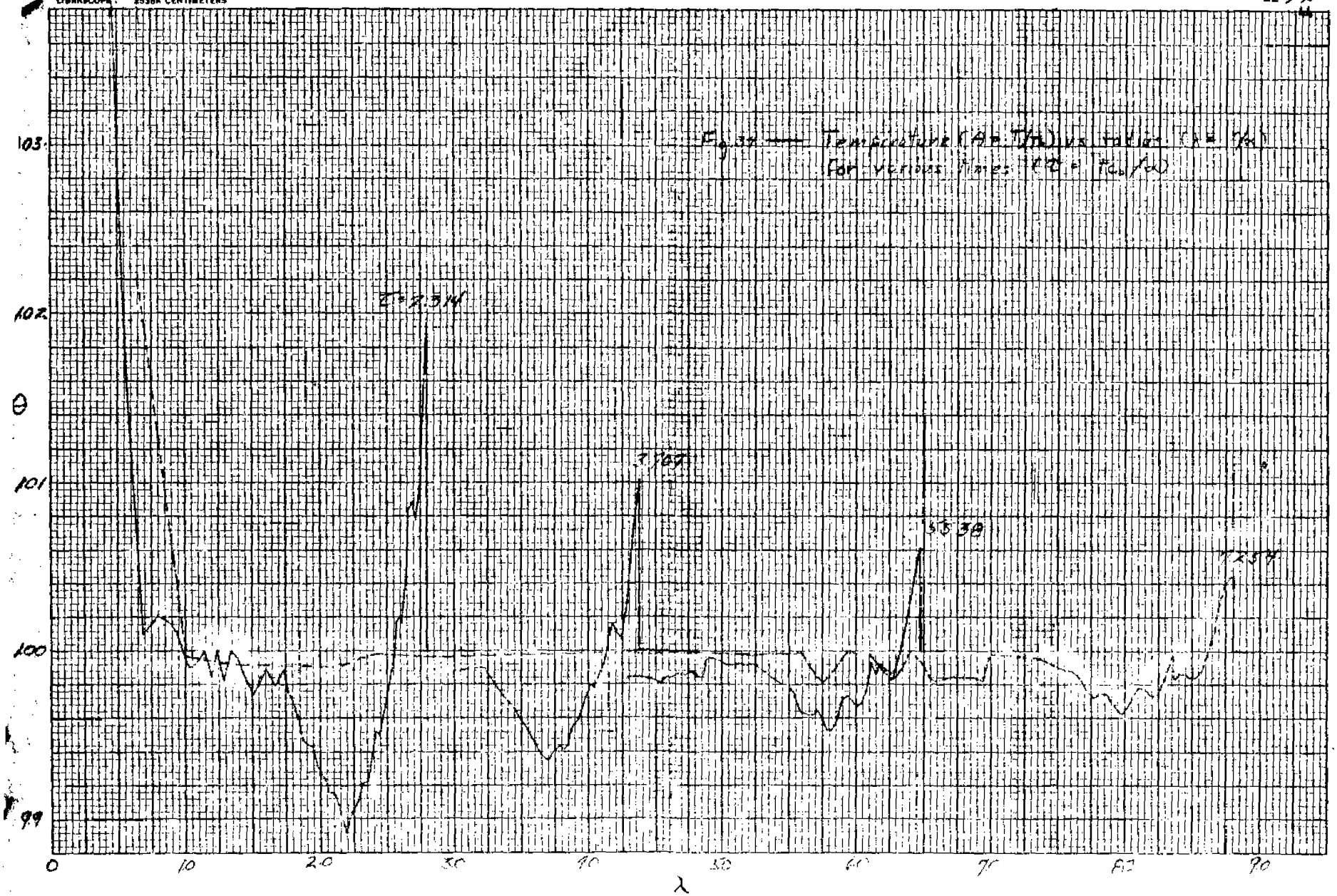

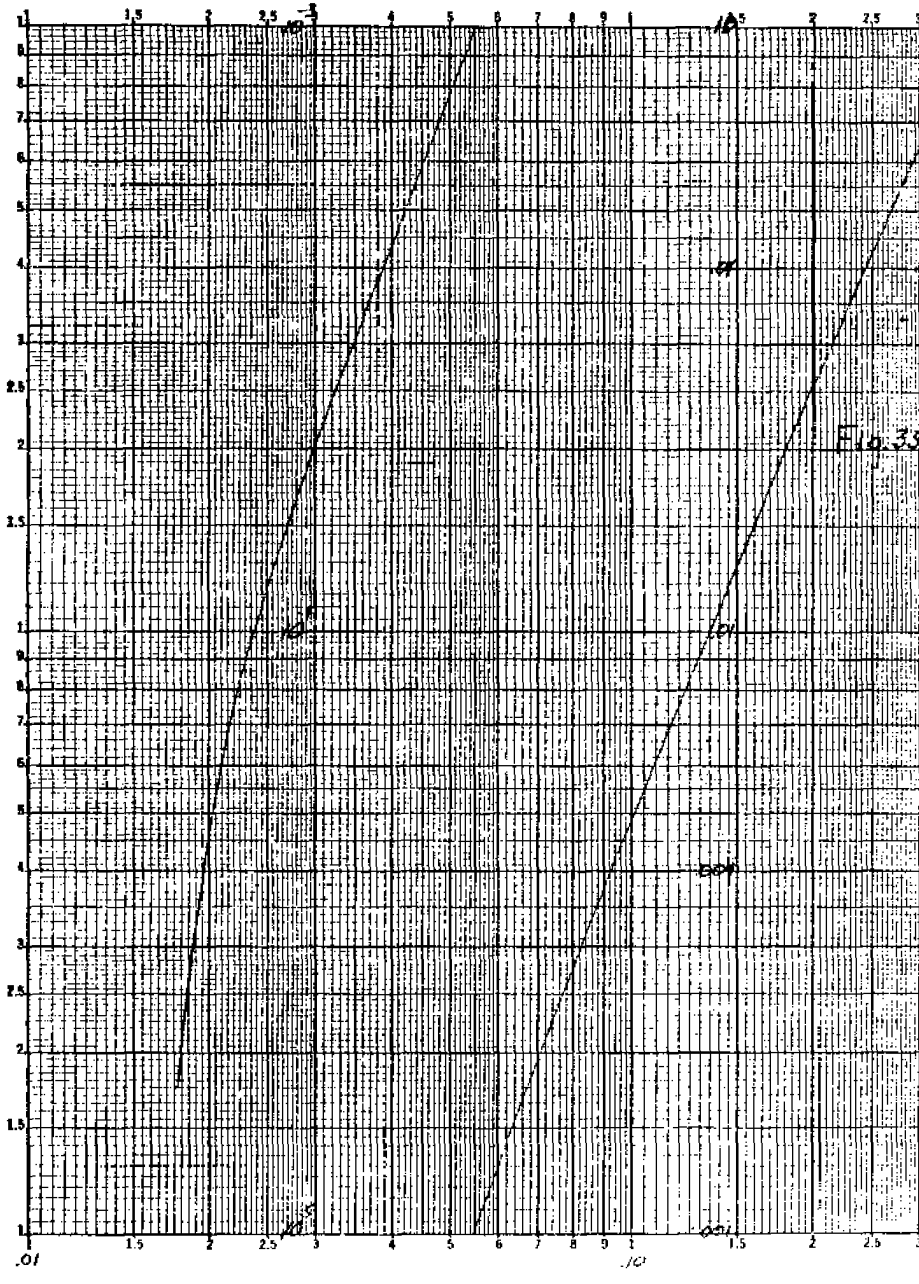
Fig. 33

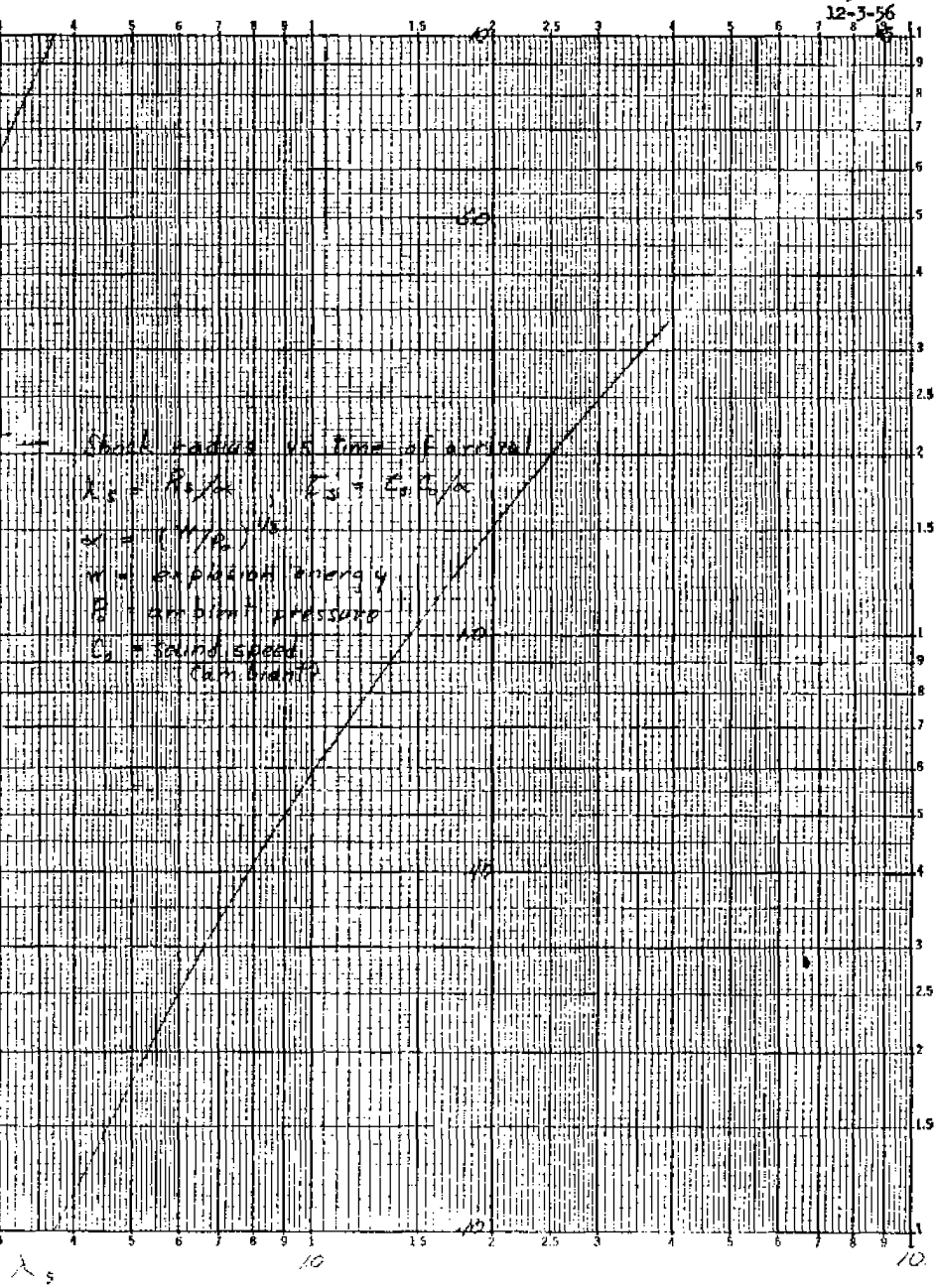
Shock radius vs time of arrival
$\lambda_s = R_s/a$
$\tau_s = t_s c_0/\alpha$
$\alpha = (w/p_0)^{1/3}$
w = explosive energy
p_0 = ambient pressure
c_0 = sound speed
λ_s

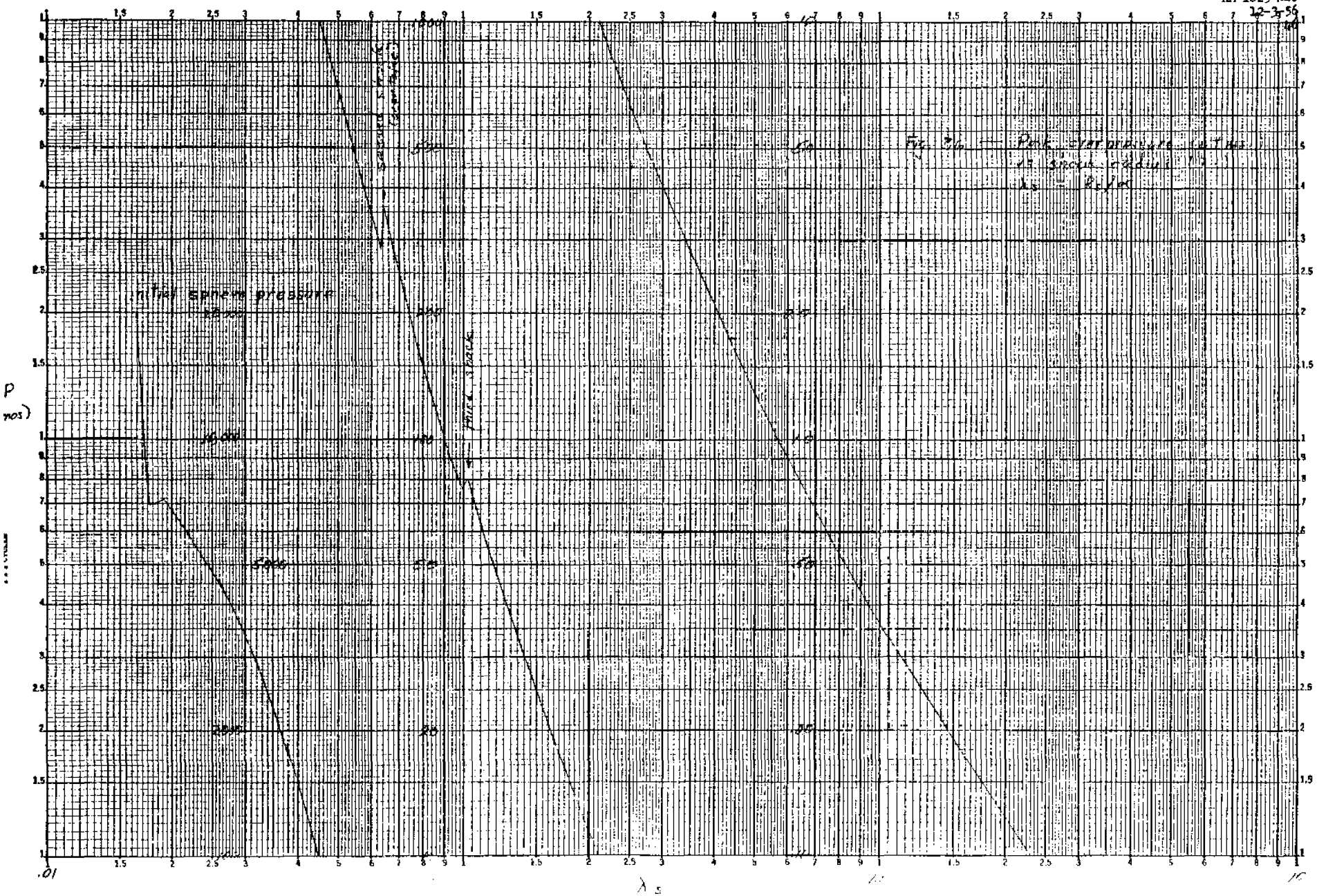
initial sphere pressure
p
nos)
λ_s

RM-1825-ABC
12-3-56

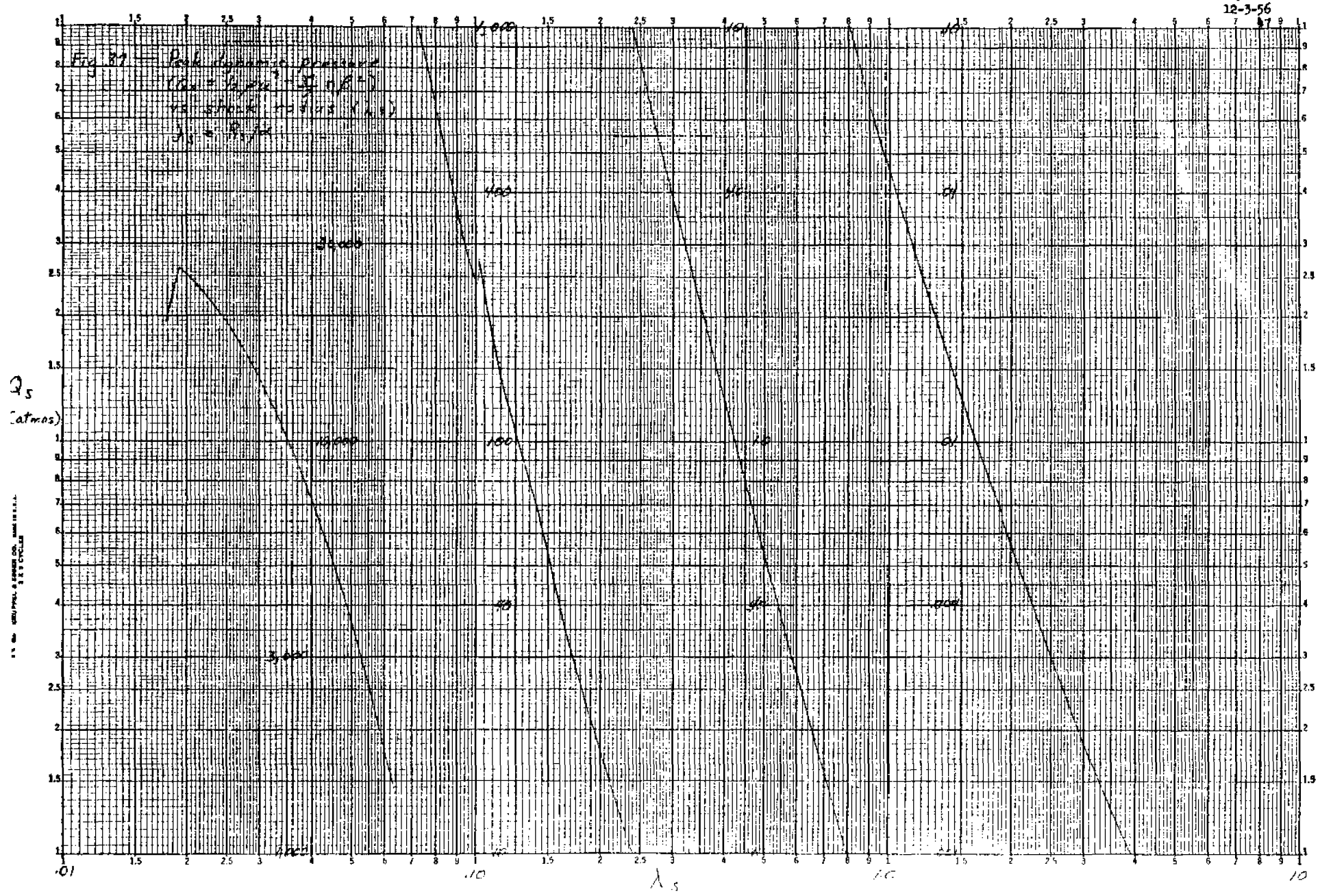

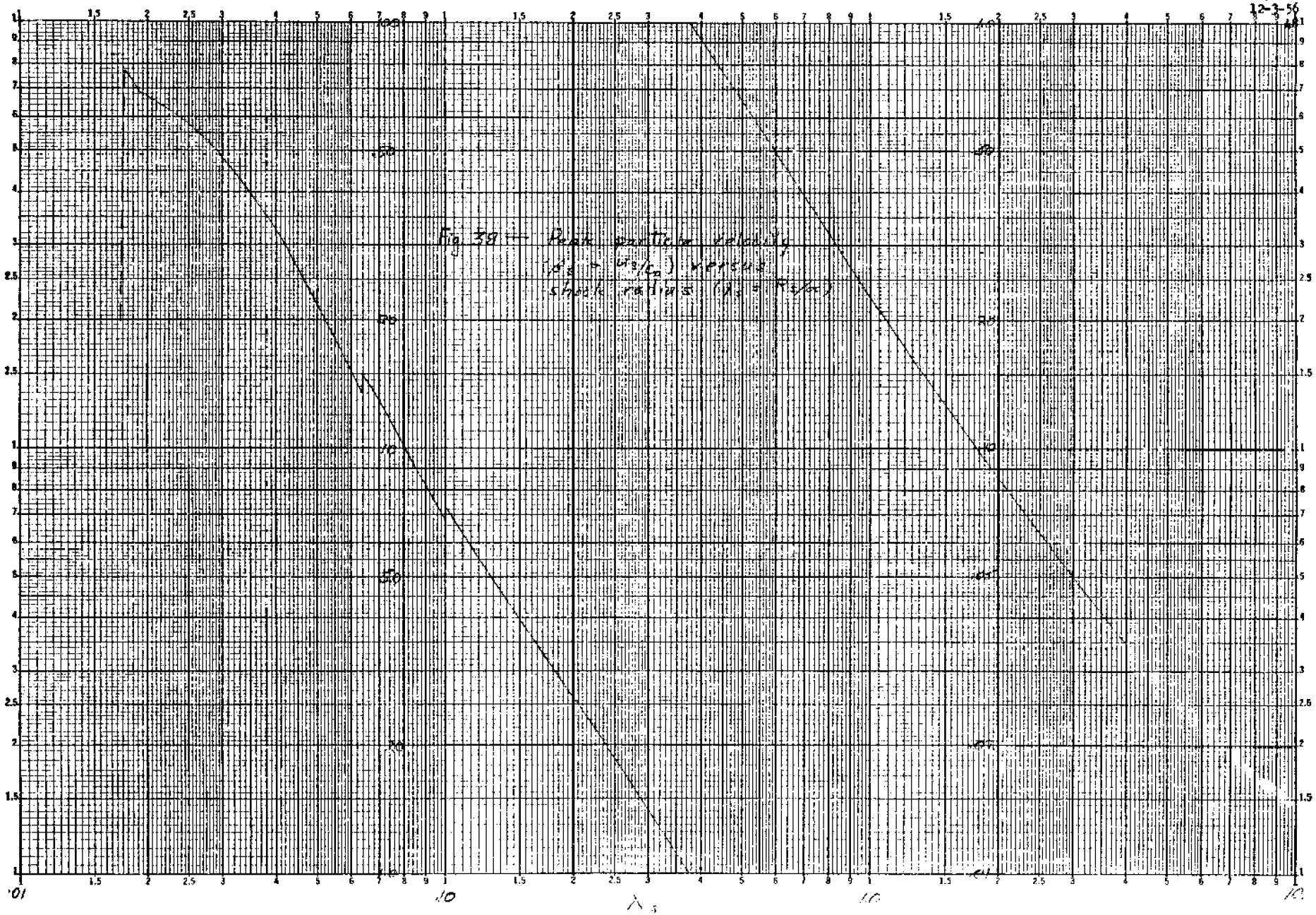

Fig. 39 — Peak particle velocity ($\sigma'_s = \sigma_s/c_0$) versus shock radius ($\lambda_s = R_s/\alpha$)

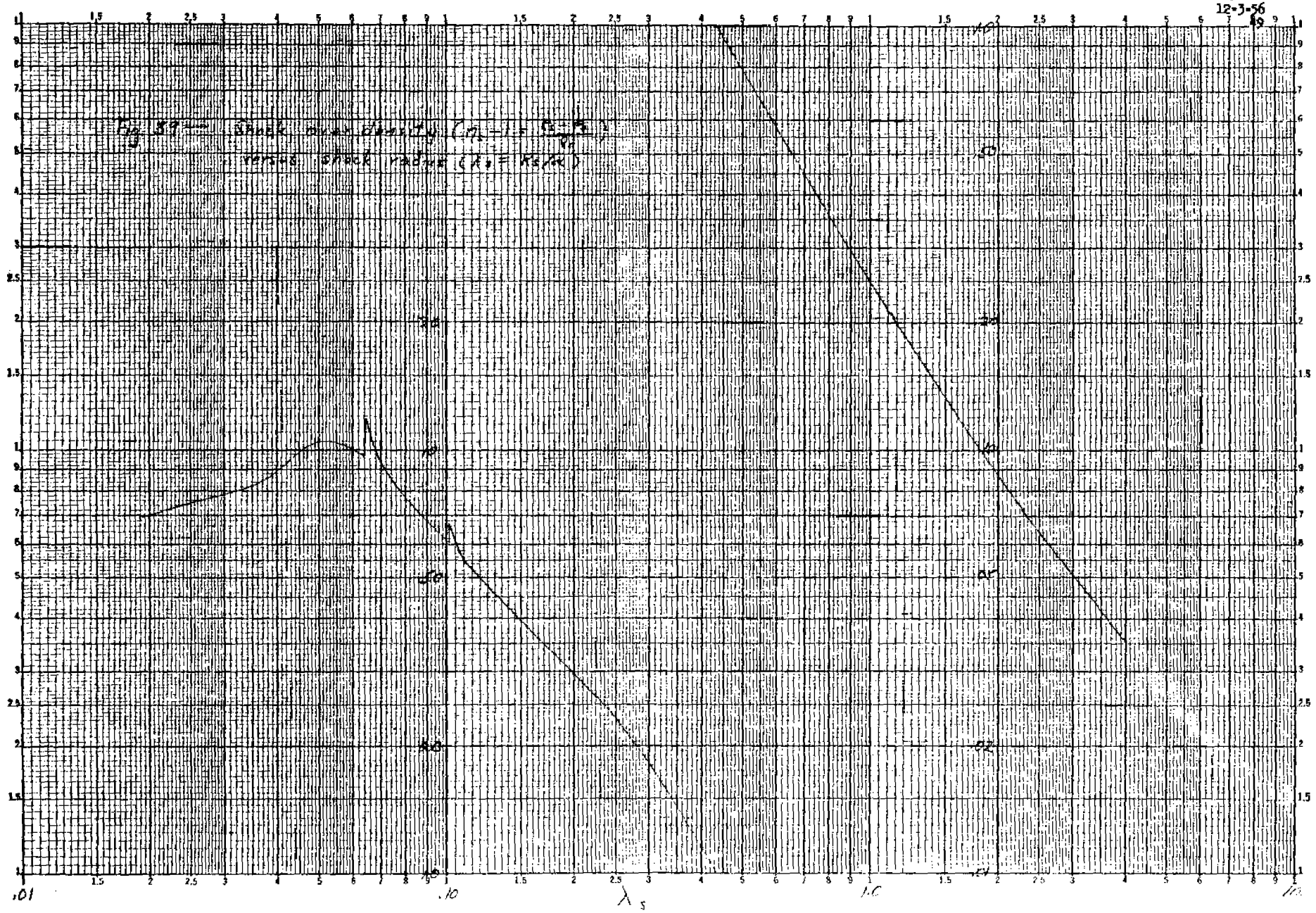
Fig. 37 — Shock mean density ($\sigma_1 = \frac{\rho_s - \rho_\infty}{\rho_\infty}$) versus shock radius ($R_s = R_s/R$)
λ_s
.01
.10

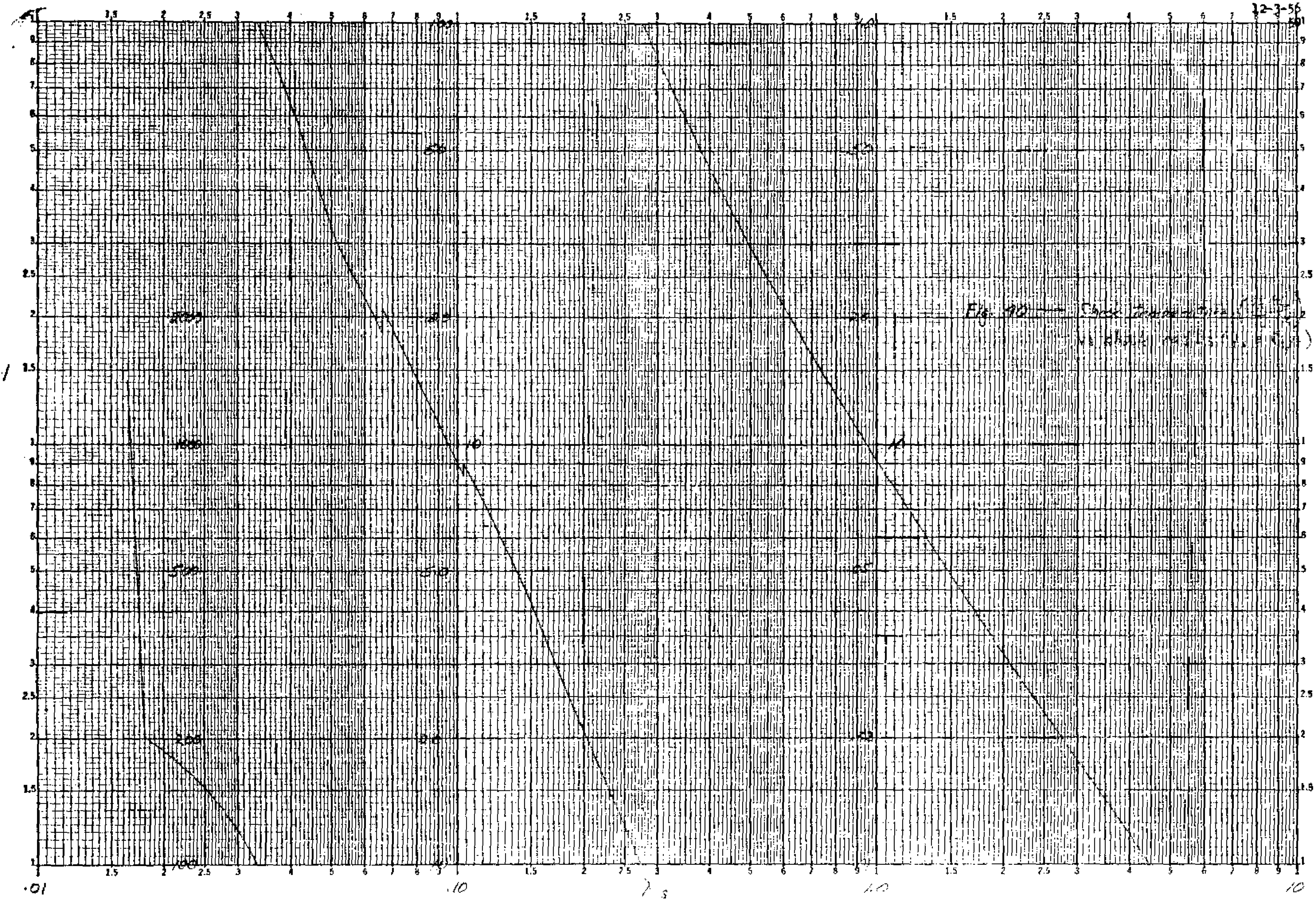

Fig. 40 —

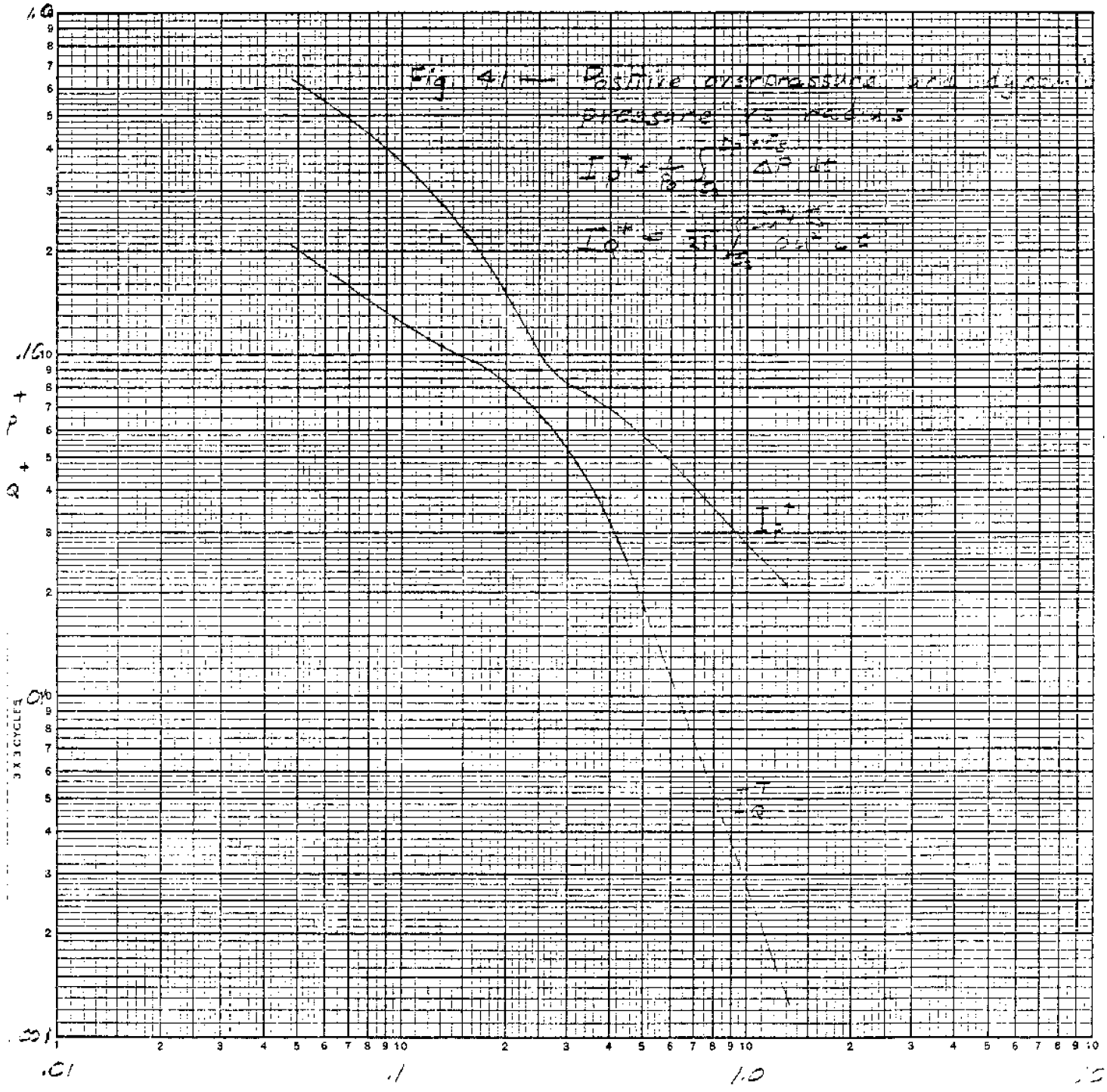
3 X 3 CYCLES
.01
.1
1.0
λ

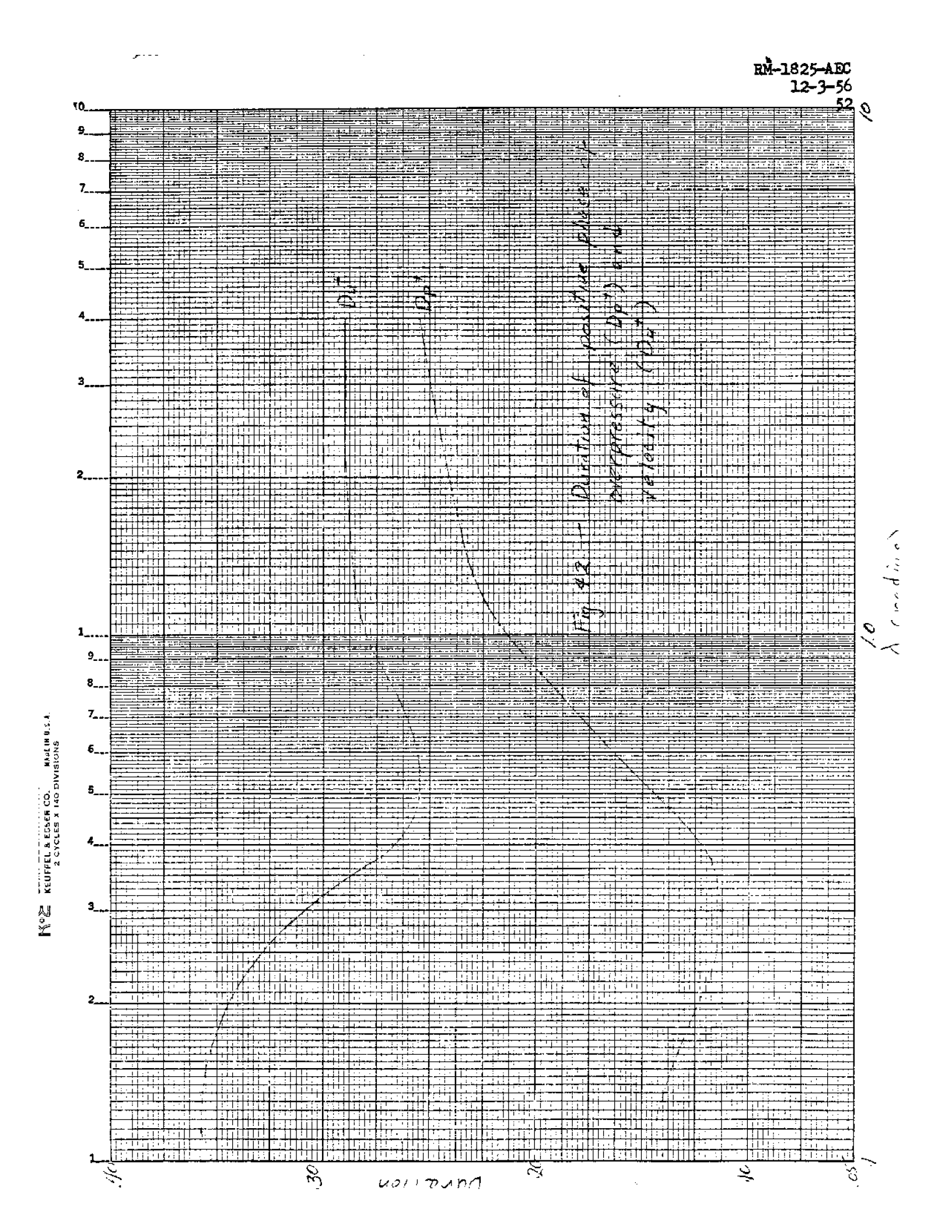

KEUFFEL & ESSER CO. MADE IN U.S.A.
2 CYCLES X 140 DIVISIONS

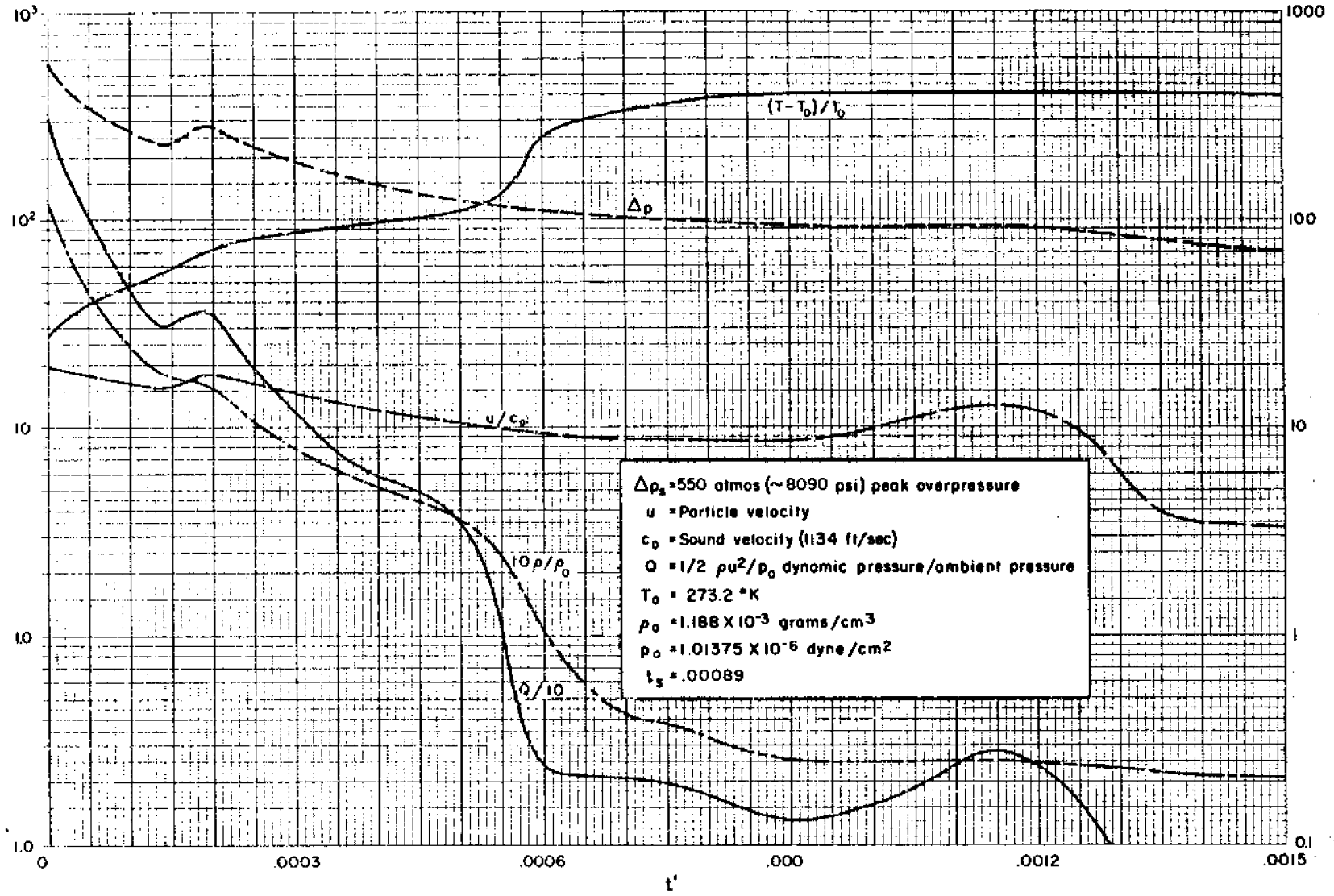

Fig. 43— Blast wave parameters as a function of time after shock arrival at $\lambda = .053$

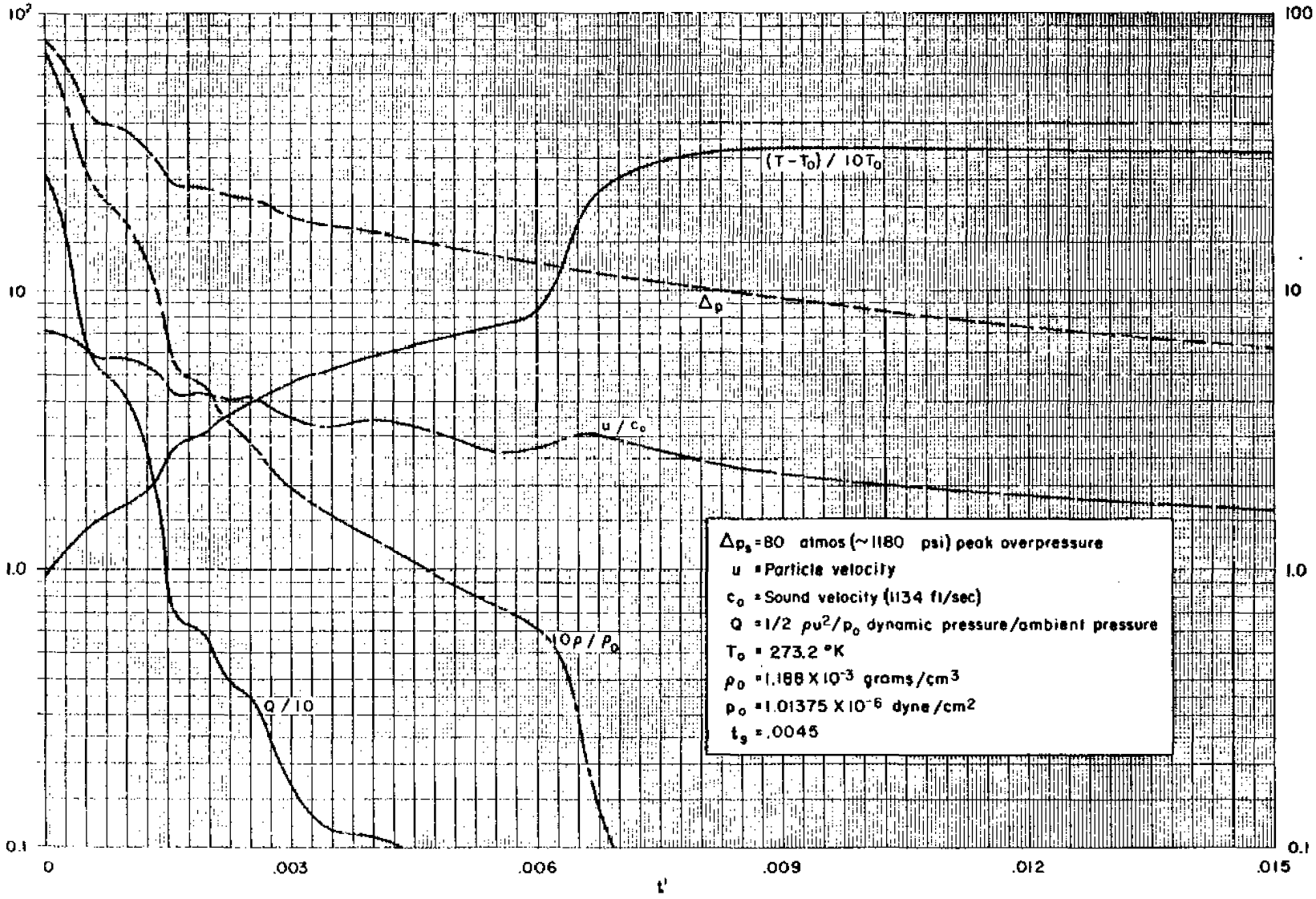

Fig. 44 — Blast wave parameters as a function of time after shock $\lambda = .098$

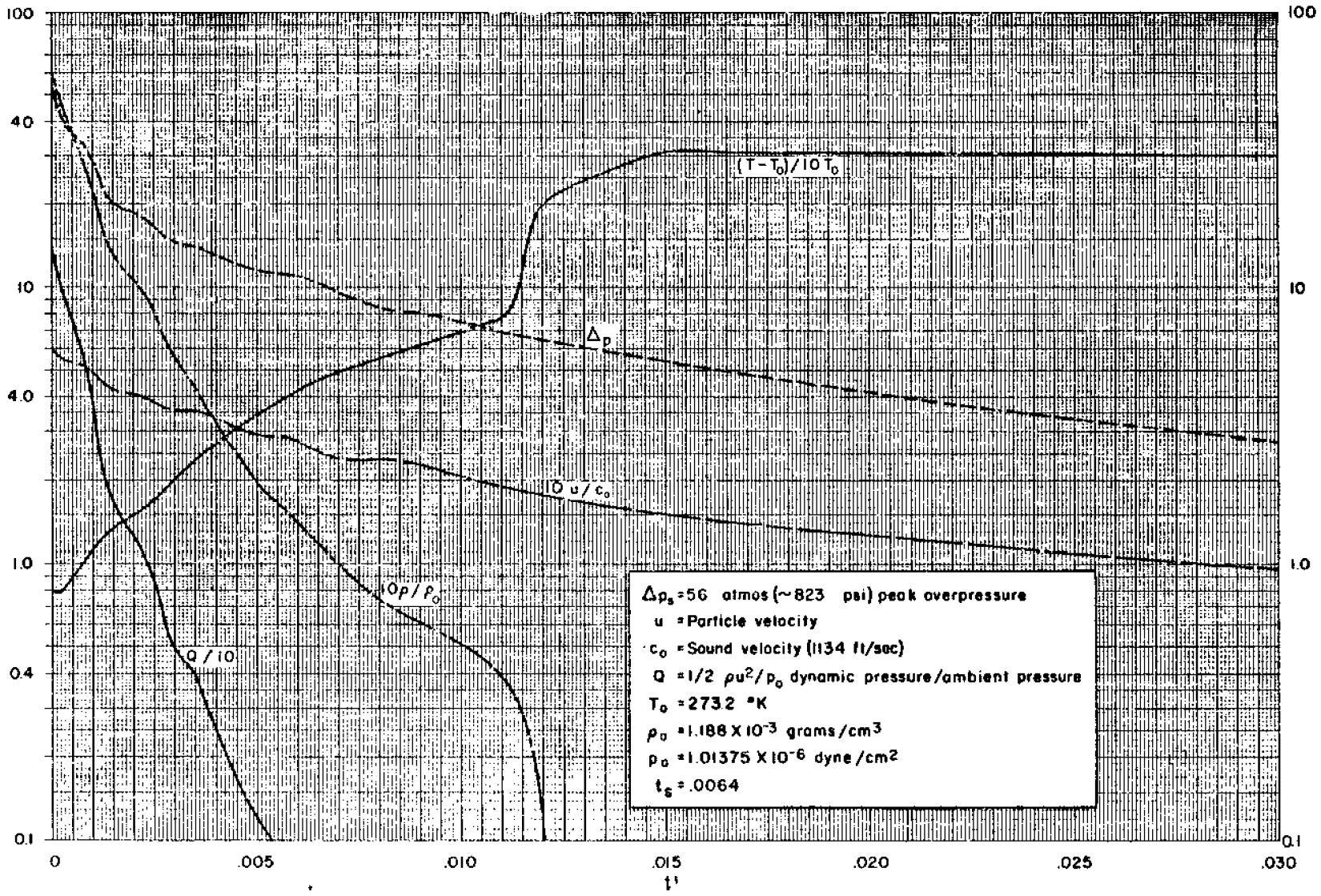

Fig. 45— Blast wave parameters as a function of time after shock arrival at $\lambda = .114$

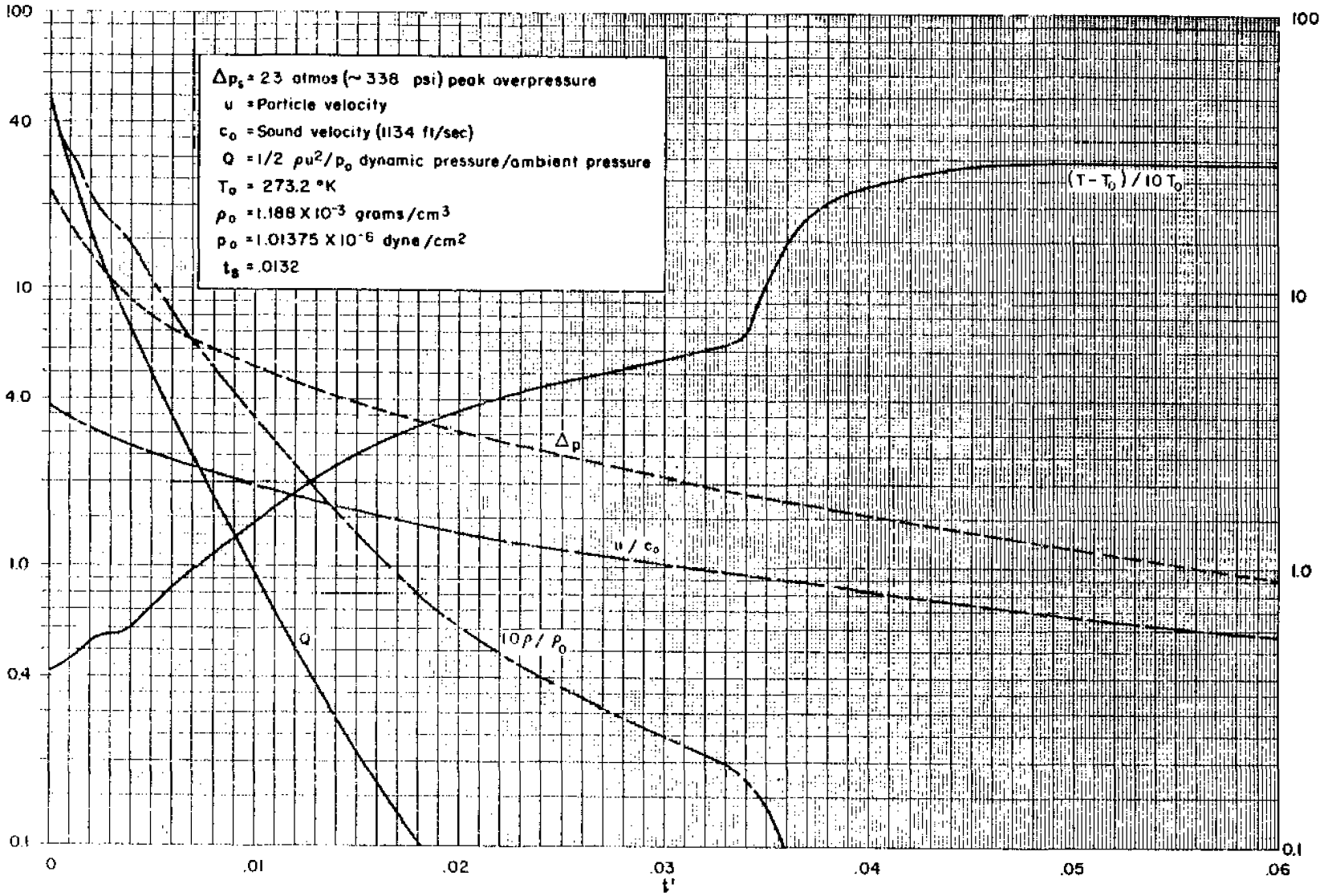

Fig. 46 — Blast wave parameters as a function of time after shock arrival at $\lambda = .155$

RM-1825-AEC
12-3-56
56

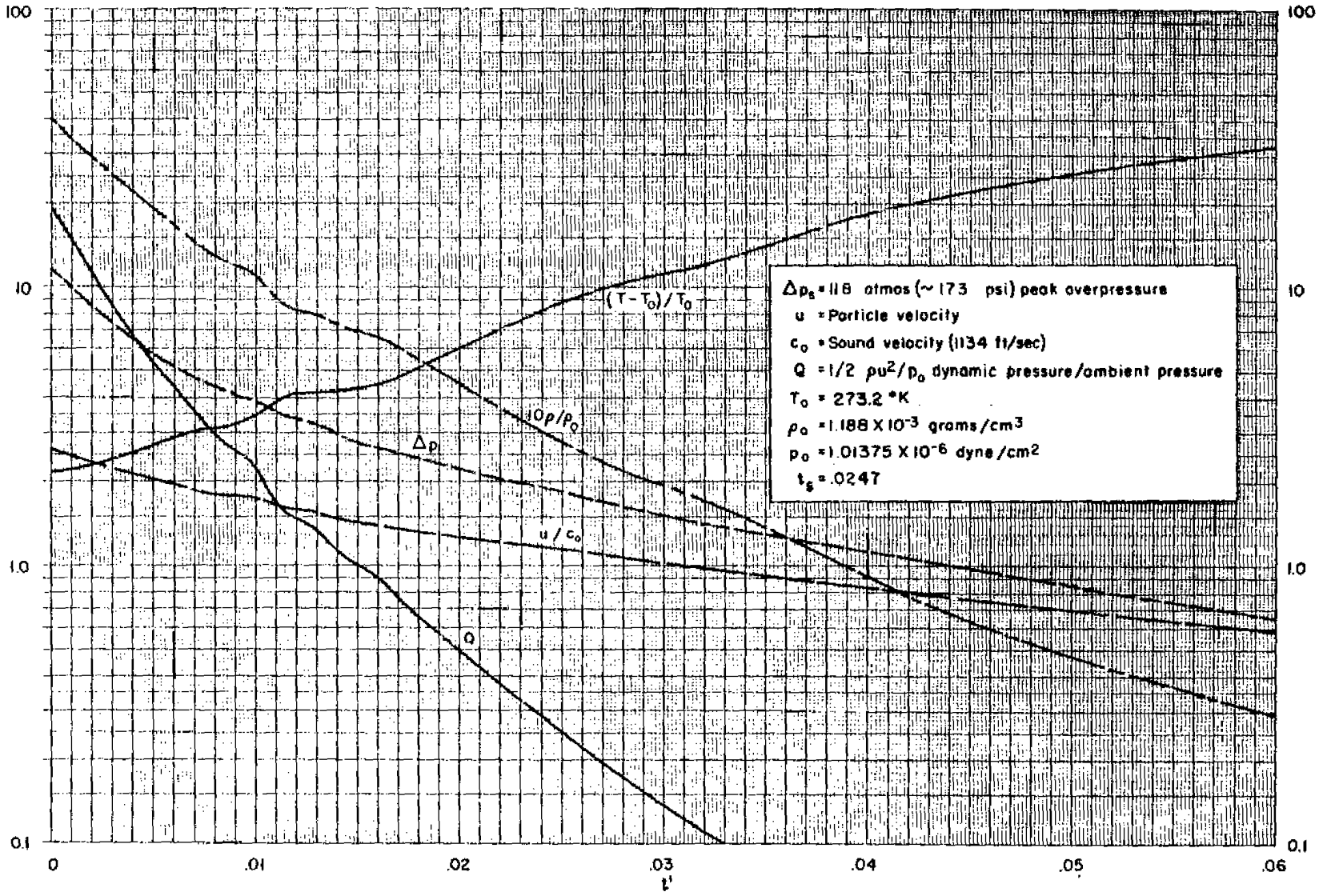

Fig. 47 – Blast wave parameters as a function of time after shock arrival at $\lambda = .200$

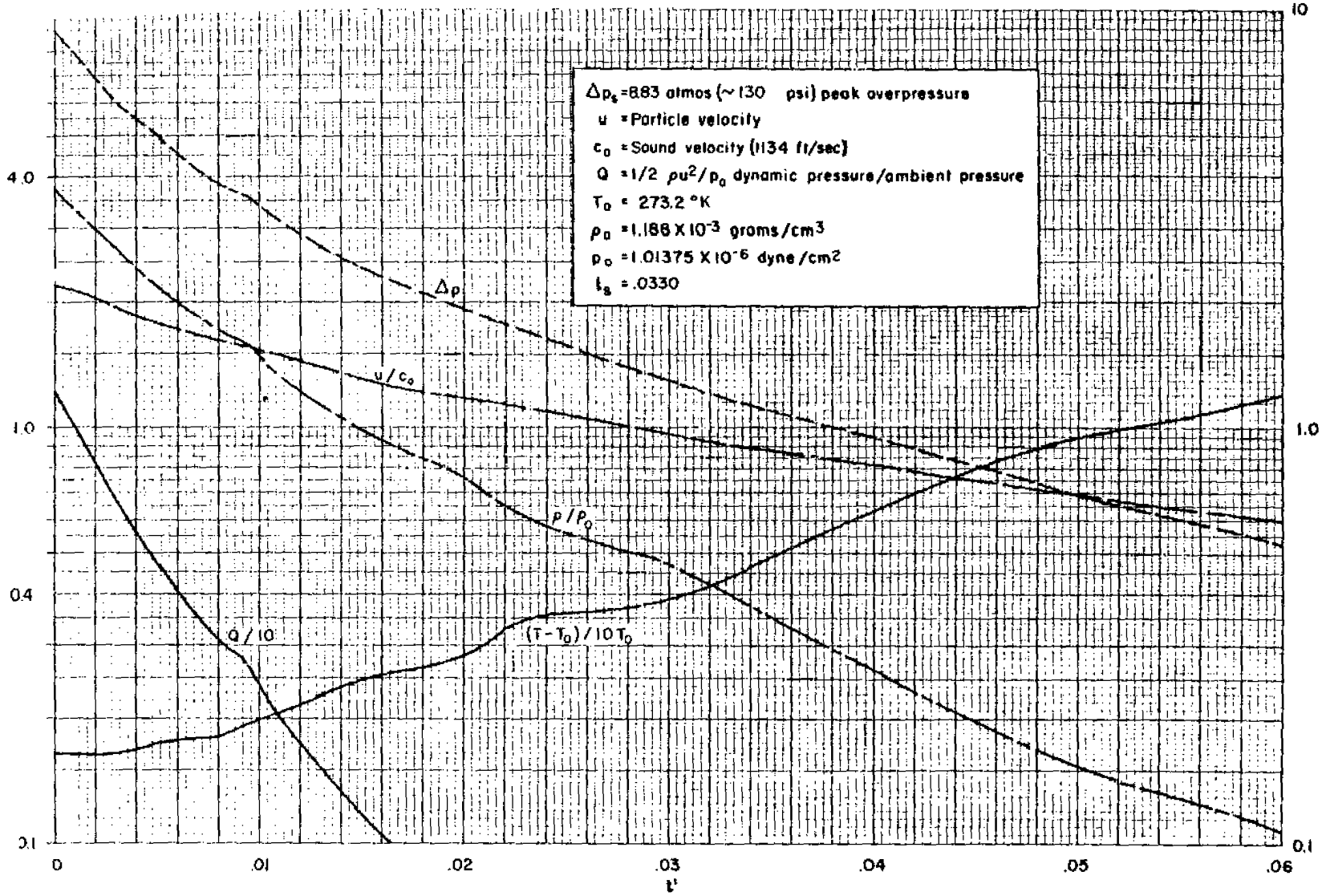

Fig. 48 — Blast wave parameters as a function of time after shock arrival at $\lambda = .220$

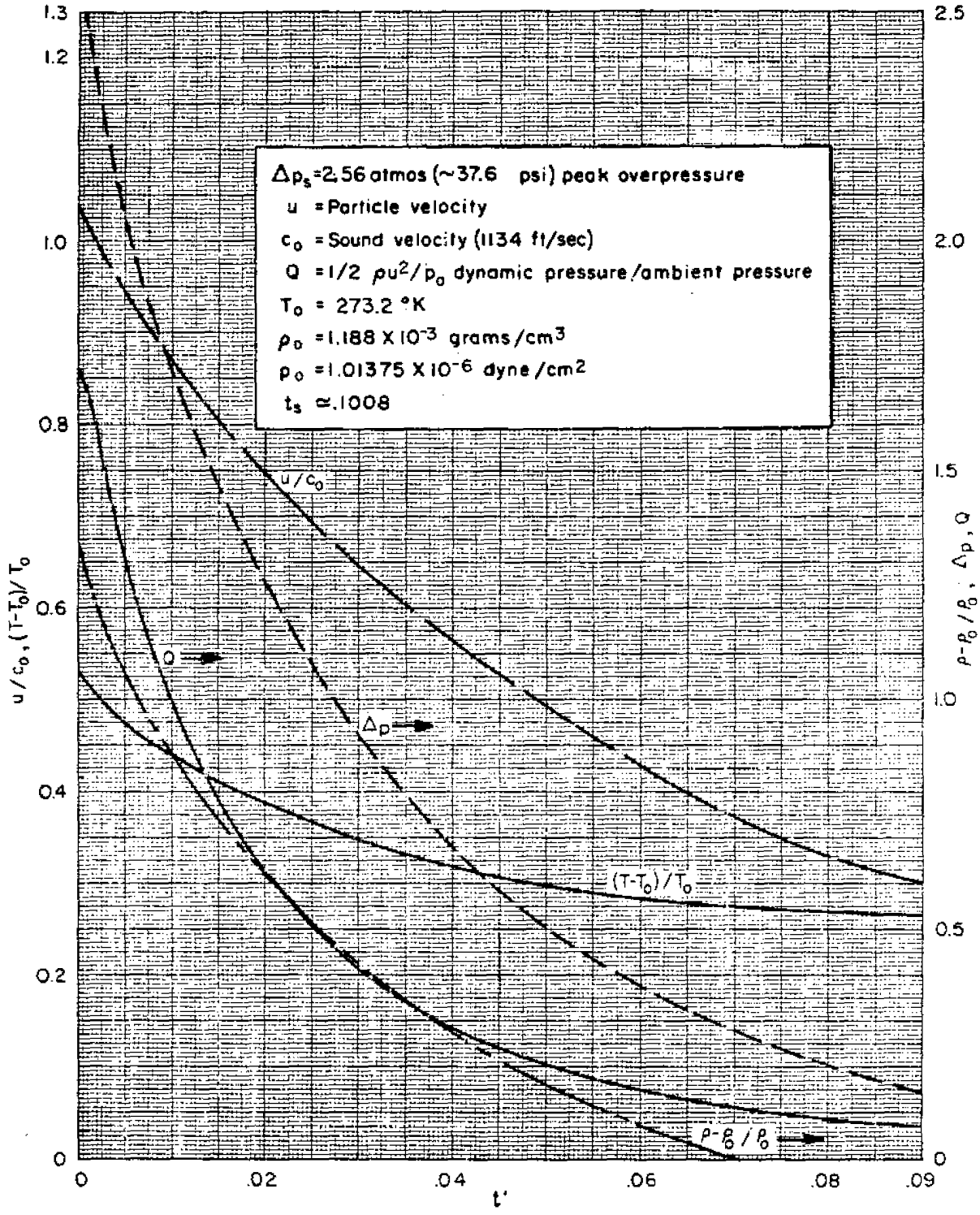

Fig. 49—Blast wave parameters as a function of time after shock arrival at λ = .366

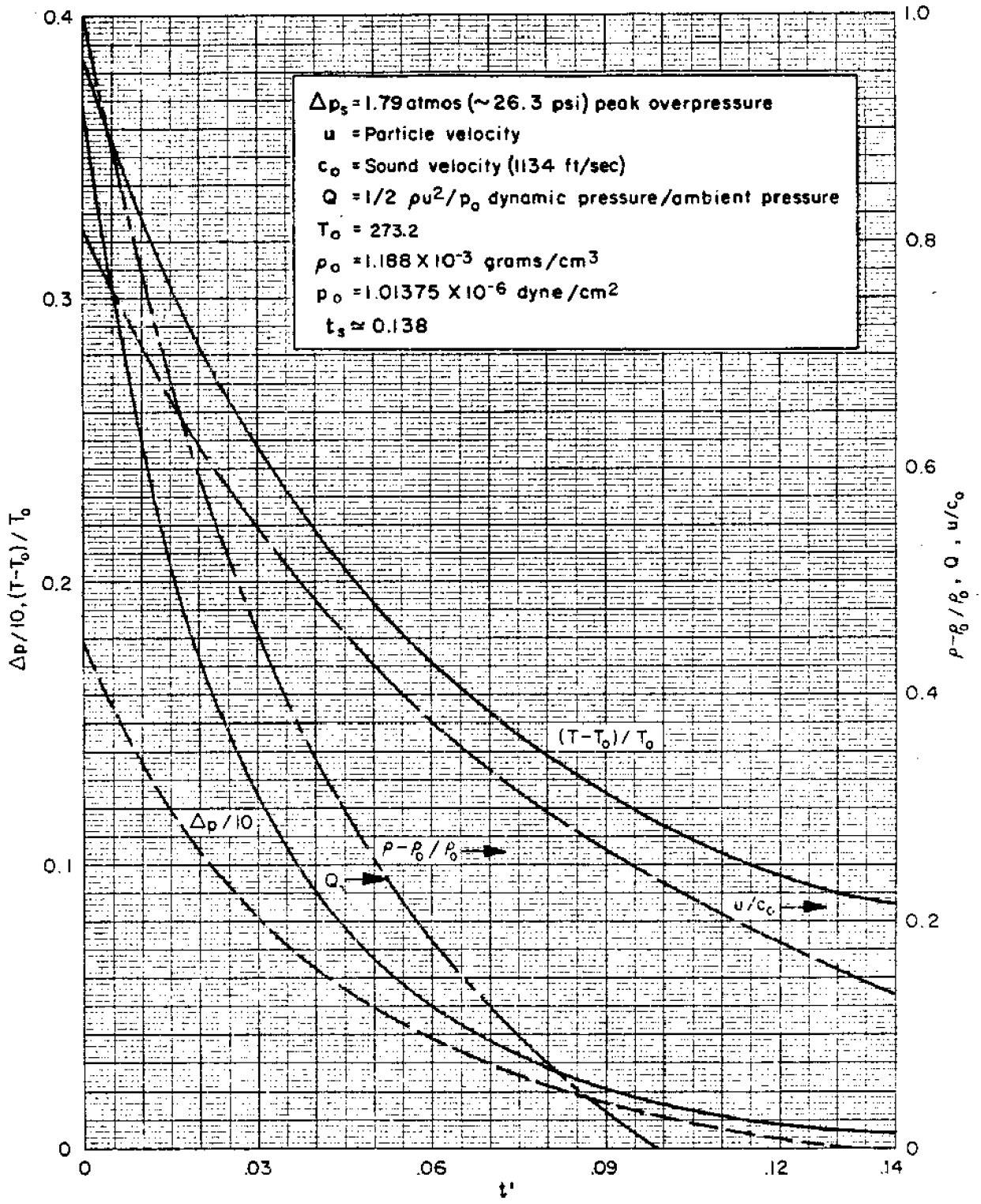

Fig. 50—Blast wave parameters as a function of time after shock arrival at $\lambda = .430$

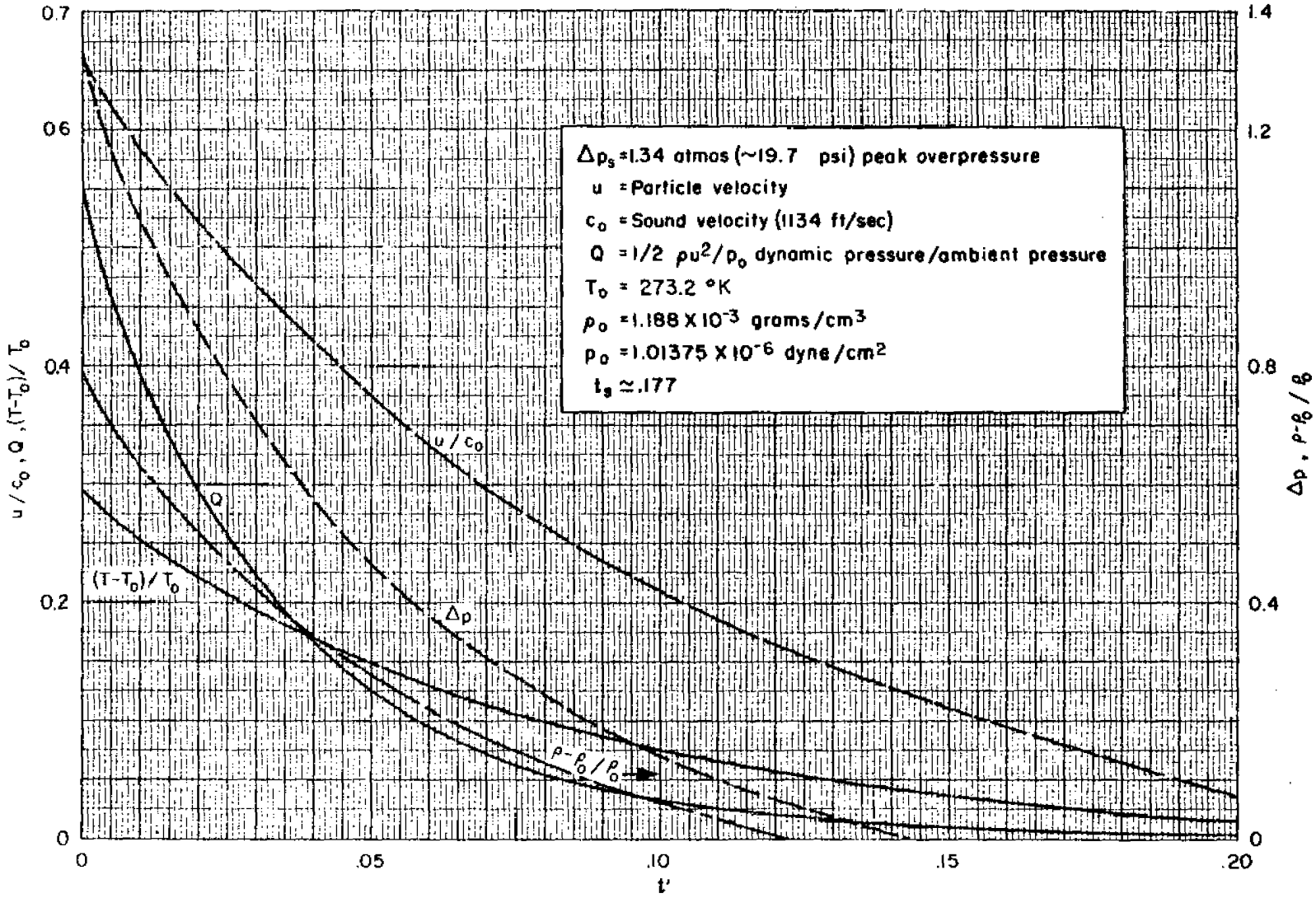

Fig. 51 – Blast wave parameters as a function of time after shock arrival at $\lambda = .493$

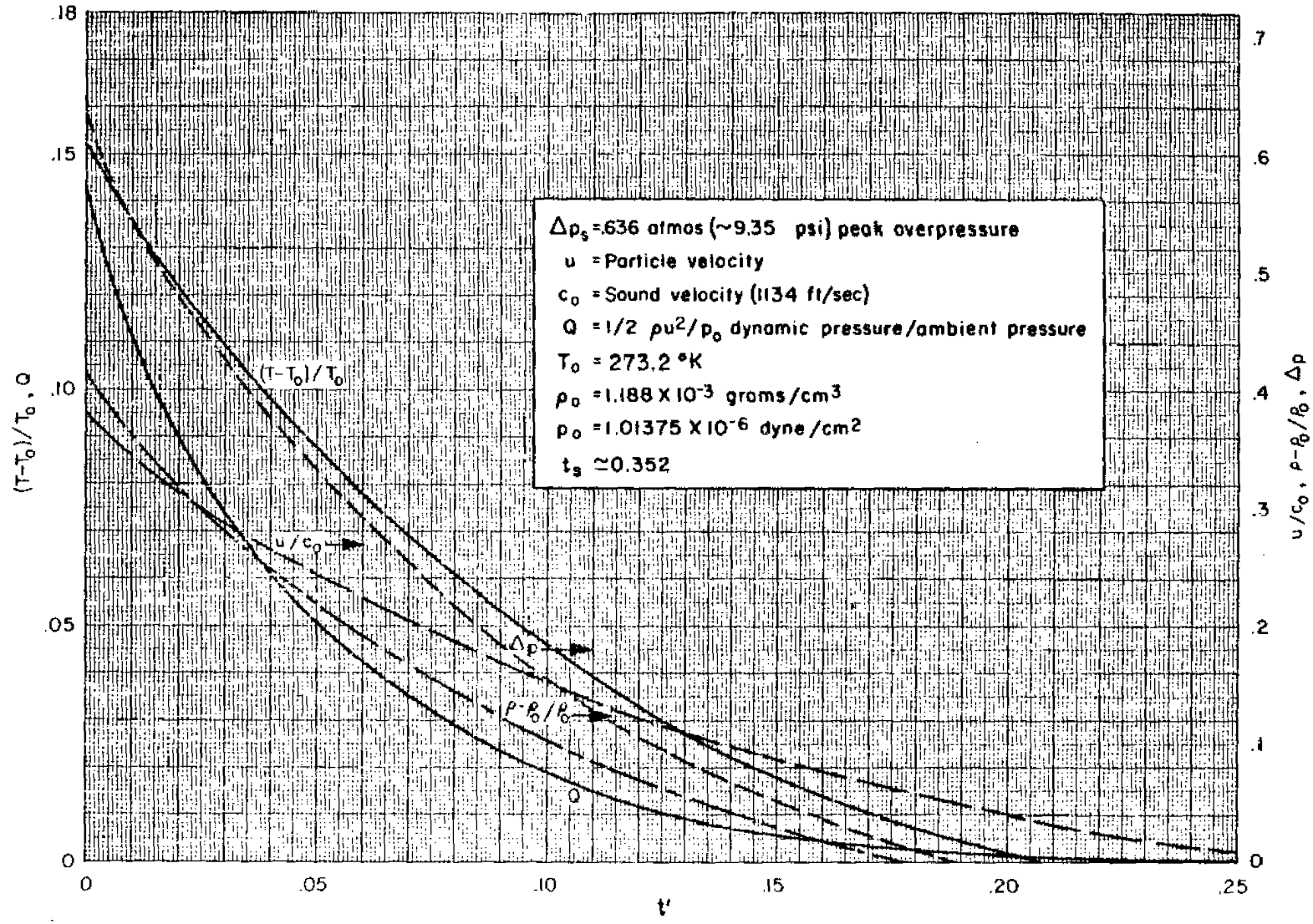

Fig. 52– Blast wave parameters as a function of time after shock arrival at λ= .728

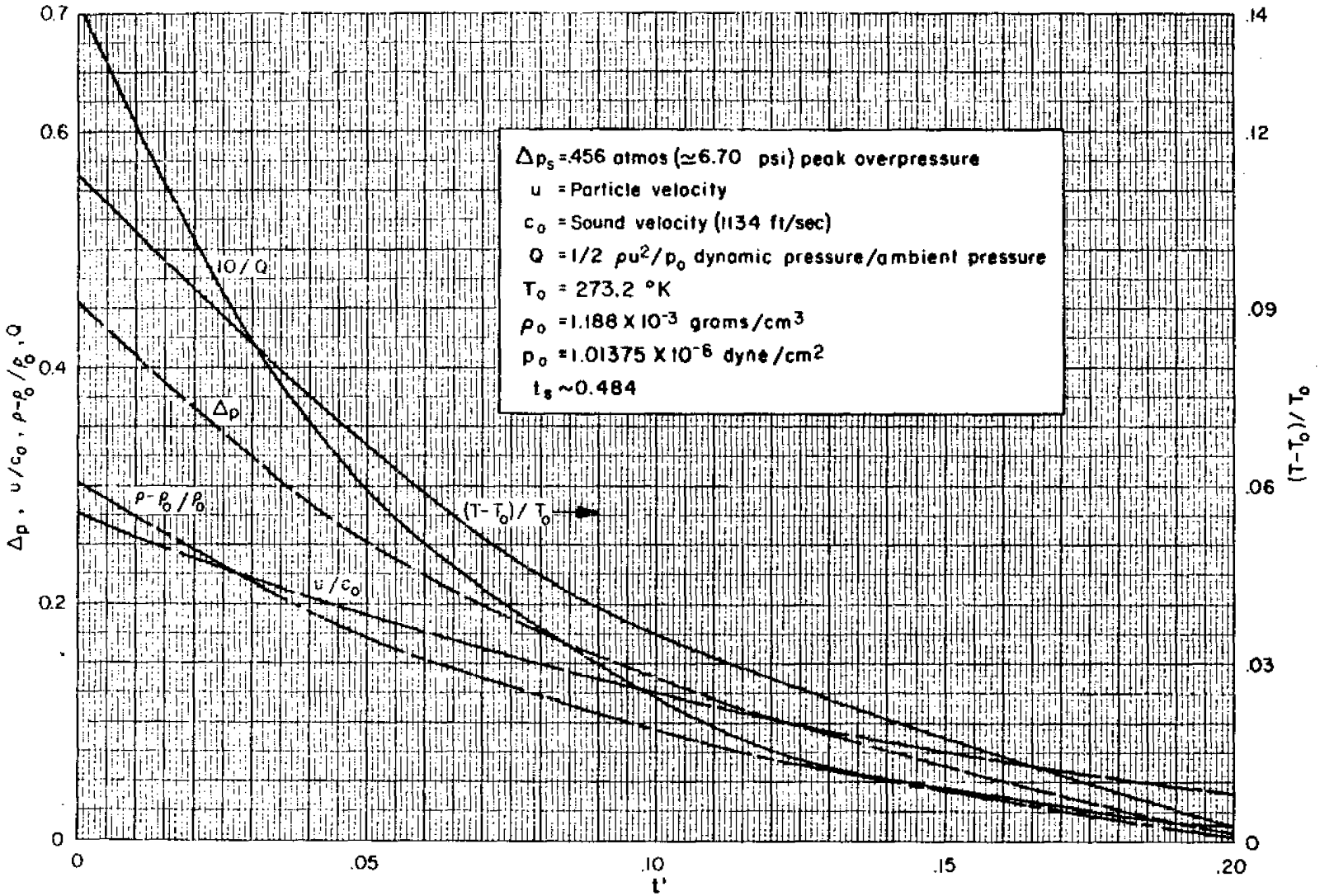

Fig. 53– Blast wave parameters as a function of time after shock arrival at λ= 0.88

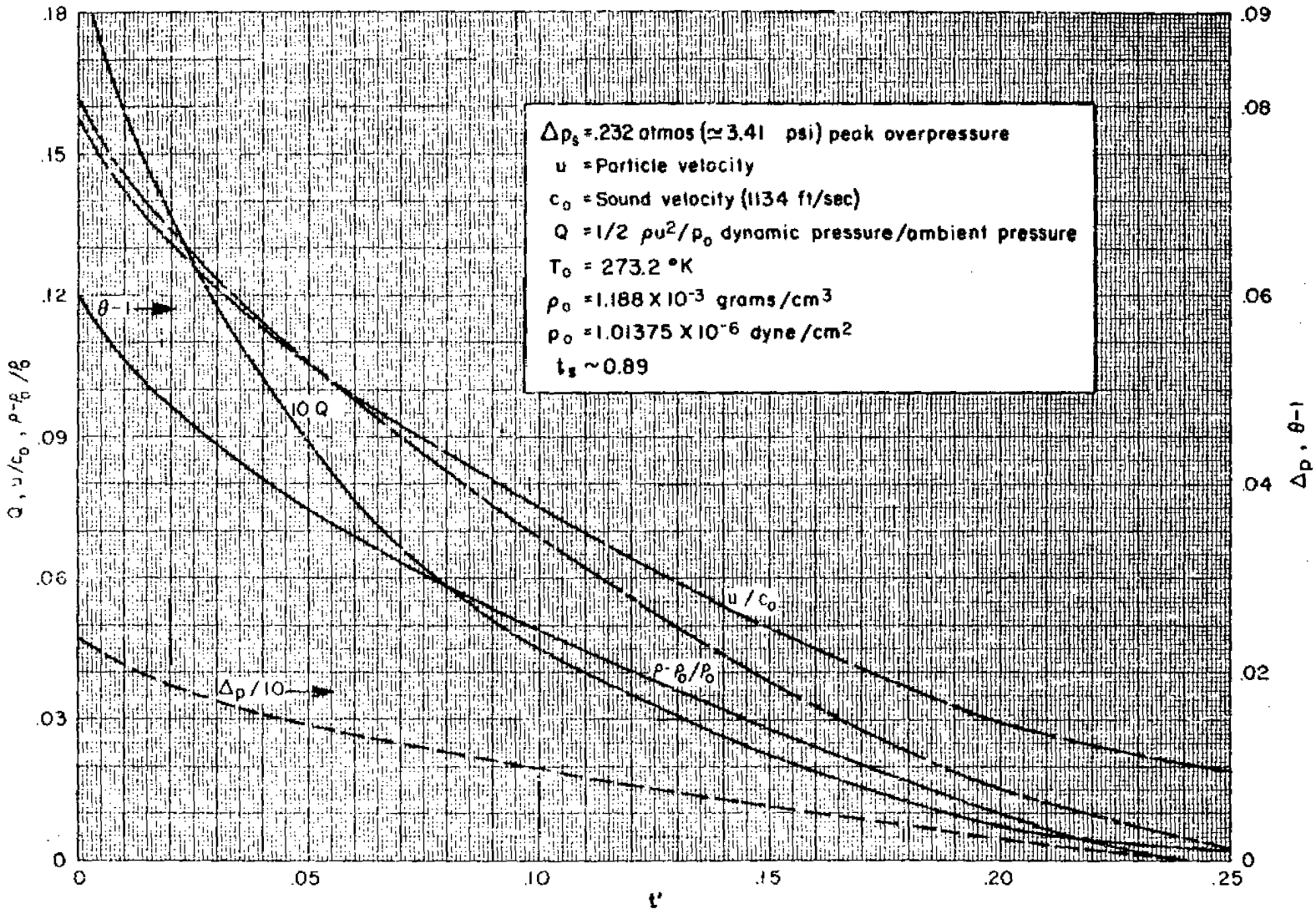

Fig. 54- Blast wave parameters as a function of time after shock arrival at λ=1.34

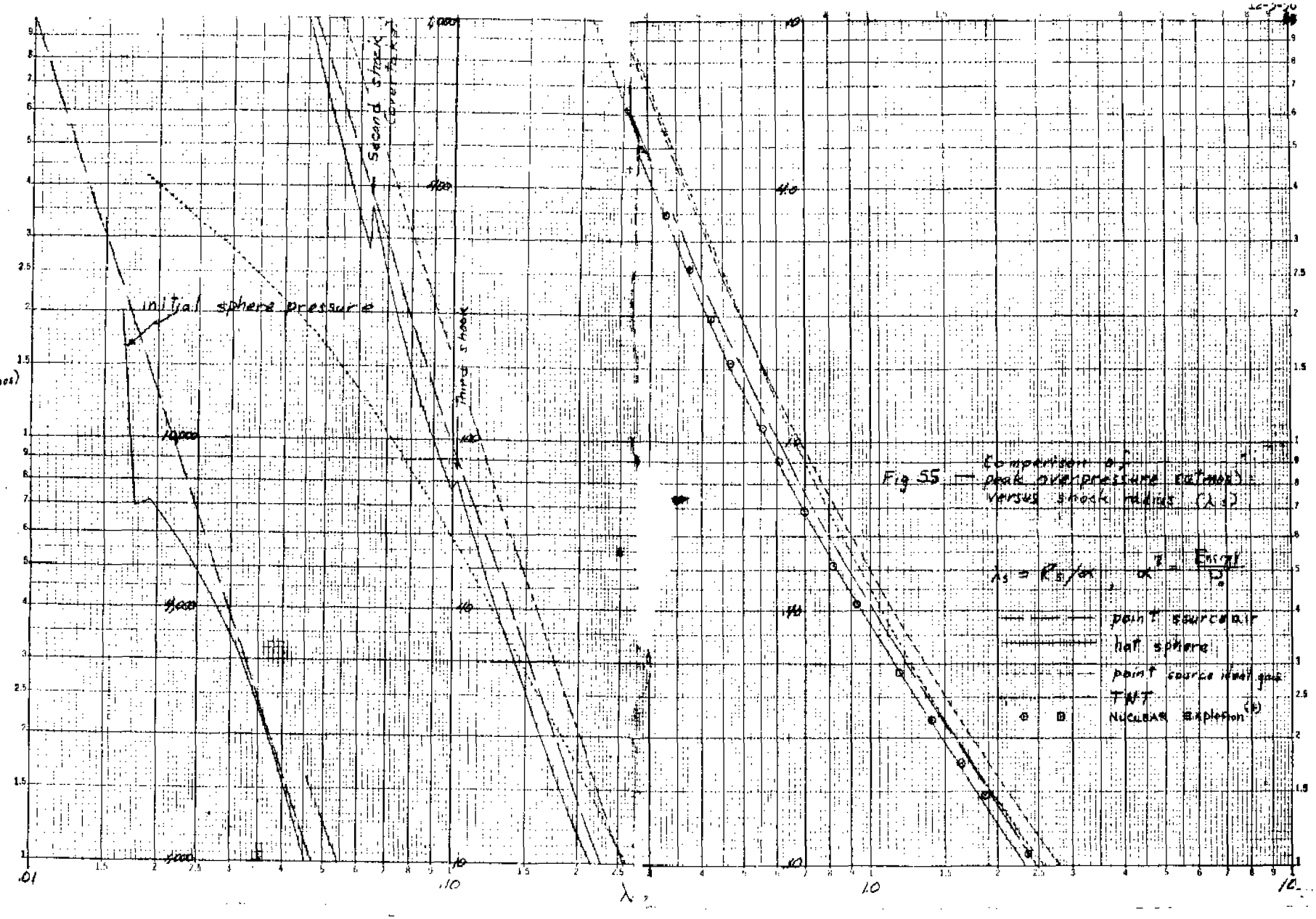

Fig 55 — Comparison of peak overpressure (atmos) versus shock radius (λ_s)

REFERENCES

1. Brode, H. L., Point Source Explosion in Air, The RAND Corporation, Research Memorandum RM-1824-AEC, December 3, 1956.

2. Brode, H. L., Space Plots of Pressure, Density, and Particle Velocity for the Blast Wave From a Point Source in Air, The RAND Corporation, Research Memorandum RM-1913-AEC, June 3, 1957.

3. Brode, H. L., A Calculation of the Blast Wave From a Spherical Charge of TNT, The RAND Corporation, Research Memorandum RM-1965, October 21, 1957. Also published in Phys. Fluids, Vol. 2, 1959, p. 217.

4. Taylor, G. I., Proc. Roy. Soc., Vol. 201A, 1950, pp. 159-186.

5. Shock Hydrodynamics and Blast Waves, Los Alamos Scientific Laboratory, Report AECD-2860, 1944.

6. Glasstone, Samuel (ed.), The Effects of Nuclear Weapons, U. S. Department of Defense, U. S. Atomic Energy Commission, June 1957.

7. Brode, H. L., Numerical Solutions of Spherical Blast Waves, The RAND Corporation, Research Memorandum RM-1363-AEC, September 29, 1954. Also published in J. Appl. Phys., Vol. 26, 1955, p. 766.